ANALYTICAL AND NUMERICAL STUDY OF INSTABILITY OF SUPERCRITICAL WATER FLOWING UPWARD IN TWO HEATED PARALLEL CHANNELS WITH WALL THERMAL ENERGY STORAGE EFFECTS.

BY

DHANASHREE SURYAJI GHADGE

A Thesis
Submitted to the Faculty of Graduate Studies
In Partial Fulfillment of the Requirements for the Degree of

MASTER OF SCIENCE

Department of Mechanical and Manufacturing Engineering
University of Manitoba
Winnipeg, Manitoba

Abstract

The wall thermal energy storage effects on supercritical thermal hydraulic instability were investigated using a 1D-Linear frequency domain solution and 3D- Non-linear ANSYS CFX solution. Experimental cases of supercritical upward flow in two heated parallel channels were analysed.

The one-dimensional (1D) analyses were done with two different wall thicknesses using uniform and non-uniform power distributions. It was found that the inclusion of wall thermal energy storage effects gives better prediction of thermal hydraulic instability in these two heated parallel-channel cases, which contradicts the conclusions of previous studies with wall thermal energy storage effects. Accurate prediction of the period of oscillation was also obtained. The 3D- numerical solution with wall also gives an excellent agreement with the experiments, for the instability boundary. A common CFD assumption; namely, circumferentially symmetric flow, was found to be inadequate. Temporal and grid independence was ensured for the reported cases. The predictions of period of oscillation obtained with the non-linear 3D ANSYS CFX code are discussed.

Additionally, non-dimensional parameters were derived for the conversion of experimental data from one fluid to another in a given test facility and validated using 1D- linear solution.

Acknowledgement

I would like to express my sincere thanks to my advisor, Dr. V. Chatoorgoon and Dr. S.J. Ormiston for giving me this opportunity to work on this excellent project and their valuable guidance. I would also like to thank AECL/CNL for the financial support of this project. I would also like to express my sincere gratitude to the University of Manitoba for this opportunity. Finally, I am grateful for the support, understanding of my parents, my friends and special ones.

Table of Content

Abstract ii

Acknowledgement iii

Table of Content iv

List of tables viii

List of Figures x

Nomenclature xiii

1. Chapter 1 Introduction 1

1.1 Nuclear energy 1

1.2 Supercritical water-cooled reactor 3

1.3 Supercritical Water Properties 4

1.4 Supercritical Flow Instability 7

1.5 SCWR Modeling 7

2. Chapter 2 Literature Review 9

2.1 Instability Studies of Parallel Channels 10

2.2 Instability studies with wall thermal energy storage effects 23

2.2 Objectives 24

3. Chapter 3 Problem Description 28

3.1 Xiong et al. Experimental Loop (Xiong et al. 2012) 28

3.1.1 Equivalent Geometry (Xiong et al. 2012) 29

3.1.2 Flow Conditions for the Xiong's Experiment (Xiong et al. 2012) 30

3.2 Xi et al. Experimental Loop (Xi et al. 2014) 31

3.2.1 Uniform Power Distribution 32

3.2.2 Influence of Axial Power Shape 33

4. Chapter 4 Analytical Model of wall energy storage (Linear code) 35

4.1 Non-Linear Governing Equations 35

4.1.1 Linearized Governing Equations 36

4.1.2 Laplace Transform of the Linearized Equations 36

4.1.3 Wall Heat Flow 36

4.1.6 Non- heated channel 40

4.2 Boundary Conditions 43

4.2.1 Steady State Solution Boundary Conditions 43

4.2.2 Linear Solution Boundary Conditions 43

4.3 Transfer Function 43

4.4 Numerical Solution Method of the 1D Non-Linear Equations 46

4.5 Solution Domain 46

5 Chapter 5 Non-dimensional parameters 47

5.1 Dimensionless 1D equations for heated channels with supercritical fluids 47

6. Chapter 6 Numerical Modelling 53

6.1 Geometrical Model 53

6.2 Assumptions 57

6.3 Governing Equations 57

6.4 Turbulence Closure 61

6.4.1 Standard k-ε Turbulence Model 62

6.4.2 Scalable Wall Functions 63

6.4.3 Wall Heat Model 65

6.5 Boundary Conditions 66

6.6 Material Properties 68

6.6.1 Supercritical Water 68

6.6.2 INCONEL 625 69

6.7 Grid Generation 69

6.8 Solution Domain 72

6.9 Numerical Solution Method 73

7. Chapter 7 Results and discussions 75

7.1 Linear Code 75

7.1.1 Xiong et al. Cases 75

7.1.2 Xi et al. Cases 76

7.1.3 Single Channel and Identical Parallel Channels 83

7.1.4 Period of Oscillation 84

7.2 Non-Dimensional Parameters 85

7.3 Numerical Analysis Using CFX 87

7.3.1 Determining the Instability Threshold 88

7.3.2 Grid Independence 89

7.3.3 Domain Symmetry Boundary Condition Effects 90

7.3.4 Enlarged Plena 93

7.3.5 Fast Fourier Transform 94

7.3.6 Temporal Independence 95

7.3.7 Fast Fourier Transform of Numerical Data 98

7.3.8 Present CFX Predictions of Threshold Mass-flow Rates and Period of Oscillation with Wall Thermal Energy Storage Effects 101

7.3.9 Comparison of With and Without Wall Thermal Energy Storage Effects using Dimensionless Parameter N_{TPC} 104

8. Chapter 8 Conclusions and Recommendations 105

8.1 Conclusions 105

8.2 Recommendations 107

References 109

List of tables

Table 2.1 Parallel Channel Literature review 15

Table 2.2 Literature with wall energy storage effects..... 25

Table 3.1 Experimental cases from (Xiong et al. 2012) 31

Table 3.2 Experimental cases from Xi et al. (2014) with uniform axial power 32

Table 4.1 Stability criteria of a Bode plot..... 45

Table 6.1 INCONEL 625 Properties ("Inconel 625 Tech Data") 69

Table 6.2 Mesh statistics..... 72

Table 7.1 Present study linear solution results compared with the Xiong et al. (2012) experiments 76

Table 7.2 Comparison between experiment and present study with and without wall thermal energy storage effects. 77

Table 7.3 Comparison of LPB between experiment and present study with and without wall thermal energy storage effects 78

Table 7.4 Comparison of IB between experiment and present study with and without wall thermal energy storage effects 79

Table 7.5 Comparison of HPB between experiment and present study with and without wall thermal heat storage effects. 81

Table 7.6 Single channel cases (Pressure: 23 MPa, inlet temperature: 513K) 83

Table 7.7 Comparison of the period of oscillation of experimental and numerical 84

Table 7.8 Instability threshold of the CO_2 numerical cases..... 85

Table 7.9 Converted Water cases using Non-dimensional parameters..... 86

Table 7.10 Comparison between threshold boundary power from non-dimensional parameters and the Linear code results 87

Table 7.11 Grids used for mesh independence study 89

Table 7.12 Half model vs Full model 92

Table 7.13 Threshold mass flow rate predictions with wall thermal energy storage 103

Table 7.14 N_{TPC} comparisons between numerical simulations and experimental results..... 104

List of Figures

Figure 1.1 Nuclear reactor development timeline ("Generation IV Reactor" 2018) 2

Figure 1.2 Schematic of SCWR design (OECD 2000) 4

Figure 1.3 Phase diagram of water (Pioro and Mokry 2011) 5

Figure 1.4 Supercritical water properties (a) Specific heat variation, Volume expansivity , thermal conductivity (b) Density, Thermal conductivity, fluid enthalpy, Prandtl number (Pioro and Mokry) 6

Figure 3.1 Schematic of the NPIC experimental setup (a) Front view (b) Side view (Xiong et al. 2012) 29

Figure 3.2 Equivalent geometry (Xiong et al. 2012) 30

Figure 3.3 Xi et al. cases with axial decreasing power profile at 23 MPa (a) Summary of cases (b) Power profile (Xi et al. 2014) 33

Figure 4.1 Bode plot (Case 3 instability boundary) 45

Figure 4.2 Schematic diagram of model used in Linear 1D analysis. 46

Figure 6.1 Parallel channels schematic 54

Figure 6.2 (a) Lower Plenum (b) Upper plenum 55

Figure 6.3 Channel, orifices and riser 55

Figure 6.4 Wall 56

Figure 6.5 Equivalent geometry used in ANSYS CFX 18.2 56

Figure 6.6 a) O-Grid sample b) edge sizing conditions used for O-grid 70

Figure 6.7 Plenum mesh (a) Isometric View (b) Detailed near channel 71

Figure 6.8 Domain declaration 73

Figure 7.1 Summary of instability threshold [1] Xiong et al. [2] Xi et al. (Uniform Power cases) 77
Figure 7.2 Experimental LPB cases versus 1D analytical With and without wall energy storage effects 79
Figure 7.3 Experimental IB cases versus 1D analytical With and without wall energy storage effects 80
Figure 7.4 Experimental IB cases versus 1D analytical With and without wall energy storage effects 82
Figure 7.5 Summary of Xi et al. Cases (Non-uniform power profile) 82
Figure 7.0.6 Stability of systems 88
Figure 7.7 Channel 1 Oscillations (With wall, Xiong's Case 1- 0.0334 kg/s) 90
Figure 7.8 (a) Half model (Li 2016) (b) Full model 91
Figure 7.9 Full model versus Half model for Xiong et al. Case 1 at 0.0334 kg/s 92
Figure 7.10 Contours in the upper plenum (a) small plenum case, and (b) large plenum case 93
Figure 7.11 Fast Fourier transform of Xiong's experimental Case 1 95
Figure 7.12 Comparison of different timestep results (Half geometry, Case 1, 0.0338 kg/s) 96
Figure 7.13 Normalized mass flow rate for channel 1 at 0.0338 kg/s using various timestep sizes 97
Figure 7.14 FFT analysis of Li (2016) Case 1 (First order transient scheme and Second order transient scheme) 98
Figure 7.15 FFT analysis of CFX results of Xiong et al. Case 1, with and without wall thermal energy storage effects (First order transient scheme, Full geometry, 0.0334 kg/s) 99
Figure 7.16 FFT results of CFX Case 1 with wall thermal storage effects 100

Figure 7.17 Normalized mass flow rate for Xiong et al. Case 9 - 0.0365 kg/s (unstable) versus 0.0370 kg/s (stable) 102

Figure 7.18 Normalized inlet and outlet mass flow rates for Xiong et al. Case 9 103

Nomenclature

A, A_c	cross section area (m^2)
A_s	surface area (m^2)
a_P	representative coefficient of a control volume
a	matrix containing the coefficients of the coupled system of linear equations
b	vector on the right hand side of the coupled system of linear equations
C	a log-layer constant depending on wall roughness (C = 5.2 for a smooth wall)
C_k	friction coefficient in momentum equation
C_p	specific heat capacity (J/kg K)
$c_\mu, c_{\varepsilon 1}, c_{\varepsilon 2}$	turbulence model constants
D	outer diameter (m)
f_r	friction factor
G	mass flux (kg/s)
g	gravitational acceleration (m/s^2)
$\dot{g}$	heat generated (W/m^3)
G_c	transfer function
G_s	characteristic equation
h	static enthalpy (J/kg)
H	height of section, (m)
h_{tot}	total enthalpy (J/kg)

h_c	heat transfer coefficient (W/m^2K)
h_f	enthalpy of fluid (kJ/kg)
I	turbulence intensity
K	K- factors of channels
k_w	thermal conductivity of wall material (W/mK)
k	turbulence kinetic energy, (m^2/s^2)
K	local pressure drop coefficient
L	channel length (m)
$\dot{m}$	mass flow rate (kg/s)
N_{node}	total number of nodes of a mesh element
P	pressure (Pa)
P'	modified pressure, (Pa)
P_{abs}	absolute pressure, (Pa)
P_k	turbulence production due to viscous forces, $kg/(m \cdot s^3)$
P_{kb}	turbulence production due to buoyancy, $kg/(m \cdot s^3)$
Pr	Prandtl number
Pr_t	turbulent Prandtl number
P_{tot}	total pressure, (Pa)
$P_{\varepsilon b}$	turbulence dissipation due to buoyancy, used in k-ε turbulence models, ($kg/(m \cdot s^3)$)
$P_{\omega b}$	turbulence dissipation due to buoyancy, used in the SST turbulence model, ($kg/(m \cdot s^3)$)

ΔP_f	pressure drop due to friction, (Pa)
ΔP_l	pressure drop due to local resistance, (Pa)
ΔP	pressure drop, (Pa)
Q_w	heat transferred to fluid (W)
q_w	volumetric heat (W/m^3)
r	radius (m)
s	frequency (Complex variable = iω) (1/s)
T	temperature (K)
t	time (s)
t_w	wall thickness (m)
ΔU	change in internal energy (J)
u,w	velocity (m/s)
W	power supplied to the channel (W)
x,z	length (m)
x_s	control volume (m)

Greek letters

α	thermal diffusivity ($k/\rho C_p$)
β	isobaric thermal expansion coefficient (K^{-1})
∇	vector differential operator
Δ	difference between two quantities
δ_{ij}	Kronecker delta function

λ_t	turbulent thermal conductivity (W/m·K)
μ_t	eddy viscosity (Pa·s)
ν_t	turbulent kinematic viscosity (m^2/s)
ρ_{ref}	reference density (kg/m^3)
$\sigma_\varepsilon, \sigma_k$	model constants for *k* and ε equations
τ_{ij}	shear stress (N/m^2)
τ_w	shear stress at the wall (N/m^2)
φ_{range}	representative value of the overall range in the solution variable
π_h	perimeter (m)
ρ	density (kg/m^3)
τ	wall thickness (m)
δ	surface roughness (m)
ε	turbulence dissipation rate (m^2/s^3)
ε_n	conversion factor (kg-K/kJ)
θ	angular position in a cylindrical coordinate system (rad)
κ	Von Kármán constant
μ	dynamic viscosity (Pa·s)
ν	kinematic viscosity (m^2/s)
ρ	density (kg/m^3)
$\rho\overline{u_i u_j}$	Reynolds stress (N/m^2)
τ	magnitude of shear stress (N/m^2)
φ	generic solution variable

Φ	heat generated (W/m^3)
ω	frequency (1/s)

Subscripts

1	channel 1
2	channel 2
f	fluid/bulk
in1	inlet of channel 1
in2	inlet of channel 2
m	mean
o	steady state
out1	outlet of channel 1
out2	outlet of channel 2
w	wall
c	critical
f	friction
g	gravity
in	inlet
ip	integration Point
l	local
max	maximum
min	minimum

nb	neighbour
norm	normalised
out	outlet
pc	pseudo-critical
thold	threshold
tot	total

Superscript and accent

′	perturbed variable
~	Laplacian of variable

Acronyms

BWR	Boiling Water Reactor
CFD	Computation Fluid Dynamics
DNS	Direct Numerical Simulation
DWO	Density Wave Oscillation
GFR	Gas-Cooled Fast Reactor
GIF	Generation IV International Forum
LFR	Lead-Cooled Fast Reactor
LWR	Light Water Reactor
MSR	Molten Salt Reactor
NPIC	Nuclear Power Institute of China

PWR	Pressurized Water Reactors
RANS	Reynolds Averaged Navier-Stokes
RELAP 5	Reactor Excursion and Leak Analysis Program
SCWR	Supercritical Water Cooled Reactor
SPORTS	Special Predictions of Reactor Transients and Stability
SFR	Sodium-Cooled Fast Reactor
UDS	Upwind Difference Scheme
VHTR	Very High Temperature Reactor

Non -Dimensional parameters

N_{SUBPC}	sub-pseudocritical number
N_{TPC}	true trans-pseudocritical numbers
Nu_b	Nusselt number
Re_b	Reynolds number
Pr_b	Prandtl number

Chapter 1

Introduction

1.1 Nuclear energy

Growth in the world's population and economy, coupled with rapid urbanisation, will result in a substantial increase in energy demand. The United Nations (UN) estimated that the world's population will grow from 7.6 billion in 2017 to 9.8 billion by 2050 (United Nations, 2017). The challenge of meeting this rapidly growing demand, whilst reducing emissions of greenhouse gases, is very significant. In 2016, global atmospheric concentrations of CO_2 rose by 0.8%, the largest annual rise ever observed. So far, fossil fuels (lignite, coal, oil and natural gas) have been the main energy source. However, it is unrealistic to depend on the combustion of fossil fuels, which are non-renewable and finite, for indefinite human energy consumption. Large-scale combustion of fossil fuels increases the emission of greenhouse gases (mainly carbon dioxide) with serious environmental consequences and health risks caused by pollution. Hence, it is deemed necessary to minimize the consumption of fossil fuels.

Electrical energy is one of the most important forms of energy used in the world. Since nuclear energy has already been used worldwide for electricity generation, with satisfactory performances increasing the construction of nuclear power plants for electricity supply is a viable, effective and logical way to reduce fossil-fuel-based energy consumption. Nuclear power plants produce less pollution than many other current energy sources, including coal fire and natural gas plants. Also, the nuclear energy source is more efficient than solar, coal and wind energy. Additionally, the level of possible radiation exposure from nuclear power plants is less than we are currently exposed to

on a daily basis, from the environment. Another reason for using more nuclear energy is that it is a cheaper source of energy than gasoline, a fuel source that has been troubling for our economy for many years. Nuclear power plants provided 11 % of the world's electricity in 2014. In 2016, 13 countries relied on nuclear energy to supply at least one-quarter of their total electricity. As of April 2017, 30 countries worldwide operate 449 nuclear reactors for electricity generation and 60 new nuclear plants are under construction in 15 countries (Nuclear Energy Institute, 2017). Currently, the majority of the first-generation nuclear reactor systems are retired, second generation reactor systems are the main reactors in operation and only about 12 Generation III reactors are in operation.

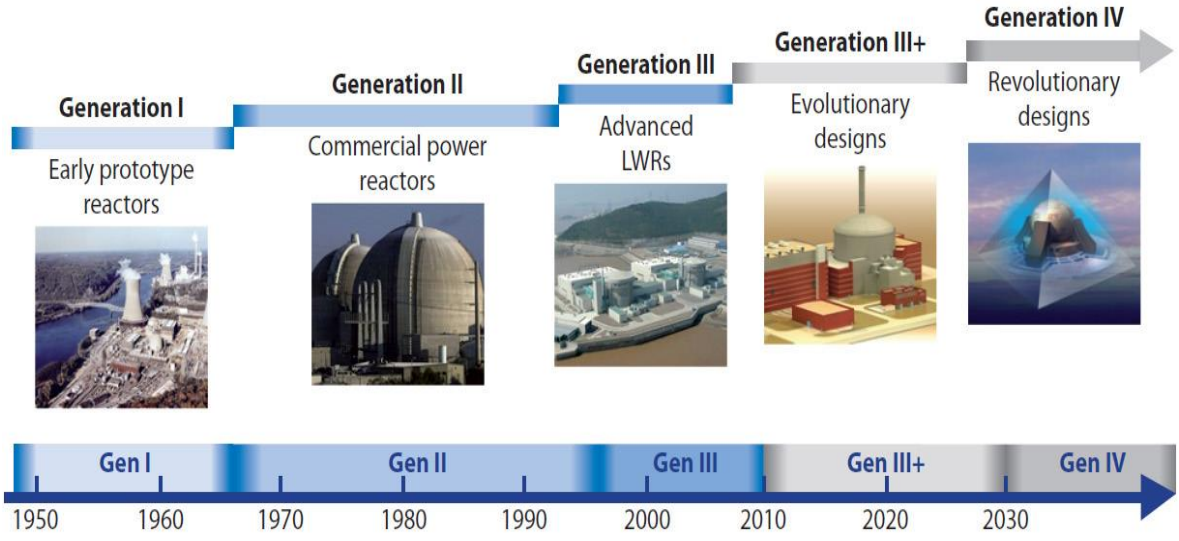

Figure 1.1 Nuclear reactor development timeline ("Generation IV Reactor" 2018)

A new and innovative generation of nuclear power reactors, Generation IV reactors, are proposed and being researched. Figure 1.1 explains the timeline of nuclear power reactor development.

1.2 Supercritical water-cooled reactor

As part of the Generation IV initiative, the International Forum chose six proposed nuclear reactor designs, namely; the Gas-Cooled Fast Reactor (GFR), the Sodium-Cooled Fast Reactor (SFR), the Lead-Cooled Fast Reactor (LFR), the Very High Temperature Reactor (VHTR), the Molten Salt Reactor (MSR), and the Supercritical Water-Cooled Reactor (SCWR) for research.

The Generation IV International Forum (GIF) was founded in 2001. It currently consists of ten active members (Canada, China, the European Atomic Energy Community (Euratom), France, Japan, Russia, South Korea, South Africa, Switzerland and the United States) and three non-active members (Argentina, Brazil and the United Kingdom). The Supercritical Water- Cooled Reactor (SCWR) uses light water at supercritical conditions ($P \geq 22.06$ [MPa] and $T \geq 373.946$ [ºC]) as the working fluid. Making full use of the technologies in supercritical water-cooled fossil-fired power plants, the thermal efficiency of SCWRs is expected to reach 44% or more, compared to 34-36% for current reactors (OECD 2000). A SCWR would work at an elevated temperature level (Above 373.95°C). Additionally, reactor coolant pumps may not be required. The only pumps driving the coolant under normal operating conditions will be the feed water pumps and the condensate extraction pumps. Consequently, this compact design of SCWRs does not only significantly simplify power plants, but is also economical. As in a boiling water reactor, the superheated steam will be supplied directly to the high-pressure steam turbine and the feed water from the steam cycle will be supplied back to the core. Thus, the SCWR concepts combine the design and operation experiences gained from hundreds of water-cooled reactors with those experiences from hundreds of fossil-fired power plants operating with supercritical water (SCW). In contrast to some of the other Generation IV nuclear systems, the SCWR can be developed incrementally step-by-step from current water-cooled reactors. Figure 1.2 is the schematic of a SCWR design.

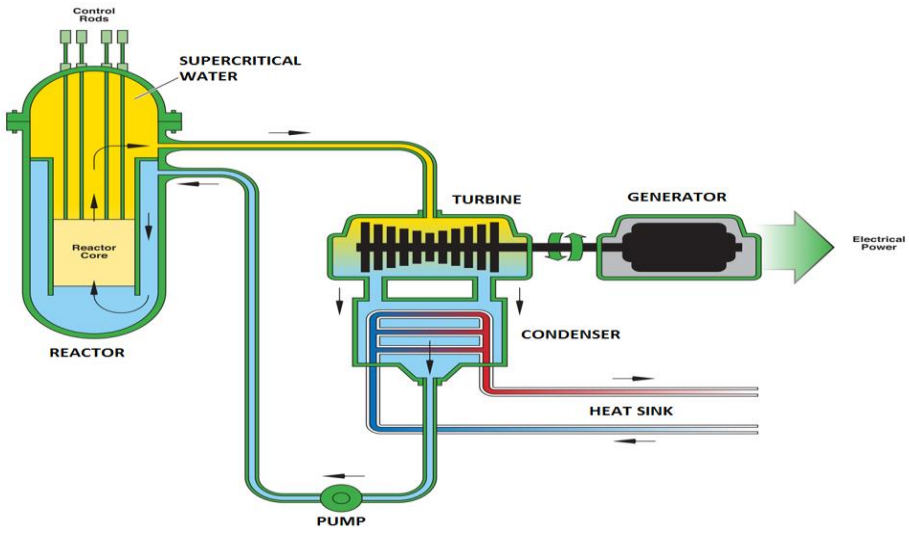

Figure 1.2 Schematic of SCWR design (OECD 2000)

The proposed design of a SCWR offers the potential of lower capital costs and better fuel efficiency (OECD, 2000). Several technological challenges are associated with the development of the SCWR, particularly the need to validate transient heat transfer models (for describing the depressurization from supercritical to sub-critical conditions), qualification of materials (namely advanced steels for cladding), and demonstration of the passive safety systems. Because of all the challenges, the technological development of SCWRs is still undergoing. According to the system development timelines in the GIF 2014 Technology Roadmap, the licensing, construction and operation of a prototype or demonstration SCWR system are likely to start around 2025, followed by another 10 years to deal with details, and then SCWRs are expected to be available for commercial construction(OECD, 2000) .

1.3 Supercritical Water Properties

The critical point or critical state is the point at which two phases of a substance initially become indistinguishable from one another. The critical point is the end of a phase equilibrium curve,

defined by a critical pressure P_{cr} and critical temperature T_{cr}. At this point, there is no phase boundary. For water, the pressure and temperature at the critical point are 22.06 MPa and 373.9 °C, respectively. When a fluid is compressed above its critical pressure and heated above its critical temperature, the fluid is said to be supercritical and exists as a single phase. At the critical point, the densities of liquid and vapor are identical. Figure 1.3 shows the phase diagram of water.

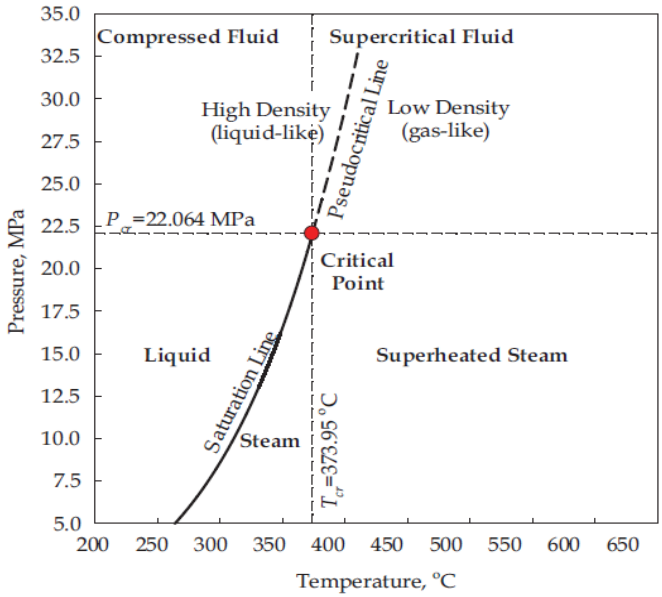

Figure 1.3 Phase diagram of water (Pioro and Mokry 2011)

In the supercritical fluid region, at any given pressure there is a corresponding pseudocritical temperature (Represented by the Pseudocritical line). The pseudocritical temperature corresponds to the maximum value of the fluid specific heat capacity, C_p. As shown in figure 1.4-(a), for each supercritical pressure, there is a spike of C_p at a unique pseudocritical temperature. In addition, the spike is largest when the pressure is close to the critical pressure. The magnitude of the spike decreases with increase in pressure. When the working condition approaches the critical or pseudocritical point, water properties undergo sharp changes. Figure 1.4-(b) illustrates properties variations of supercritical water at a supercritical pressure of 25 MPa. It is observed that, properties such as density and dynamic viscosity undergo a significant drop (near the critical point this drop

is almost vertical) within a very narrow temperature range (Figure 1.4-(b)), while the kinematic viscosity and fluid enthalpy undergo a sharp increase (Figure 1.4-(b)). The volume expansivity, specific heat, thermal conductivity and Prandtl number have peaks near the critical and pseudocritical points (Figure 1.4). Magnitudes of these peaks decrease very quickly with an increase in pressure. Also, "peaks" transform into "humps" at pressures beyond the critical pressure.

(a)

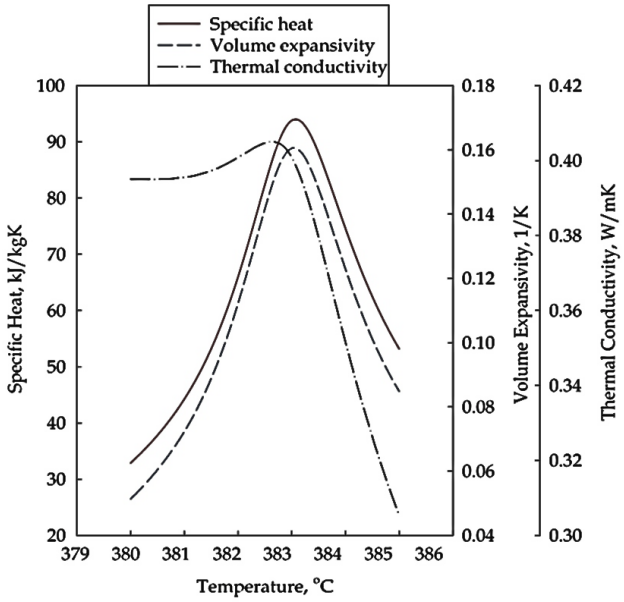

(b)

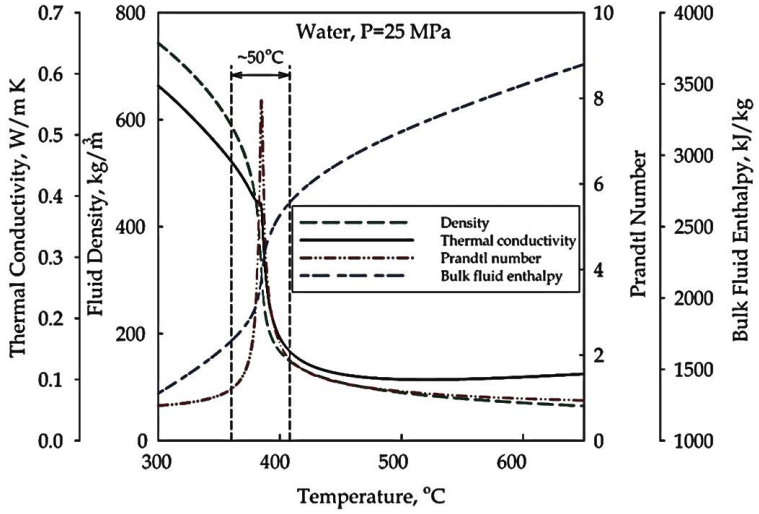

Figure 1.4 Supercritical water properties (a) Specific heat variation, Volume expansivity , thermal conductivity (b) Density, Thermal conductivity, fluid enthalpy, Prandtl number (Pioro and Mokry)

1.4 Supercritical Flow Instability

Despite the benefits of SCWRs listed, sharp changes of water physical properties (mainly the significant change of density) happen when the water temperature transitions through the pseudocritical point. This can result in thermal hydraulic instabilities. Flow instabilities in a nuclear reactor must be avoided, as a mandatory safety requirement, as the sustained oscillations in flow may lead to mechanical vibrations of components and degrade system control and may even result in mechanical damage of the whole nuclear reactor. With regards to the stable or unstable states of the flow, it is mainly distinguished by the fluid reaction after a disturbance in the initial steady state. If the disturbance has a negligible influence on the initial steady state of the flow system and dies down gradually with time, then the flow is deemed to be stable. Otherwise, the flow is unstable. For an unstable flow with dynamic instabilities, the mass flow rate oscillates with growing amplitudes. To predict dynamic instability thresholds, analyses of time-dependent (transient) characteristics of the system are required. In the present study, oscillatory instabilities with mass flow rate oscillations are investigated.

1.5 SCWR Modeling

For oscillatory instabilities in SCWRs, three typical classifications were proposed (Zhao, 2005). The first case is single channel oscillations where only one channel or a small part of parallel channels in the fuel assemblies oscillate while the other channels stay steady. This kind of instability can be modeled by a single channel with constant pressure drop boundary conditions. The second case is named as out of phase or region-wide instability. During this case of oscillation,

about half of the core oscillates with a 180° shift to the other half. A two-parallel-channel system with constant total mass flow rate can be used as the physical model for this kind of instability. The third case is called the core-wide in-phase instability, in which all channel flows oscillate in phase, leading to an oscillation throughout the core and the whole loop. This kind of oscillation can be modeled as circulation loop instability. Most investigations on supercritical flow instabilities are focused on the above three cases and can be divided into major two configurations: parallel-channel systems, and circulation loop. A review of the relevant experiments and numerical studies will be presented in the next chapter.

In this study, mainly the second kind of instability with a two-parallel-channel system model is studied numerically considering wall thermal energy storage effects by using the SPORTS code (Chatoorgoon, 2001), linear 1D code (Chatoorgoon and Upadhye, 2005) and a CFD code – ANSYS CFX R18.1.

Chapter 2

Literature Review

The Gen-IV Supercritical water reactor (SCWR) was proposed due to its promising high thermal efficiency (from 33–35% to 45% or more) and comparatively lower cost. The investigation into the use of supercritical water in a nuclear reactor as a coolant started at the end of the 1950s, but it gained popularity late in the 1990s. Intensive work on the concept of the supercritical water-cooled reactor began by countries like Canada, Germany, Italy, Russia, India, Korea, Japan, China (I. L. Pioro and Duffey, 2005; Oka and Koshizuka, 2001; Gabaraev et al., 2003). The fuel bundle arrangement in Canada's CANDU reactors is horizontal, while the Euratom (Europe and Japan) contribution to the Generation IV International Forum (GIF) is the high-performance light water reactor (HPLWR), which has a vertical orientation of its core. Also, Canada's SCWR design has a vertical core. Regardless whether the reactor core is horizontal or vertical, any flow oscillations in the parallel channels of a fuel bundle, or between the feeders connecting the inlet and outlet headers, would be deemed undesirable. In the SCWR loop design, water leaves the core at a pressure of approximately 25 MPa and temperatures above 500°C. Despite of the benefits of SCWRs, supercritical water experiences sharp density changes around the pseudocritical point, which can trigger a thermal hydraulic instability. Hence, the stability of supercritical water-cooled reactor was recognized as a critical issue to be accessed. Thus, the flow stability of a natural circulation loop and parallel channels received attention over the last decade. As the fuel bundles in a nuclear reactor comprise many parallel channels, and there are many parallel feeders connected by common headers, understanding supercritical flow stability in parallel channels would be important for reactor design. All the previous studies of parallel channel thermal

hydraulic instability of supercritical flow are categorized into two major parts: literature without wall thermal energy storage effects and with wall thermal energy storage effects.

2.1 Instability Studies of Parallel Channels

2.1.1 Literature Without Wall Thermal Energy Storage Effects

The theoretical research on flow instability in the subcritical region began with Zuber (Zuber, 1966), who developed three region models with regions namely liquid, transition and perfect gases. He used perturbation theory and linearized governing equations to study the conditions leading to aperiodic and periodic flow oscillations. D'Auria et al. (1993) presented an analysis of new generation plants. They concluded that the thermal hydraulic instability occurring in several parallel loops largely depends upon local loss coefficients in complex three-dimensional geometries. Following Zuber, Zhao (2005) proposed a three-region model for the heated channel, which included the so-called "light fluid region", "heavy and light fluid mixture region", and "heavy fluid region". Stability maps were constructed with the dimensionless pseudo sub-cooling number and expansion number. Based on the stability maps, the effects of the inlet orifice, inlet flow, system pressure, and inlet temperature on the single channel instability were assessed and reported. Chatoorgoon and Upadhye (2005) presented at the NURETH-11 conference a frequency domain linear solution to validate the non-linear SPORTS results. The same solution is extended for parallel channels in this study.

Gómez et al. (2008) stated that, while density-wave oscillations (DWO) can occur, Ledinegg excursive instabilities and pressure drop oscillations (PDO) will not occur in supercritical parallel-channel systems. New non-dimensional parameters for the neutral stability plane were derived for supercritical water. These non-dimensional numbers were reduced to the well

known N_{PCH} and N_{SUB} of phase change systems. Both linear and non-linear analyses were performed by utilizing these newly defined parameters. It was also concluded that use of approximate state equations, having linear slopes, can lead to an overly conservative neutral stability boundary. Ambrosini and Sharabi (2008) also derived non-dimensional parameters for supercritical fluids in heated channels. Unlike the parameters developed by Zhao (2005), these new dimensionless parameters, trans-pseudo-critical number and sub-pseudo-critical number, adopted the pseudo-critical point as the only reference state. This was later proved to be a success by Ambrosini (2011). These new non-dimensional parameters are applicable to other supercritical fluids such as CO_2, R23 and Ammonia. Besides the analytical and numerical methods mentioned above, computational fluid dynamics (CFD) has been used as a tool in supercritical flow instability analyses. Sharabi, Ambrosini (2008) performed an instability study using FLUENT for supercritical water flowing inside a single heated channel. The standard k-ε model with wall functions and a more detailed low-Reynolds number model were able to predict the onset of unstable behavior in close agreement with predictions of one-dimensional models. Hou et al. (2011) used linear and non-linear 1-D methods to investigate the stability performance of parallel channels of a newly designed mixed-spectrum SCWR (SCWR-M). A frequency-domain model was developed and marginal stability boundaries for the parallel-channel system with multiple channels were generated, which indicated that the system normal operational condition was in the stable region. It was also mentioned that the stability of parallel channels was mostly determined by the hottest channel.

Even though numerical modeling of the single channel is considered a better option to save computational time, it is almost impossible to conduct a single channel experiment without having a bypass channel. However, two parallel channels can be studied experimentally and this was done

by Xiong et al. (2012) and Xi et al. (2014). Xiong et al. (2012) presented nine instability cases of parallel channel supercritical water with pressure ranging from 23 MPa – 25 MPa and temperature ranging from 453 K to 513 K. This experimental study provided important data for validation of thermal-hydraulic codes especially in the field of stability of parallel channel systems with a supercritical fluid. Xi et al. (2014) presented cases with a thicker wall structure using the same experimental loop of Xiong et al. (2014), and they also studied the effect of axial power shape on the instability boundary. Five cases with uniform power distribution and seventeen cases with non-uniform power profile were presented. This was the first attempt of an experimental study in parallel channels with non-uniform axial power. The power distribution used was unrealistic, from a reactor point of view. These experiments were modelled using 1D in house codes (Xiong et al., 2013). The maximum relative error between code predictions and experimental results was found to be -12%. A numerical analysis using the 3D code ANSYS CFX was also carried out for Xiong et al. experimental cases. In their 3-D numerical simulation, Xi et al. (2014) determined that it was difficult to decide the best numerical model. Based on CFD engineers' experience, they adopted a higher order difference scheme and a shorter time step to obtain more accurate results. A mesh count of only 300,000 nodes was used. The k-ε model was used for computational time expediency. They concluded that the 3D predictions of the instability boundary were more accurate than their 1D solutions. An independent CFD study by Li (2016) disagreed with these findings. A series of investigations were conducted by Ampomah-Amoako et al. (2013) with the STAR-CCM+ CFD code, the 1-D RELAP5/MOD3.3 code, and an in-house linear code, covering from the simple circular pipe models to more realistic 3-D rod bundle sub-channels. The instability threshold predictions and oscillation periods, obtained by the different models, showed that flow instability is characterized mainly by 1D behavior, even though the application of CFD can

provide details that are impossible for the 1D approach to provide. Feng et al. (2013) used finite difference method to solve the area averaged conservation equations to study the effect of channel diameter, pressure, inlet temperature on thermal hydraulic boundary threshold of two parallel channels. The flow instability in parallel two-channel system were investigated. Mathematical–physical models were established to analyze the flow instability under supercritical pressure using time-domain method. It was concluded that the stability of the parallel channels is mainly dominated by the pressure drop.

A numerical study was performed for 3-D axisymmetric turbulent flow of supercritical water flowing upward in a vertical pipe with constant applied wall heat flux using ANSYS CFX by Ebrahimnia et al. (2016). Analyses of static and oscillatory flow instabilities were performed using the standard k–ε model with a scalable wall-function and the k–ω based SST model. The instability threshold results of the CFD code were compared to 1-D non-linear code predictions. Also, criteria for approximating the thresholds of static and oscillatory instabilities based on steady-state results were assessed and discussed. Comparisons of instability threshold predictions between CFD and 1-D codes showed smaller differences for static instabilities and greater differences for oscillatory instabilities. A 3-D numerical study of the turbulent flow of supercritical water flowing upward in two heated parallel channels with constant applied wall heat flux (experimental cases of Xiong et al.) was done using a RANS model in the Computational Fluid Dynamics (CFD) code ANSYS CFX by Li et al. (2018). It was concluded that the 1-D results did better than the 3-D CFX results, which contradicted the conclusion of Xi et al. (2014) . It was also mentioned that the transient responses of the second order transient scheme were not smooth as compared with the transient response of the first order transient scheme, and it took a much longer time to capture an identifiable oscillation pattern. A recent study discussed the flow instability in parallel channels at

supercritical pressures using a three dimensional (3D) numerical tool STAR-CCM+ (Shitsi et al., 2017). The amplitude and period of out-of-phase inlet mass flow oscillation at the heated channel inlet, and the maximum heated channel outlet temperature oscillation were discussed. The flow oscillation period and amplitude were found to change with the time-step used, which clearly indicated that temporal convergence was not achieved.

Table 2.1 summarizes the literature on parallel channel without wall energy storage effects.

Table 2.1 Parallel Channel Literature review

Reference	Methodology	Procedure	Findings and Comments
Zhao (2005)	- 1D-Linear (Frequency domain) - Analytical -	- For BWR and SCWR stability, analytical and numerical results were compared.	- Proposed a three-region model for heated channels similar to Novak Zuber 1966, which included the so-called “light fluid region”, “heavy and light fluid mixture region”, and “heavy fluid region”. - Stability maps were constructed with the pseudo sub-cooling number and expansion number.
Chatoorgoon (2008)	- Analytical - 1D- Non-linear (Time domain)	- Two horizontal parallel channels were numerically analysed using non-linear SPORTS and a point heat source model.	- Non-dimensional parameters defining instability boundaries were analytically derived. - Importance of accuracy of state equations was emphasized. - This study pioneered the research in parallel channels.

Table 2.1: Parallel Channel Literature review (Continued)

Reference	Methodology	Procedure	Findings and **Comments**
Gómez et al. (2008)	- 1D-Linear (Frequency domain) - 1D-Non-linear (Time domain)	Steady state, linear and non-linear stability analyses of water flowing through a uniformly heated pipe at supercritical pressure have been performed using FEMLAB 3.1.	- It was stated that while density-wave oscillations (DWO) can occur, Ledinegg excursive instabilities and pressure drop oscillations (PDO) will not occur in supercritical water systems.at
Hou et al. (2011)	- 1D-Linear (Frequency domain) - 1D-Non-linear (Time domain)	- The dynamic stability characteristics of the fast-spectrum zone of a newly designed mixed-spectrum SCWR (SCWR-M), which is characterized as a parallel-channel system was studied. - Using the frequency-domain model, the system linear stability maps were constructed.	- It is verified that the fast zone of SCWR-M design is stable in a wide range of operating conditions. - The non-linear and linear code results were found to be in good agreement with each other. - It was mentioned that “stability of parallel channels was mostly determined with the hottest channel”, which can be untrue since the stability of parallel channel depends on the difference in pressure perturbation of the channels.

Table 2.1: Parallel Channel Literature review (Continued)

Reference	Methodology	Procedure	Findings and **Comments**
Xiong et al. (2012)	- Experimental (Uniform axial power distribution)	- Nine instability cases of parallel channel supercritical water with pressure ranging from 23 MPa – 25 MPa and temperature ranging from 453 K to 513 K were presented. - A study of parametric effects on supercritical flow instability was performed.	- Parametric studies show that the flow becomes more stable with increasing pressure or decreasing inlet temperature in the range of present experiments. - These experimental study, provided a systematic and important data for validation of thermal-hydraulic codes especially in the field of stability of parallel channel systems (Similar to SCWR) with the supercritical fluid.
Xiong et al. (2013)	- 1D – Non-linear - (Time domain)	- Parametric effects on supercritical flow instability are numerically analyzed. - Comparison between the numerical and experimental results (Xiong et al. 2012) was discussed	- The results showed that the entrance and riser sections cannot be eliminated with respect to numerical modeling of flow stability and a relative simple as well as the common geometrical model was proposed for making the experimental results readily available for numerical analysis of supercritical stability. - The maximum relative error was recorded as 12% which was higher than the experimental uncertainty, which may arise the question of in house code capability.

Table 2.1: Parallel Channel Literature review (Continued)

Reference	Methodology	Procedure	Findings and **Comments**
Feng et al. (2013)	- 1D Non-linear (Time domain)	- Mathematical and physical models were established to simulate the flow and the heat transfer characteristics of supercritical water with the semi-implicit scheme and staggered mesh scheme.	- The parametric relation of inlet temperature, pressure, mass-flow rate is stated. - It was also mentioned that "the stability of the parallel channels is mainly dominated by the pressure drop."
Ampomah-Amoako et al. (2013)	- CFD STARCCM+	- The results obtained by a 3D model obtained by the 1D RELAP5 code; the steady-state characteristics of the two models were considered and the thresholds of instability identified by transient calculations were compared with maps set up by an in-house 1D code.	- Both static and dynamic instabilities are observed, in similarity with previous analyses performed for circular channels. - The work represents a further step in a research aimed to establish a methodology for the analysis of flow stability in nuclear reactor cores by CFD codes.

Table 2.1: Parallel Channel Literature review (Continued)

Reference	Methodology	Procedure	Findings and **Comments**
Xi et al. (2014)	- Experimental - (Uniform and non-uniform axial power distribution)	- Cases with thicker wall structure using a same experimental loop of Xiong were done. - The effect of axial power shape on the instability boundary was studied.	- Although thick INCONEL 625 circular pipes which were thought to make the system more stable were used in the experiment, out of phase flow instability occurred. - Period and maximum inlet mass flow rate amplitude are not so sensitive to the axial power distribution. - Even this was the very first attempt of experimental study with non-uniform axial power, the power distribution used was unrealistic and would hardly occur in SCWR core.
Xi et al. (2014)	- CFD Ansys CFX	- A three dimensional (3D) numerical simulation is carried out using the CFX code to investigate the out of phase oscillation between two heated parallel channels with supercritical water. - A parametric study of numerical models like SIMPLE, SIMPLEC, PISO was done.	- It was mentioned that the oscillation period was higher than the experimental period. - A mesh count of only 3,00,000 was used. Also, the k-e model was used to save the computational time. - The 1D code gives better predictions than 3D was later proved by Li et al. which was contradictory to the conclusion in this study.

Table 2.1: Parallel Channel Literature review (Continued)

Reference	Methodology	Procedure	Findings and **Comments**
Dutta et al., (2015)	- 1D Non-linear (Time domain)	- A 1D code was extended for parallel channels in the reactor core to determine both in-phase and out-of-phase modes of oscillations considering the origination of the instabilities purely due to the thermal-hydraulic feedbacks.	- Asymmetric heating power can significantly reduce the instability threshold for the CANDU SCWR and make the reactor less stable with the increase in the heating power asymmetric level for both the in-phase and out-of-phase modes of DWOs.
Ebrahimnia et al. (2016)	- CFD ANSYS CFX	- Analyses of static and oscillatory flow instabilities are performed using the standard k–e model with a scalable wall-function and the k–e-based SST model. - The instability threshold results of the CFD code are compared with 1-D non-linear code predictions.	- It was observed that the instability threshold results obtained using the *k–ε* and the SST models were like 1-D results. - The k-e model was recommended for stability predictions which is important for further investigations using RANS models.

Table 2.1: Parallel Channels Literature review (Continued)

Reference	Methodology	Procedure	Findings and **Comments**
Edward Shitsi et al. (2017)	- CFD STAR CCM+	- The dynamics characteristics such as amplitude and period of out-of-phase inlet mass flow oscillation at the heated channel inlet, and heat transfer characteristic such as the maximum outlet temperature of the heated channel outlet temperature oscillation were studied.	- The results showed that the system parameters have a significant effect on the amplitude of the mass flow oscillation and maximum temperature of the heated outlet temperature oscillation but have a negligible effect on the period of the mass flow oscillation. - It was also discussed that the period of oscillation and amplitude changes with the time step used, which clearly stated poor temporal convergence.

Table 2.1: Parallel Channels Literature review (Continued)

Reference	Methodology	Procedure	Findings and **Comments**
Li et al. (2018)	- CFD Ansys CFX	- A 3-D numerical study of the turbulent flow of supercritical water flowing upward in two heated parallel channels with constant applied wall heat flux of Xiong's cases was developed using a RANS model. - The effects on the instability thresholds of changing the outlet plenum volume, the turbulent Prandtl number, the turbulence inlet conditions, the channel outlet K factor, the maximum iterations per time step in the transient analysis, and the order of the transient scheme were examined.	- It was also concluded that the 1-D results were better than the 3-D CFX results, which was different from the conclusion stated by Xi et al. (Xi et al., 2014) that the 3-D CFX code predicts the onset of flow instability better than a previous 1-D code. - There was a high sensitivity of the CFX code to the time step size. - It was also mentioned that, compared with the first order transient scheme, transient responses of the second order transient scheme were not smooth, and it also took a much longer time to capture an identifiable oscillation pattern. The unsmooth curves can basically be hidden frequencies which should have been investigated.

2.2 Instability studies with wall thermal energy storage effects

Compared with the large amount of previous work on instability investigations within all configurations of single, parallel channels and natural circulation loop, the literature on supercritical flow instability with wall thermal energy storage effects is very limited.

March-Leuba pioneered the research on the effect of wall thermal energy storage on thermal hydraulic instability (March-Leuba et al., 1993). He mentioned that the inclusion of wall thermal energy storage effects prolongs the stability of a system. The combined analyses (Debrah et al., 2013a) with the RELAP-1D system code and an in-house code written in the dimensionless form and based on the non dimensional parameters allowed highlighting the importance of heat transfer to heating structures as a phenomenon contributing to stabilising natural circulation loops. They concluded that the results for the loop without heating structures were closer to the experimental values, and the addition of wall thermal energy storage effects made the instability boundary go way beyond the experimental boundary. Similar, linear and non linear analyses were carried out with three reduced thermal capacitances of the wall in a natural circulation loop (Debrah et al., 2013b). The findings of the previous study were confirmed, and it was suggested to carry all thermal hydraulic stability analyses without considering wall energy storage effects.

A closed Supercritical Pressure Parallel Channel Loop (SP-PCL) based on natural circulation with water as working fluid was proposed to be built at Bhabha Atomic Research Centre (BARC), India (Sharma et al., 2015). A one-dimensional model for simulating thermal capacitance of the pipe wall was incorporated in the NOLSTA-p code based on the same methodology used in NOLSTA-p code (Sharma et al., 2013). This code yielded worse results with wall thermal energy storage effects. A recent study on the effect of pipe wall thickness and length on density wave instability was done by Liu et al. (2018). They developed a time-domain 1D model and their results showed

that wall energy storage significantly changes the flow instability boundary. They concluded that, with no wall, the system stability decreases with the decrease in pipe length and then remains constant. They also stated that when the wall heat storage is considered, there exists a critical value of pipe length, L_{cr}, such that when pipe length is less than L_{cr}, the system stability decreases with the pipe length. When pipe length is greater than L_{cr}, the system stability increases with the pipe length. The summary of literature with wall energy storage effects is given in Table 2.2.

2.2 Objectives

The objectives of the work are,

1. To extend the 1D linear code single channel model to include wall thermal energy storage effects.
2. To extend the linear 1D code (single channel) to parallel channels with the wall thermal energy storage and compare with experimental data of Xiong et al. (2012) and Xi et al. (2014).
3. To compare the flow instability thresholds predicted by the present developed linear code with wall energy storage and with previous numerical results (1-D) of the same experiment without the wall thermal energy storage effects.
4. To rationalize the discrepancies between the experiment and different numerical simulations with the 1-D code.
5. To develop, using ANSYS CFX, a 3-D CFD model of the experiment of Xiong et al. (2012) and Xi et al. (2014) for upward flow in two heated parallel channels with and without wall thermal energy storage effects.
6. To compare the flow instability thresholds predicted by the CFX code (with and without wall thermal energy storage) with the experimental data of Xiong et al. (2012); Xi et al. (2014) and with other investigators' results.

Table 2.2 Literature with wall energy storage effects

Reference	Methodology	**Application** and procedure	Findings and **Comments**
March-Leuba et al. (1993)	- Analytical - 1D- Non-linear (Time domain)	BWR - A physical model of BWR was developed using non-linear code employed to calculate the amplitude of limit cycle.	- It was concluded that the inclusion of wall energy storage effect prolongs the stability of a system. He also noted the effects of thermal capacitance on thermal hydraulic instabilities. - March-Leuba pioneered the research on the effects of wall heat storage on thermal hydraulic instability.
Debrah et al. (2013a)	- 1D-Linear - 1D-Non-linear (Time domain)	Natural Circulation - The analysis of the natural circulation loop operated at CIAE with supercritical water by the RELAP5 code. - The combined analyses with the system code and an in-house code written in the dimensionless form was based on the non-dimensional parameters.	- The presence of heating structures was found to be very important to determine the level at which unstable behaviour could be reached. - It was concluded as the result for the loop without the heating structures are the closest ones to the experimental value, and the addition of wall energy storage effects makes the numerical boundary onset go way beyond the experimental onset. - This conclusion was contradictory to the conclusion with wall energy storage in the present study.

Table 2.2: Literature with energy storage effects (Continued)

Reference	Methodology	**Application** and procedure	Findings and **Comments**
Debrah et al. (2013b)	- 1D-Linear - 1D-Non-linear (Time domain)	Natural Circulation - Linear and non-linear analysis were carried out with three reduced thermal capacitances of the wall in a natural circulation loop.	- When heat structures are accounted for in models equipped with heat transfer and friction correlations for ‘‘normal’’ fluids, the comparison with experimental data is not completely satisfactory. - It was concluded that models with no allowance for heat structure capacity should be considered only an approximation of the real situation.
Sharma et al. (2015)	- 1D-Non-linear (Time domain)	Parallel Channels - One-dimensional model for simulating thermal capacitance of the pipe wall was incorporated in NOLSTA-p code based on the same methodology used in NOLSTA code (Sharma et al. 2014).	- The large instability zone as observed without wall vanishes by including pipe wall capacitance. - The loop is stable even near the pseudo-critical temperature range. - All the conclusions regarding wall heat in parallel channel instability by Sharma et al., 2015 are contradictory to the conclusions of this study.

Table 2.2: Literature with wall energy storage effects (Continued)

Reference	Methodology	**Application** and procedure	Findings and **Comments**
J. Liu et al. (2018)	- 1D-Non-linear (Time domain)	Single channel - A time-domain model for considering the heat storage of pipe wall was proposed to study the DWO instability of supercritical flow. - The effect of wall thickness and pipe length on DWO instability of supercritical flow was investigated.	- The result showed that the wall energy storage model significantly changes the influence rules of pipe structural parameters on flow instability. - It was concluded that, under the situation without the wall heat storage (the wall thickness is zero), system stability begins with a decrease of the pipe length and then tends to be unchanged. - Under the situation where the wall heat storage is considered (the wall thickness is greater than zero), there exists a critical value about pipe length ('L_{cr}'). When pipe length is less than L_{cr}, the system stability decreases with the pipe length. When pipe length is greater than L_{cr}, the system stability increases with the pipe length.

Chapter 3

Problem Description

To validate the numerical results with wall thermal energy storage effects, relevant experimental data were required. The oscillatory instability in a two-parallel-channel geometry with and without wall thermal energy storage effects was investigated in this study using the experiments of Xiong et al. (2012) and Xi et al. (2014). The flow conditions of these experiments are similar to the real operating conditions in a SCWR. The experimental loop and the flow conditions of Xiong et al. and Xi et al. experiments are described in this chapter.

3.1 Xiong et al. Experimental Loop (Xiong et al. 2012)

In the supercritical water loop at the Nuclear Power Institute of China (NPIC), the test section had a two-parallel-channel system which allowed up-flow. There was a lower plenum, flow meters, entrance sections, heated sections, riser sections and an upper plenum. The two heated sections were made of INCONEL Alloy pipes with inner and outer diameters of 6 and 11 mm, while the heated length was 3 m. The use of INCONEL alloy pipes ensured that the heat flux along the axis was uniform, since the resistance changes very little with temperature. Orifices were placed at the inlet and outlet of the heated sections. The whole piping was thermally insulated to minimize heat loss. Figure 3.1 presents a schematic diagram of the test section. The fluid temperatures at the inlet and the outlet of the test section were measured by sheathed N-type thermocouples. 14 sheathed N-type thermocouples were spaced along each heated pipe at seven different axial locations to measure outlet wall temperature to identify the heat transfer deterioration and measure the wall temperature near the deterioration location. Pressure measurements were made at the lower plenum, inlet of the heated sections, outlet of the heated sections and upper plenum. Heat applied to the

system was measured by means of current and voltage readings. Further details can be found in Xiong et al. (2012).

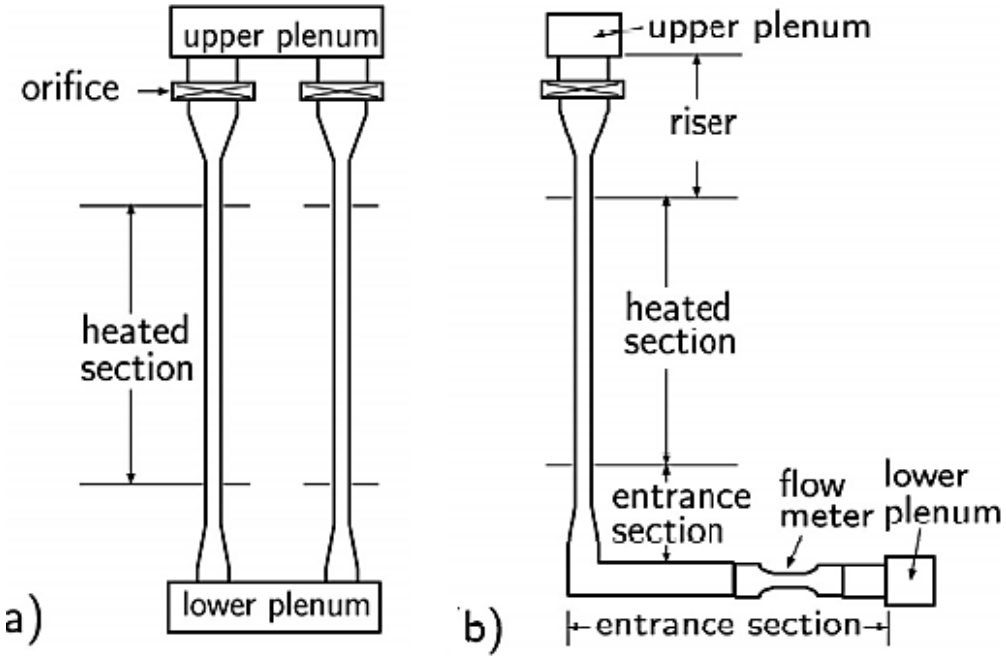

Figure 3.1 Schematic of the NPIC experimental setup (a) Front view (b) Side view (Xiong et al. 2012)

3.1.1 Equivalent Geometry (Xiong et al. 2012)

A proposed geometrical model by Xiong et al. experiment is illustrated in Figure 3.2. The simplification is made by changing the entrance and the riser sections. Pipes of various inner diameters were substituted with one pipe, which was of the same inner diameter with the heated section, and local pressure drops were assumed to be concentrated at special orifices.

During the experiments, two pressure drops were measured for each channel i.e. pressure drop from the lower plenum to the entrance of the heated section and from the exit of the heated section

to the upper plenum. Based on the pressure drops, the K factors were calculated. The K-factors of the experiments were reported to be: $K_{in1} = 5.40$, $K_{in2} = 5.50$, $K_{out1} = 4.93$, $K_{out2} = 6.46$.

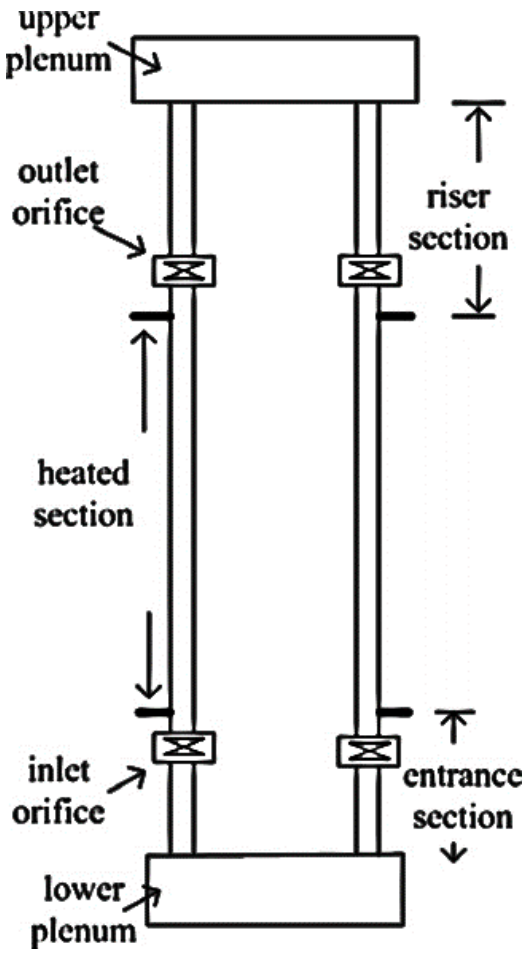

Figure 3.2 Equivalent geometry (Xiong et al. 2012)

3.1.2 Flow Conditions for the Xiong's Experiment (Xiong et al. 2012)

The experiments were performed at pressures in the range of 23 MPa to 25 MPa with inlet temperatures in the range of 453 K to 513 K. The cases are given in Table 3.1.

Table 3.1 Experimental cases from (Xiong et al. 2012)

Cases	System Pressure (MPa)	Inlet Temperature (K)	Inlet Mass Flow Rate (kg/s)	Threshold Power (kW)	N_{TPC}	N_{SPC}
1	23	453	0.0342	67.9	3.54	4.52
2	23	473	0.0333	66.0	3.52	4.48
3	23	493	0.0333	65.6	3.35	4.38
4	24	473	0.0333	67.0	4.04	4.69
5	24	493	0.0333	66.0	3.95	4.64
6	24	513	0.0331	64.6	3.90	4.62
7	25	473	0.0328	69.3	3.54	4.98
8	25	493	0.0333	68.9	3.52	4.86
9	25	513	0.0339	67.9	3.35	4.85

The experiments were run by fixing the inlet total mass flow rate and the heating power was changed until flow oscillations were observed. Therefore, the inlet mass flow rates in Table 3.1 are the instability threshold mass flow rates for the power indicated.

3.2 Xi et al. Experimental Loop (Xi et al. 2014)

Xi et al. (2014) continued the study of flow instability on the same experimental loop, but used a thicker wall and uniform and non-uniform axial power distributions. The test section was the same as Xiong et al. (2012) except for the water-cooled insulation flanges at the inlet and outlet of each pipe for better sealing and insulation, and the thicker wall of the heated section. A wall of 6.5 mm thickness was used for the test section. The length of the channels was 3.105 m and three copper plates were arranged along the axial direction of each pipe to divide it into two sections. The section close to the inlet was called the inlet section and the one close to the outlet was called the outlet section. For each section, two modular DC power supplies were connected in parallel to

supply the heat. The power of each group modular DC power supply was controlled independently to alter the axial power shape for the tests. A venturi flow meter was located at the entrance of each pipe to measure mass flow rate. The similar equivalent geometry (Figure 3.2) as of Xiong's experiment (Xiong et al. 2012) was suggested. The K factors for the experiments with a thicker wall were reported to be: $K_{in1} = 4.1$, $K_{in2} = 4.3$, $K_{out1} = 3.9$, $K_{out2} = 3.8$. The schematic diagram of the test section is similar to Fig. 3.1. Further details can be found in the cited reference.

3.2.1 Uniform Power Distribution

For uniform axial power distributions, and a system pressure of 23 MPa, tests were carried out for inlet temperatures ranging from 180 ^{o}C to 260 ^{o}C. The total inlet mass flow rate was held constant at 125 kg/ h. The experimental conditions and instability boundary are given in the Table 3.2. Flow instability occurred under five different inlet temperatures. With increasing inlet temperature, the system became more unstable.

Table 3.2 Experimental cases from Xi et al. (2014) with uniform axial power

Cases	System Pressure (MPa)	Inlet Temperature (K)	Inlet Mass Flow Rate (kg/s)	Threshold Power (kW)
1	23	458	0.0347	79.02
2	23	479	0.0347	77.22
3	23	495	0.0347	76.21
4	23	513	0.0347	72.91
5	23	533	0.0347	71.42

The cross-sectional temperature variation at inlet and outlet was negligible, hence average velocity was considered for the mass-flow rate prediction. The period of oscillation reported was 1.2 s while the inlet temperature was 260°C.

3.2.2 Influence of Axial Power Shape

The influence of axial power shape on flow instability was also studied experimentally. Three kinds of axial power shapes were used, which were axially decreased, uniform and axially increased. They found that the axial power shape had a significant impact on the instability boundaries and the dynamic characteristics. The influence of inlet temperature, axial power shape, total inlet mass flow rate and system pressure on the onset of flow instability were systematically studied experimentally. In the axially decreasing power shape cases, the heating power at the inlet section of each channel was constant at 20.75 kW. Only the heating power of the outlet section increased with time. On the other hand, in the cases with axially increased power shape, only the heating power of the inlet section increased with time. The heating power of the outlet section was held constant at 20.75 kW. The investigators mentioned that the axially increasing power profile didn't give any instability for the maximum permissible power limit, but for the axially decreased profile, instabilities were found. The instability boundaries for the axially decreased profile are given in Figure 3.3(a).

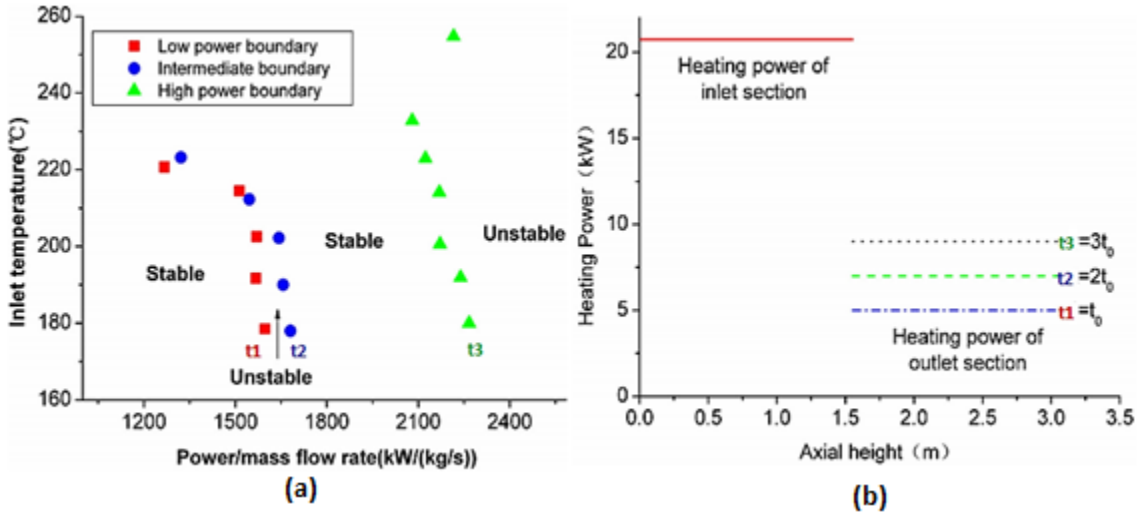

Figure 3.3 Xi et al. cases with axial decreasing power profile at 23 MPa (a) Summary of cases (b) Power profile (Xi et al. 2014)

The axially decreased profile is again categorized into three types based on the profile. As explained in the Figure 3.3(b), the Lower power boundaries consisted of 20.75KW in the first section and 5 KW in the second section. Intermediate boundary cases had 20.75 KW in the first section and 7.5 KW in the second section. High power boundaries had 20.75 KW in the first section and 10 KW in the second section.

When out of phase oscillation occurred near the LPB, the period was 1.6 s, slightly longer than when it occurred near the HPB, which was 1.3 s. Inlet mass flow rate oscillation and the outlet temperature oscillation were observed. The periods of the two were the same, as expected. The influences of these parameters on LPB, IB and HPB were different. However, the period and maximum inlet mass flow rate amplitude were not sensitive to them.

Chapter 4

Analytical Model of wall energy storage (Linear code)

Chatoorgoon and Upadhye (2005) developed a linear stability frequency-domain code based on perturbation theory and presented it at the NURETH-11 conference. The frequency domain code was developed for stability analysis of a natural circulation loop and single channels to validate the non-linear SPORTS time domain results. The linear code was extended by this author to analyse parallel channels with and without wall energy storage effects. This extended linear solution was presented in ICONE -26, London UK (Ghadge and Chatoorgoon, 2018). The equations explained by Chatoorgoon and Upadhye are given below, along with the modifications for wall thermal energy storage effects.

4.1 Non-Linear Governing Equations

The governing equations are area-averaged balances of mass, momentum and energy:

$$\frac{\partial \rho}{\partial t} + \frac{\partial (\rho u)}{\partial x} = 0 \tag{4.1}$$

$$\rho \frac{\partial u}{\partial t} + G \frac{\partial u}{\partial x} + \frac{\partial P}{\partial x} + C_k \rho u^2 + \rho g = 0 \tag{4.2}$$

$$\rho \frac{\partial h}{\partial t} + G \frac{\partial h}{\partial x} = q_w \tag{4.3}$$

In deriving Eq. (4.3), where x is the axial coordinate in a channel, the term $\frac{\partial P}{\partial t}$ has been assumed to be negligible for the applications considered here. The volumetric energy source due to exchange between the wall and the fluid is denoted q_w. The additional relation used is an equation of state $\rho = f(P, h)$.

4.1.1 Linearized Governing Equations

The governing equations above can be linearized and written in terms of perturbations to yield:

$$\frac{\partial \rho'}{\partial t} + \frac{\partial G'}{\partial x} = 0 \tag{4.4}$$

$$\rho_o \frac{\partial u'}{\partial t} + G_o \frac{\partial u'}{\partial x} + G' \left(\frac{du_o}{dx}\right) + \frac{\partial P'}{\partial x} + C_k(G_o u' + u_o G') + \rho' g = 0 \tag{4.5}$$

$$\rho_o \frac{\partial h'}{\partial t} + G_o \frac{\partial h'}{\partial x} + G' \left(\frac{dh_o}{dx}\right) = q'_w \tag{4.6}$$

4.1.2 Laplace Transform of the Linearized Equations

Taking the Laplace transform of the linearized equations and the equation of state yields:

$$s\,\widetilde{\rho'} + \frac{\partial \widetilde{G'}}{\partial x} = 0 \tag{4.7}$$

$$\widetilde{G'} = \rho_o \widetilde{u'} + u_o \widetilde{\rho'} \tag{4.8}$$

$$\rho_o\, s\, \widetilde{u'} + G_o \frac{\partial \widetilde{u'}}{\partial x} + \widetilde{G'} \frac{\partial u_o}{\partial x} + \frac{\partial \widetilde{P'}}{\partial x} + C_k\left(G_o \widetilde{u'} + u_o \widetilde{G'}\right) + \widetilde{\rho'} = 0 \tag{4.9}$$

$$\rho_o\, s\, \widetilde{h'} + G_o \frac{\partial \widetilde{h'}}{\partial x} + \widetilde{G'} \left(\frac{dh_o}{dx}\right) = \widetilde{q'_w} \tag{4.10}$$

$$\widetilde{\rho'} = \left(\frac{\partial \rho}{\partial h}\right)\widetilde{h'} \tag{4.11}$$

where $s = i\omega$.

4.1.3 Wall Heat Flow

Electrical energy creates a volumetric source term in the wall. Some of this energy is stored in the wall and the remainder is transferred to the fluid. The energy balance in the wall and the resulting equation are used to determine the heat transfer to the fluid.

4.1.3.1 Wall Temperature Equation

A lumped analysis is used to determine the wall temperature at a given axial location. The governing equation for the wall temperature is

$$\rho_w \, C_{p,w} \, V_w \, \frac{\partial T_w}{\partial t} \; = \; Q_e \; - \; Q_w \tag{4.12}$$

where Q_e is the rate of energy added to the wall from the electrical source and Q_w is the rate of energy transferred to the fluid. Subscript w refers to the wall properties. The heat transfer from the wall to the fluid can be written in terms a convective heat transfer coefficient, and the resulting T_w equation can be written as

$$\rho_w \, C_{p,w} \, V_w \, \frac{\partial T_w}{\partial t} \; = Q_e \; - \; A_w \;\; h_c \, (T_w - T) \tag{4.13}$$

Now using the relationship between the fluid temperature and enthalpy the following equation for the wall temperature is obtained:

$$\frac{\partial T_w}{\partial t} \; = \frac{Q_e}{\rho_w \, C_{p,w} \, V_w} \; - \; \frac{A_w \;\; h_c}{\rho_w \, C_{p,w} \, V_w} \left(T_w - \frac{h}{C_p} \right) \tag{4.14}$$

Writing Equation (4.14) in terms of perturbations yields,

$$\frac{\partial \mathrm{T}'_w}{\partial \mathrm{t}} \; = \; - \; \frac{A_w \;\; h_c}{\rho_w \, C_{p,w} \, V_w} \left(T'_w - \frac{h'}{C_p} \right) \tag{4.15}$$

Taking the Laplace transform of Equation (4.15) produces,

$$s \; \widetilde{T'_w} \; = \; - \; \frac{A_w \;\; h_c}{\rho_w \, C_{p,w} \, V_w} \left(\widetilde{T'_w} - \frac{\widetilde{h'}}{C_p} \right) \tag{4.16}$$

From Equation (4.16), the following equation for the Laplace transform of the wall temperature perturbation can be written,

$$\widetilde{T'_w} \; = \; \frac{\gamma}{(s + \gamma)} \, \frac{\widetilde{h'}}{C_p} \tag{4.17}$$

Where,

$$\gamma = \frac{A_w\ h_c}{\rho_w\ C_{p,w}\ V_w} = \frac{h_c}{\rho_w\ C_{p,w}\ D\ \left(\frac{t_w}{D}\right)\ \left(1 + \frac{t_w}{D}\right)} \tag{4.18}$$

4.1.4 Volumetric Energy Source Term

The volumetric energy source term in the fluid energy equation is defined as,

$$q_w = \frac{Q_w}{\left(\frac{\pi D^2}{4}\right)\Delta x} \tag{4.19}$$

where Δx is axial direction mesh spacing. The wall heat transfer can be estimated with a convective heat transfer coefficient as

$$Q_w = h_c(\pi D \Delta x)(T_w - T) \tag{4.20}$$

So that q_w can be written as:

$$q_w = \frac{4}{D} h_c (T_w - T) \tag{4.21}$$

Equation (4.21) can be written in terms of perturbations, considering only perturbations of the temperature. In addition, the fluid temperature can be related to its enthalpy. Taking the Laplace transform of the resulting equation yields,

$$\tilde{q}'_w = \frac{4}{D} h_c \left(\widetilde{T'_w} - \frac{\tilde{h}'}{C_p} \right) \tag{4.22}$$

Now, substituting for $\widetilde{T'_w}$ from Equation (4.17) yields,

$$\tilde{q}'_w = \frac{4}{D} h_c \left(\frac{\gamma}{(s+\gamma)} \frac{\tilde{h}'}{C_p} - \frac{\tilde{h}'}{C_p} \right) = -\frac{4}{D} \frac{h_c}{C_p} \left(\frac{1}{\left(1 + \frac{\gamma}{s}\right)} \right) \tilde{h}' \tag{4.23}$$

Finally, one can write

$$\tilde{q}'_w = -\frac{4}{D}\frac{h_c}{C_p}\left(\frac{1}{\left(1+\left(\frac{1}{s}\right)\frac{h_c}{\rho_w\, C_{p,w}\, D\, \left(\frac{t_w}{D}\right)\left(1+\frac{t_w}{D}\right)}\right)}\right)\tilde{h}' = -\lambda\,\tilde{h}' \qquad (4.24)$$

Equation (4.24) shows that the heat flux perturbation is zero when the wall thickness goes to zero or as the convective heat transfer coefficient goes to zero.

The convective heat transfer coefficient, h_c, is determined from a Dittus-Boelter type correlation of the form

$$\mathrm{Nu_b} = C_{DB}\mathrm{Re_b^{0.8}Pr_b^{0.4}} \qquad (4.25)$$

Where C_{DB} is 0.023 for subcritical fluids and 0.0243 for supercritical fluids.

4.1.5 Reduced Linear Equations

The linear equations can be simplified for a direct solution. The continuity, energy and state equations can be combined to eliminate $\widetilde{\rho'}$ and $\widetilde{h'}$. This yields,

$$\frac{\partial^2\widetilde{G'}}{\partial x^2}+\left[\frac{s}{u_o}+\frac{\lambda}{G_o}-\left(\frac{\partial\rho}{\partial h}\right)\frac{\partial}{\partial x}\left(\frac{1}{\left(\frac{\partial\rho}{\partial h}\right)}\right)\right]\frac{\partial\widetilde{G'}}{\partial x}-\left[\frac{s\left(\frac{\partial\rho}{\partial h}\right)}{G_o}\left(\frac{dh_o}{dx}\right)\right]\widetilde{G'}=0 \qquad (4.26)$$

Alternatively,

$$\frac{\partial^2\widetilde{\mathrm{G'}}}{\partial \mathrm{x}^2}+\left[\frac{\mathrm{s}}{\mathrm{u_o}}+\frac{\lambda}{\mathrm{G_o}}-\frac{\mathrm{d}(\ln\rho_\mathrm{h})}{\mathrm{dx}}\right]\frac{\partial\widetilde{\mathrm{G'}}}{\partial \mathrm{x}}-\frac{\mathrm{s}\rho_\mathrm{h}}{\mathrm{G_o}}\left(\frac{\mathrm{dh_o}}{\mathrm{dx}}\right)\widetilde{\mathrm{G'}}=0 \qquad (4.27)$$

Where,

$$\rho_\mathrm{h}=\frac{\partial\rho}{\partial \mathrm{h_p}} \qquad (4.28)$$

Another equation for $\widetilde{G'}$ can be obtained by combining the continuity and momentum equations to obtain:

$$\left[\frac{u_o^2}{s}\right]\frac{\partial^2\widetilde{G'}}{\partial x^2}+\left[2u_o+\frac{1}{s}\frac{\partial(u_o^2)}{\partial x}+C_k\frac{u_o^2}{s}-\frac{g}{s}\right]\frac{\partial\widetilde{G'}}{\partial x} + \left[s+2\frac{\partial u_o}{\partial x}+2C_k u_o\right]\widetilde{G'}+\frac{\partial\widetilde{P'}}{\partial x}=0 \quad (4.29)$$

Alternatively,

$$\nu_1\frac{\partial^2\widetilde{G'}}{\partial x^2}+\nu_2\frac{\partial\widetilde{G'}}{\partial x}+\nu_3\widetilde{G'}=-\frac{\partial\widetilde{\rho'}}{\partial x} \quad (4.30)$$

Where,

$$\nu_1=\frac{{u_o}^2}{s} \quad (4.31)$$

$$\nu_2=\frac{1}{s}\frac{d({u_o}^2)}{dx}+2u_o+C_k\left(\frac{{u_o}^2}{s}\right)-\frac{g}{s} \quad (4.32)$$

$$\nu_3=s+2\frac{du_o}{dx}+2C_k u_o \quad (4.33)$$

4.1.6 Non- heated channel

In the non-heated sections $\frac{dh_o}{dx}=0$, and Equation (4.27) simplifies to,

$$\frac{\partial^2\widetilde{G'}}{\partial x^2}+\left[\frac{s}{u_o}-\frac{d(\ln\rho_h)}{dx}\right]\frac{\partial\widetilde{G'}}{\partial x}=0 \quad (4.34)$$

The solution to Equation (4.34) can be obtained by first setting $\varsigma \equiv \frac{\partial\widetilde{G'}}{\partial x}$ and

$$\gamma_1=\left[\frac{s}{u_o}-\frac{d(\ln\rho_h)}{dx}\right] \quad (4.35)$$

Thus, Equation (4.34) reduces to

$$\frac{\partial\varsigma}{\partial x}+\gamma_1\varsigma=0 \quad (4.36)$$

This gives for each non-heated section,

$$\varsigma_{out}\equiv\left(\frac{\partial\widetilde{G'}}{\partial x}\right)_{out}=-s\widetilde{\rho'_{in}}e^{-\gamma_1 x_s} \quad (4.37)$$

$$\widetilde{G'_{out}} = \widetilde{G'_{in}} - (1 - e^{-\gamma_1 x_s})\frac{s\widetilde{\rho'_{in}}}{\gamma_1} \quad (4.38)$$

$$\widetilde{\rho'_{out}} = \widetilde{\rho'_{in}} e^{-\gamma_1 x_s} \quad (4.39)$$

$$\left(\frac{\partial^2 \widetilde{G'}}{\partial x^2}\right)_{out} = s\widetilde{\rho'_{in}} e^{-\gamma_1 x_s} \quad (4.40)$$

Where, $\widetilde{\rho'_{in}}$ and $\widetilde{G'_{in}}$ are Laplacian of perturbations at the section inlet and $\widetilde{\rho'_{out}}$ and $\widetilde{G'_{out}}$ are the Laplacian perturbations at the section outlet. Equations (4.37) - (4.40) can be used in Equation (4.30) to yield for $\widetilde{\rho'_{out}}$ each section.

4.1.7 Heated Sections

The general solution when heat added to any section can be expressed as,

$$\widetilde{G'} = A_1 e^{\omega_A x_s} + B_1 e^{\omega_B x_s} \quad (4.41)$$

where ω_A and ω_B are the roots of the quadratic equation,

$$m^2 + \gamma_1 m + \gamma_2 = 0 \quad (4.42)$$

where,

$$\gamma_1 = \frac{s}{u_o} - \frac{d(\ln \rho_h)}{dx} + \frac{\lambda}{G_o} \quad (4.43)$$

$$\gamma_2 = \frac{s\rho_h}{G_o}\left(\frac{dh_o}{dx}\right) \quad (4.44)$$

The roots of Equation (4.42) are

$$\omega_A, \omega_B = \frac{-\gamma_1 \pm \sqrt{\gamma_1^2 - 4\gamma_2}}{2} \quad (4.45)$$

Therefore, $\frac{\partial \widetilde{G'}}{\partial x}$ and $\frac{\partial^2 \widetilde{G'}}{\partial x^2}$ are

$$\frac{\partial \widetilde{G'}}{\partial x} = A_1 \omega_A e^{\omega_A x_s} + B_1 \omega_B e^{\omega_B x_s} \tag{4.46}$$

$$\frac{\partial^2 \widetilde{G'}}{\partial x^2} = A_1 {\omega_A}^2 e^{\omega_A x_s} + B_1 {\omega_B}^2 e^{\omega_B x_s} \tag{4.47}$$

A_1 and B_1 are found by matching the conditions at the end of the previous section.

$$\mathrm{A_1} = \frac{\left(\omega_\mathrm{B} \widetilde{\mathrm{G'_{in}}} + \mathrm{s}\widetilde{\rho'_{\mathrm{in}}}\right)}{(\omega_\mathrm{B} - \omega_\mathrm{A})} \tag{4.48}$$

$$\mathrm{B_1} = \frac{\left(\omega_\mathrm{A} \widetilde{\mathrm{G'_{in}}} + \mathrm{s}\widetilde{\rho'_{\mathrm{in}}}\right)}{(\omega_\mathrm{A} - \omega_\mathrm{B})} \tag{4.49}$$

Using Equations (4.26), (4.43), and (4.44) at the outlet yields

$$\widetilde{\mathrm{G'_{out}}} = \frac{1}{\gamma_2}\left(\mathrm{A_1}\omega_\mathrm{A} \mathrm{e}^{\omega_\mathrm{A} \mathrm{x_s}}(\omega_\mathrm{A} + \gamma_1) + \mathrm{B_1}\omega_\mathrm{B} \mathrm{e}^{\omega_\mathrm{B} \mathrm{x_s}}(\omega_\mathrm{A} + \gamma_1)\right) \tag{4.50}$$

Equation (4.26) can be combined with Equation (4.28) to eliminate $\widetilde{\boldsymbol{G'}}$. To yield

$$\left(\nu_1 - \frac{\nu_3}{\gamma_2}\right)\frac{\partial^2 \widetilde{\mathrm{G'}}}{\partial \mathrm{x}^2} + \left(\nu_2 - \nu_3 \frac{\gamma_1}{\gamma_2}\right)\frac{\partial \widetilde{\mathrm{G'}}}{\partial \mathrm{x}} = -\frac{\partial \widetilde{\mathrm{P'}}}{\partial \mathrm{x}} \tag{4.51}$$

Equation (4.51) can be integrated if the coefficients are constant. This yields,

$$\widetilde{P'_{\mathrm{out}}} = \widetilde{P'_{\mathrm{in}}} + s\left(\overline{\nu_1 - \frac{\nu_3}{\gamma_2}}\right)\left(\widetilde{\rho'_{\mathrm{out}}} - \widetilde{\rho'_{\mathrm{in}}}\right) + \left(\overline{\nu_3 \frac{\gamma_1}{\gamma_2} - \nu_2}\right)\left(\widetilde{G'_{\mathrm{out}}} - \widetilde{G'_{in}}\right) \tag{4.52}$$

where the overbar indicates the average steady-state value for that given section, $\widetilde{G'_{out}}$ is defined by Equation (4.26) and $\widetilde{\rho'_{\mathrm{out}}}$ is given by

$$\widetilde{\rho'_{\mathrm{out}}} = -\frac{1}{\mathrm{s}}\left(\frac{\partial \widetilde{\mathrm{G'}}}{\partial \mathrm{x}}\right)_{\mathrm{out}} = -\frac{1}{\mathrm{s}}\left(\mathrm{A_1}\omega_\mathrm{A} \mathrm{e}^{\omega_\mathrm{A} \mathrm{x_s}} + \mathrm{B_1}\omega_\mathrm{B} \mathrm{e}^{\omega_\mathrm{B} \mathrm{x_s}}\right) \tag{4.53}$$

If the geometry is discretized into sufficiently small sections where the steady-state coefficients are approximately constant in any given section, the above procedure will be adequate to yield the outlet pressure perturbation of every discretized section up to the last section.

4.2 Boundary Conditions

The analysis described in the previous section has a combination of non-linear time domain steady state solution and a linear Frequency domain solution. The 1D non-linear time domain solution is obtained using the SPORTS code.

4.2.1 Steady State Solution Boundary Conditions

Inlet: Mass flow rate and uniform temperature are specified at the inlet.

Outlet: Total pressure boundary condition is specified at the outlet.

Walls: Heating power is specified. Also, for cases with non-uniform axial power, a power ratio is specified.

4.2.2 Linear Solution Boundary Conditions

Channel Inlet: The Laplacian of the total pressure perturbation and density perturbation are given as zero. A small velocity perturbation is given at channel inlets.

Channel Outlet: The Laplacian of total pressure perturbation is specified as zero.

Walls: Heating power is specified.

4.3 Transfer Function

The stability boundary power for a single channel or natural circulation loop would be the power that satisfies $\widetilde{P'_{out}} = 0$, where $\widetilde{P'_{out}}$ is the calculated outlet total pressure perturbation at the last section.

In the case of parallel channels, the pressure at the outlet of 2 channels should be equal.

$$(P_{tot_{out}})_1 = (P_{tot_{out}})_2 \tag{4.54}$$

The outlet total pressure can also be written in the form of steady state pressure and perturbed pressure,

$$(P_{out1})_{ss} + P'_{out1} = (P_{out2})_{ss} + P'_{out2} \tag{4.55}$$

Where, $(P_{out1})_{ss} = (P_{out2})_{ss}$

Taking the Laplace transform,

$$\widetilde{P'_{tot_{out1}}} = \widetilde{P'_{tot_{out2}}} \tag{4.56}$$

So, it can also be stated as,

$$\widetilde{P'_{tot_{\text{out1}}}} - \widetilde{P'_{tot_{\text{out2}}}} = 0 \tag{4.57}$$

Hence for two parallel channels, the difference of $\widetilde{P'_{\text{out}}}$ of channel 1 and 2 was considered.

The transfer function of the system is given as follows:

$$G_c = \frac{(\widetilde{u'_{in}})\, G_o}{\left(\widetilde{P'_{tot_{out}}}\right)_1 - \left(\widetilde{P'_{tot_{out}}}\right)_2} = \frac{(\widetilde{u'_{in}})\, G_o}{\Delta\widetilde{P'_{tot_{out}}}} \tag{4.58}$$

At the instability threshold, the difference in pressure perturbation at the outlet must be equal to zero. So, the characteristic equation can be written as follows,

$$G_s = \frac{1}{G_c} = \frac{\Delta\widetilde{P'_{tot_{out}}}}{(\widetilde{u'_{in}})G_o} = 0 \tag{4.59}$$

The cross-over frequency is a frequency at which the phase margin is greater than 180° or less than -180°. The primary cross over frequency indicates the major period of oscillation. The other crossover frequencies give the hidden frequencies (secondary period of oscillations), which can be analysed with the help of fast Fourier transform (FFT) of the temporal response. Table 4.1 shows the stability criteria of Bode plot.

Table 4.1 Stability criteria of a Bode plot

Stability	Gain Margin G_s [$GM(G_s)$]	Phase Margin (Gs) [$PM(G_s)$]
Stable	$GM(G_s) < 0$	$-180° \leq PM(Gs) \leq 180°$
Stable	$GM(G_s) > 0$	$-180° \leq PM(Gs) \leq 180°$
Stable	$GM(G_s) < 0$	$-180° \geq PM(G_s)$ or $PM(G_s) \geq 180°$
Unstable	$GM(G_s) > 0$	$-180° \geq PM(G_s)$ or $PM(G_s) \geq 180°$

The gain margin for the Bode plot is usually calculated as,

$$GM(G_s) = 20\, log_{10}\, Gs \tag{4.60}$$

The phase margin can be given as,

$$PM(Gs) = tan^{-1} \frac{Im[Gs]}{Re[Gs]} \tag{4.61}$$

The Bode plot for the instability boundary of Case 3 is shown in Figure 4.1.

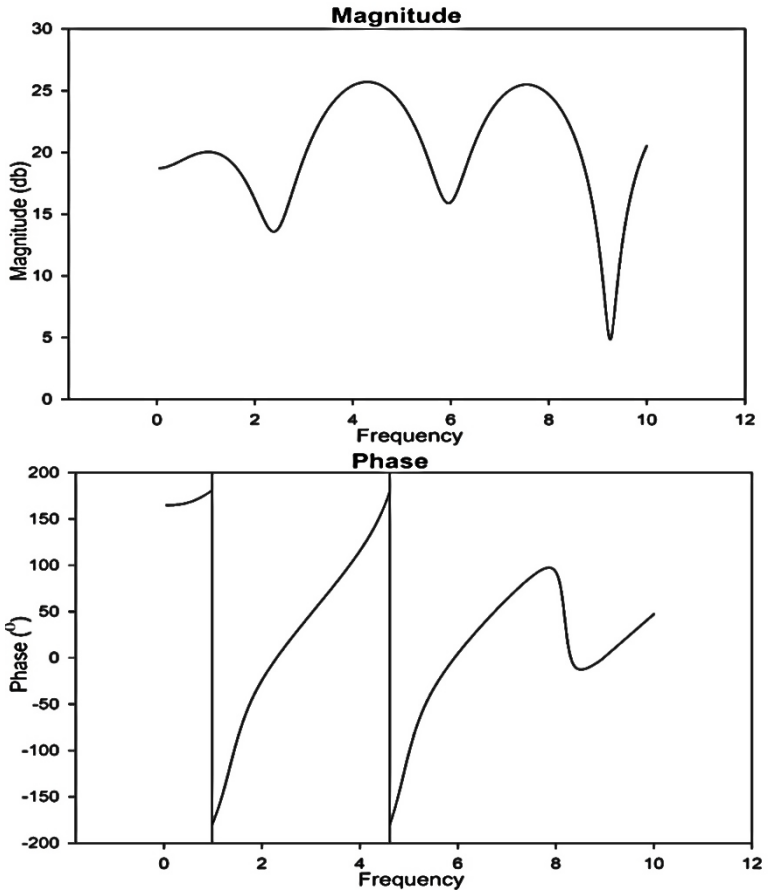

Figure 4.1 Bode plot (Case 3 instability boundary)

For frequency approximately 1 (1/s), the magnitude is above 0 dB and the phase shift for that frequency is also 180°. This shows the case is unstable and the major period of oscillation is 1 s.

4.4 Numerical Solution Method of the 1D Non-Linear Equations

The numerical method, a finite difference scheme is described in detail in Chatoorgoon (1986). The NIST property package (2003) has been used for the equation of state.

4.5 Solution Domain

Based on the simplified version of the experimental test section, the solution domain of the system is made. The height of plena is considered for non-linear SPORTS steady state solution while the linear frequency domain solution only uses the boundary condition of total pressure at outlet of the channel as explained in Section 4.4. Figure 4.2 shows the dimensions used in the analyses.

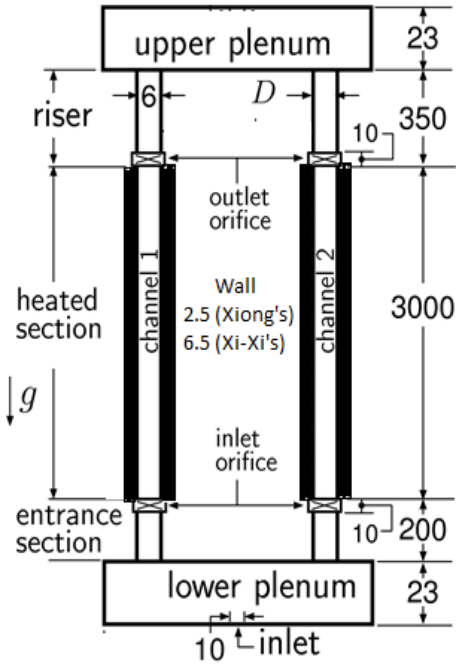

Figure 4.2 Schematic diagram of model used in Linear 1D analysis.

Dimensions are in mm.

Chapter 5

Non-dimensional parameters

Ambrosini and Sharabi (2008) derived non-dimensional parameters for supercritical fluids in heated systems. Unlike, the non-dimensional parameters proposed Zhao (2005), the new dimensionless parameters: trans-pseudo-critical number and sub-pseudo-critical number, adopted the pseudo-critical point as the only reference state. This was later proved to be a success (Ambrosini, 2011). These new non-dimensional parameters can be applied for supercritical stability analyses, but also to other supercritical fluids such as supercritical CO_2, R23 and Ammonia. While converting the experimental results for fluids, it was observed that the wall thickness of the heat structure should also be converted. To apply the non – dimensional parameters to the numerical results with wall thermal energy storage effects, the non-dimensional parameters were revised.

5.1 Dimensionless 1D equations for heated channels with supercritical fluids

The following conservation equations can be stated (Ambrosini and Sharabi 2008),

$$\frac{\partial \rho}{\partial t} + \frac{\partial (\rho w)}{\partial z} = 0 \tag{5.1}$$

$$\frac{\partial \rho w}{\partial t} + \frac{\partial \rho w^2}{\partial t} + \frac{\partial p}{\partial z} = -\rho g - \left[\frac{f}{D_h} + 2K_{in}\delta_d(z) + 2K_{ex}\delta_d(z-L)\right]\frac{\rho w^2}{2} \tag{5.2}$$

$$\frac{\partial \rho h}{\partial t} + \frac{\partial \rho h w}{\partial z} = q_o'' \frac{\pi_h}{A_c} f q(z) \tag{5.3}$$

The one-dimensional conduction equation can be written as,

$$\frac{\partial^2 T_w}{\partial r^2} + \frac{1}{r}\frac{\partial T_w}{\partial r} + \frac{\dot{g}}{k} = \frac{1}{\alpha}\frac{\partial T_w}{\partial t} \tag{5.4}$$

The following dimensionless parameters were adopted,

$$\rho^* = \frac{\rho}{\rho_{pc}} \tag{5.5}$$

$$h^* = \frac{\beta_{pc}}{C_{p_{pc}}}(h - h_{pc}) \tag{5.6}$$

$$P^* = \frac{P}{\rho_{pc} w_o^2} \tag{5.7}$$

$$N_{\text{TPC}} = q_o'' \frac{\pi_h L}{\rho_{pc} A_c w_o} \frac{\beta_{pc}}{C_{p_{pc}}} \tag{5.8}$$

$$N_{subpc} = \frac{\beta_{pc}}{C_{p_{pc}}}(h_{pc} - h_{in}) \tag{5.9}$$

$$t^* = \frac{t\omega_o}{L} \tag{5.10}$$

$$z^* = \frac{z}{L} \tag{5.11}$$

where all the pressure-dependent parameters are calculated at a unique operating pressure, disregarding local variations due to pressure drops.

Non-dimensional form of mass conservation, momentum conservation and energy conservation can be derived using Equations (5.1) - (5.3) and (5.5) - (5.11).

$$\frac{\partial \rho^*}{\partial t^*} + \frac{\partial (\rho^* w^*)}{\partial z^*} = 0 \tag{5.12}$$

$$\frac{\partial \rho^* w^*}{\partial t^*} + \frac{\partial \rho^* w^{*2}}{\partial t^*} + \frac{\partial p^*}{\partial z^*} = -\frac{\rho^*}{Fr} - [\Lambda + K_{in}\delta_d^*(z^*) + K_{ex}\delta_d^*(z^* - 1)]\frac{G^{*2}}{\rho^*} \tag{5.13}$$

$$\frac{\partial \rho^* h^*}{\partial t^*} + \frac{\partial \rho^* h^* w^*}{\partial z^*} = \frac{\pi_h q_o'' L}{\rho_{pc} A_c w_o} \frac{\beta_{pc}}{C_{p_{pc}}} f_q^*(z^*) \tag{5.14}$$

In Equation (5.14), the volumetric heat can be expressed as follows

$$q_o'' = \frac{Q}{\pi(R_1^2 - R_2^2)L} \tag{5.15}$$

The one-dimensional conduction equation then can be written as follows,

$$\frac{\partial^2 T_w}{\partial r^2} + \frac{1}{r}\frac{\partial T_w}{\partial r} + \frac{\dot{g}}{k} = \frac{1}{\alpha}\frac{\partial T_w}{\partial t} \tag{5.16}$$

$$\dot{g} = \frac{Q}{\pi(R_2^2 - R_1^2)L} - \frac{h_c(T_w - T_f)A_s}{\pi(R_1^2)L} \tag{5.17}$$

The temperature distribution across radial direction was assumed to be uniform (Lumped parameter), using Equations (5.15) and (5.16),

$$\frac{Q}{\pi(R_2^2 - R_1^2)L} - \frac{2h_c(T_w - T_f)\pi R_1 L}{\pi(R_1^2)L} = \frac{\mathrm{k}}{\alpha}\frac{\partial T_w}{\partial \mathrm{t}} \tag{5.18}$$

From Equation (5.18) and Equation (5.15),

$$\frac{Q}{\pi(R_2^2 - R_1^2)L} = \frac{\mathrm{k}}{\alpha}\frac{\partial T_w}{\partial \mathrm{t}} + \frac{2h_c(T_w - T_f)\pi R_1 L}{\pi(R_1^2)L} \tag{5.19}$$

$$Q = \left(\frac{\mathrm{k}}{\alpha}\frac{\partial T_w}{\partial \mathrm{t}} + \frac{2h_c(T_w - T_f)\pi R_1 L}{\pi(R_1^2)L}\right)\pi(R_2^2 - R_1^2)L \tag{5.20}$$

From Equation (5.14),

$$\frac{\partial \rho^* h^*}{\partial t^*} + \frac{\partial \rho^* h^* w^*}{\partial z^*} = \frac{(\pi_h q_o'' L)\rho_{in}}{(\rho_{in} A_c w_o)\rho_{pc}}\frac{\beta_{pc}}{C_{p_{pc}}} f_q^*(z^*) \tag{5.21}$$

$$\frac{\partial \rho^* h^*}{\partial t^*} + \frac{\partial \rho^* h^* w^*}{\partial z^*} = \frac{Q\rho_{in}}{\dot{m}\rho_{pc}}\frac{\beta_{pc}}{C_{p_{pc}}} f_q^*(z^*) \tag{5.22}$$

$$\frac{\partial \rho^* h^*}{\partial t^*} + \frac{\partial \rho^* h^* w^*}{\partial z^*} = \left(\frac{Q}{\dot{m}}\frac{\beta_{pc}}{C_{p_{pc}}}\right) f_q^*(z^*)\rho_{in}^* \tag{5.23}$$

$$\frac{\partial \rho^* h^*}{\partial t^*} + \frac{\partial \rho^* h^* w^*}{\partial z^*} = \left(\frac{Q}{\dot{m}}\frac{\beta_{pc}}{C_{p_{pc}}}\right)\left(\frac{Q}{Q}\right) f_q^*(z^*)\rho_{in}^* \tag{5.24}$$

From Equation (5.24) and Equation (5.8), the right hand side of Equation (5.24) can be written as,

$$= N_{\mathrm{TPC}}\left(\left(\frac{\mathrm{k}}{\alpha \mathrm{Q}}\frac{\partial T_w}{\partial \mathrm{t}} + \frac{2h_o(T_w - T_f)\pi R_1 L}{\pi(R_2^2 - R_1^2)LQ}\right)\pi(R_2^2 - R_1^2)L\right) f_q^*(z^*)\rho_{in}^* \tag{5.25}$$

$$= N_{\mathrm{TPC}}\left[\frac{\mathrm{k}}{\left(\frac{k}{\rho_w C_{p_w}}\right)}\frac{\partial T_w}{\partial \mathrm{t}}\frac{V_w}{Q}\right] f_q^*(z^*)\rho_{in}^* + N_{\mathrm{TPC}}\left[\frac{2h_c(T_w - T_f)\pi R_1 L V_w}{Q\pi(R_1^2)L}\right] f_q^*(z^*)\rho_{in}^* \tag{5.26}$$

Here, volume of wall can be expressed as,

$$V_w = 2\pi R_m t_w L \tag{5.27}$$

Where, $\mathrm{R_m} = \frac{\mathrm{R_1 + R_2}}{2}$ and t_w is wall thickness.

Using Equation (5.26) and (5.27)

$$= \left(N_{\mathrm{TPC}} \left[\frac{(\rho_w C_{p_w} V_w)}{\mathrm{Q}} \frac{\partial T_w}{\partial \mathrm{t}} \right] + N_{\mathrm{TPC}} \left[\frac{2h_c (T_w - T_f) \pi R_1 L (2\pi R_m t_w L)}{Q\pi (R_1^2) L} \right] \right) f_q^*(z^*) \rho_{in}^* \quad (5.28)$$

$$= N_{\mathrm{TPC}} \left[\frac{(m_w C_{p_w} \frac{\partial T_w}{\partial \mathrm{t}})}{\mathrm{Q}} \right] f_q^*(z^*) \rho_{in}^* + N_{\mathrm{TPC}} \left[\frac{4\pi h_c (T_w - T_f)(R_m t_w L)}{Q(R_1)} \right] f_q^*(z^*) \rho_{in}^* \quad (5.29)$$

Replacing $m_w C_{p_w} \frac{\partial T_w}{\partial \mathrm{t}}$ by change in internal energy

$$N_{\mathrm{TPC}} \left[\frac{\Delta U}{\mathrm{Q}} \right] f_q^*(z^*) \rho_{in}^* + N_{\mathrm{TPC}} \left[\frac{4\pi h_c (T_w - T_f)(R_m t_w L)}{Q(R_1)} \right] f_q^*(z^*) \rho_{in}^* \quad (5.30)$$

$$N_{\mathrm{TPC}} f_q^*(z^*) \rho_{in}^* + N_{\mathrm{TPC}} \left[\frac{4\pi h_c (T_w - T_f)(R_m t_w L)}{Q(R_1)} \right] f_q^*(z^*) \rho_{in}^* \quad (5.31)$$

The temperature of fluid can be written in following form,

$$T_f = \varepsilon_n h \quad (5.32)$$

Where ε_n (kg-K/kJ), h is enthalpy (kJ/kg)

$$h^* = \frac{\beta_{pc}}{C_{p_{pc}}} (h - h_{pc}) \quad (5.33)$$

Using Equations (5.31), (5.32) and (5.33)

$$N_{\mathrm{TPC}} f_q^*(z^*) \rho_{in}^* + N_{\mathrm{TPC}} \left[\frac{4\pi h_c (R_m t_w L)(T_w - \varepsilon_n h^*)}{Q(R_1)} \right] f_q^*(z^*) \rho_{in}^* \quad (5.34)$$

$$N_{\mathrm{TPC}} f_q^*(z^*) \rho_{in}^* + N_{\mathrm{TPC}} \left[\frac{4\pi h_c (R_m t_w L) \left(T_w - \varepsilon_n \left(h^* \frac{C_{p_{pc}}}{\beta_{pc}} + h_{pc} \right) \right)}{Q(R_1)} \right] f_q^*(z^*) \rho_{in}^* \quad (5.35)$$

From Equation (5.35),

Term I = $N_{\mathrm{TPC}} f_q^*(z^*) \rho_{in}^*$

Term II $= N_{\mathrm{TPC}} \left[\frac{4\pi h_c (R_m t_w L)\left(T_w - \varepsilon_n\left(h^* \frac{C_{p_{pc}}}{\beta_{pc}} + h_{pc}\right)\right)}{Q(R_1)} \right] f_q^*(z^*)\rho_{in}^*$

The term II can be resolved further as,

$$N_{\mathrm{TPC}} \left[\frac{4\pi h_c (R_m t_w L)\left(T_w - \varepsilon_n\left(h_{pc}\right)\right)}{Q(R_1)} - \frac{4\pi h_c (R_m t_w L)\left(T_w - \varepsilon_n\left(h_{pc}\right)\right)}{Q(R_1)} \left(\frac{T_w - \varepsilon_n\left(h^* \frac{C_{p_{pc}}}{\beta_{pc}}\right)}{\left(T_w - \varepsilon_n\left(h_{pc}\right)\right)} \right) \right] f_q^*(z^*)\rho_{in}^* \tag{5.36}$$

Hence N_{wall} can be stated as,

$$N_{wall} = \frac{4\pi h_c (R_m t_w L)\left(T_w - \varepsilon_n\left(h_{pc}\right)\right)}{Q(R_1)} \tag{5.37}$$

The Equation (5.36), can be written as,

$$N_{\mathrm{TPC}} N_{\mathrm{wall}} \left(1 - \left(\frac{T_w - \varepsilon_n\left(h^* \frac{C_{p_{pc}}}{\beta_{pc}}\right)}{\left(T_w - \varepsilon_n\left(h_{pc}\right)\right)} \right)\right) f_q^*(z^*)\rho_{in}^* \tag{5.38}$$

$$N_{\mathrm{TPC}} N_{\mathrm{wall}} (1 - \Delta T^*) f_q^*(z^*)\rho_{in}^* \tag{5.39}$$

Where,

$$\Delta T^* = \frac{T_w - \varepsilon_n\left(h^* \frac{C_{p_{pc}}}{\beta_{pc}}\right)}{\left(T_w - \varepsilon_n\left(h_{pc}\right)\right)} \tag{5.40}$$

The Equation (5.24) can be written as,

$$\frac{\partial \rho^* h^*}{\partial t^*} + \frac{\partial \rho^* h^* w^*}{\partial z^*} = \left(N_{\mathrm{TPC}} + N_{\mathrm{TPC}} N_{\mathrm{wall}} (1 - \Delta T^*)\right) f_q^*(z^*)\rho_{in}^* \tag{5.41}$$

So, from above equation we can say that the equation gives a proper trend,

If thickness of wall is zero, N_{wall} equals to zero and Equation (5.41) can be written as,

$$\frac{\partial \rho^* h^*}{\partial t^*} + \frac{\partial \rho^* h^* w^*}{\partial z^*} = (N_{\mathrm{TPC}}) f_q^*(z^*) \rho_{in}^* \tag{5.42}$$

The results of N_{wall} were tested using two fluids water and CO_2 in supercritical region. The results using N_{wall} are discussed in Chapter 7.

Chapter 6

Numerical Modelling

6.1 Geometrical Model

The original experimental setup made up of several throttle valves, tube bends and diameter-varied pipes from the lower plenum to the entrance of heated section (called the entrance section) and from the exit of the heated section to the upper plenum (called the riser section). A simplified version of the experimental test section was proposed by Xiong et al. (2012). This simplified model modifies the entrance and riser sections by making the pipes with different inner diameters in these sections have uniform inner diameter, which is equal to the inner diameter of the pipe in the heated section. Local pressure drops are assumed to get concentrated in the orifices at inlet and outlet across each channel. The equivalent geometry has been explained before in Section 3.1.1. The geometrical model was developed in ANSYS geometry modelling software called Spaceclaim.

The geometry has been divided into key parts such as the lower plenum, the upper plenum, the channels, the risers and the orifices. The “Topology sharing” option is used to obtain matching grids at interfaces between parts in Ansys Meshing. The isometric view of the geometry is shown in Figure 6.1. Each part was divided in several sections to obtain hexagonal mesh and O-grid across the channel and wall. It can be seen in detail as follows.

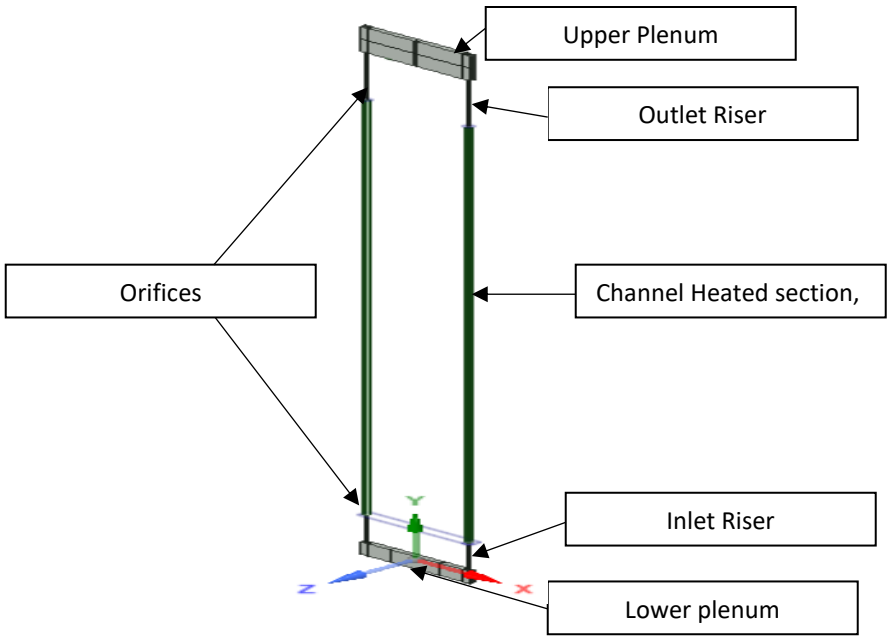

Figure 6.1 Parallel channels schematic

Plena

The lower and upper plena height for the previous study by Li (2016) was considered as 23 mm. It was observed that for the full geometry with 23 mm high plena, the highest residuals of the solution domain were located in the plena. When the flow solution in the lower plenum was examined in terms of residuals, it was observed that the small recirculation zones were occurring in the plenum, making it difficult to obtain a converged solution. The height of the lower plenum was then increased to 90 mm to reduce these effects. In addition, the inlet of the lower plenum was increased to 180 mm X 20 mm from 20 mm X 20 mm to assist in reducing flow circulation pockets in the plenum. In the upper plenum, the flow from outlet of each channel was emerging with a high velocity in the range of 6 m/s to 8 m/s, forming a jet-like structure. These fluid jets were hitting the upper plenum wall, creating a complex dynamic in the plenum. The height of the upper plenum was increased to 180 mm to reduce this effect.

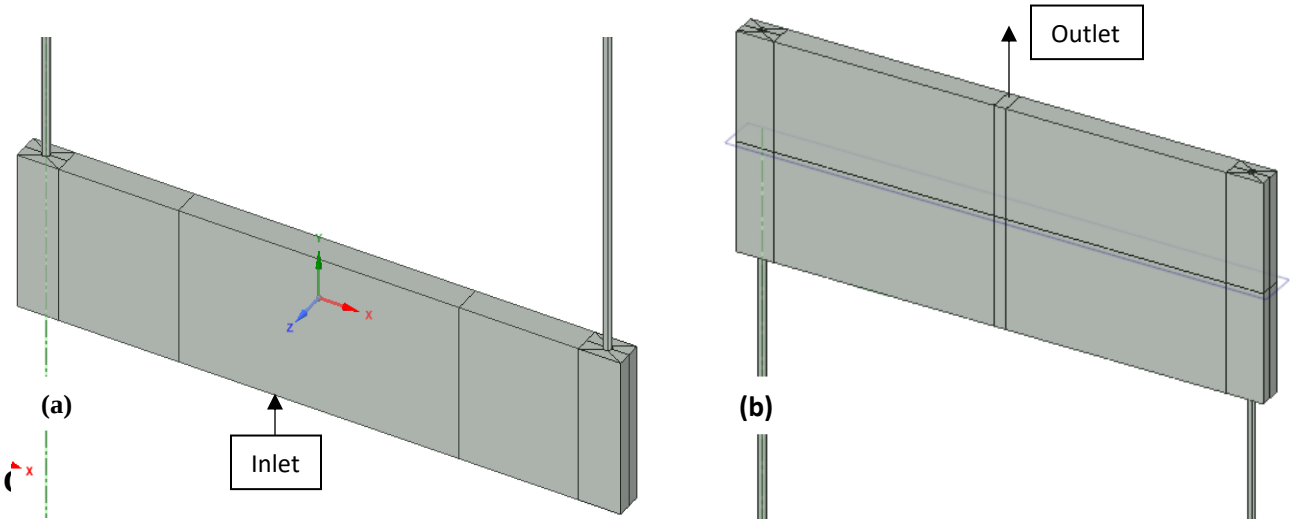

Figure 6.2 (a) Lower Plenum (b) Upper plenum

The channels, orifices and riser were modelled in eight parts to facilitate creating the blocks needed for O-grid style mesh.

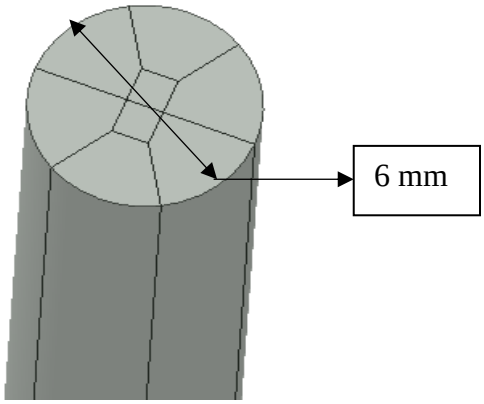

Figure 6.3 Channel, orifices and riser

Wall

The wall region was divided into six segments that followed logically from the O-grid used in the fluid region. A sample view of the wall is shown in Figure 6.4. The wall thickness was varied to match the experiments: 2.5 mm (Xiong et al. 2012) and 6.5 mm (Xi et al. 2014).

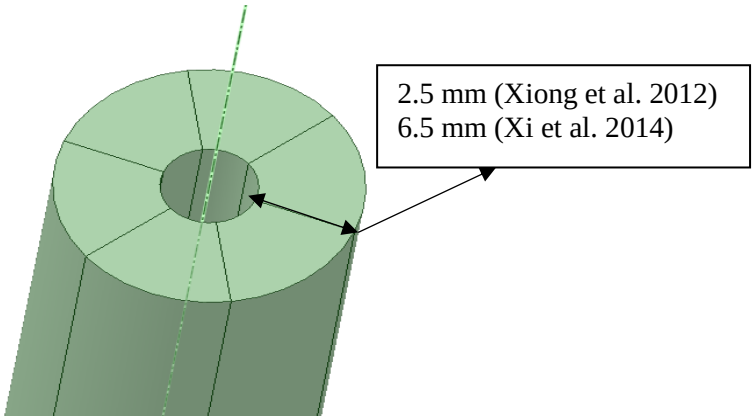

Figure 6.4 Wall

The equivalent geometry used for the CFX study is shown in Figure 6.5.

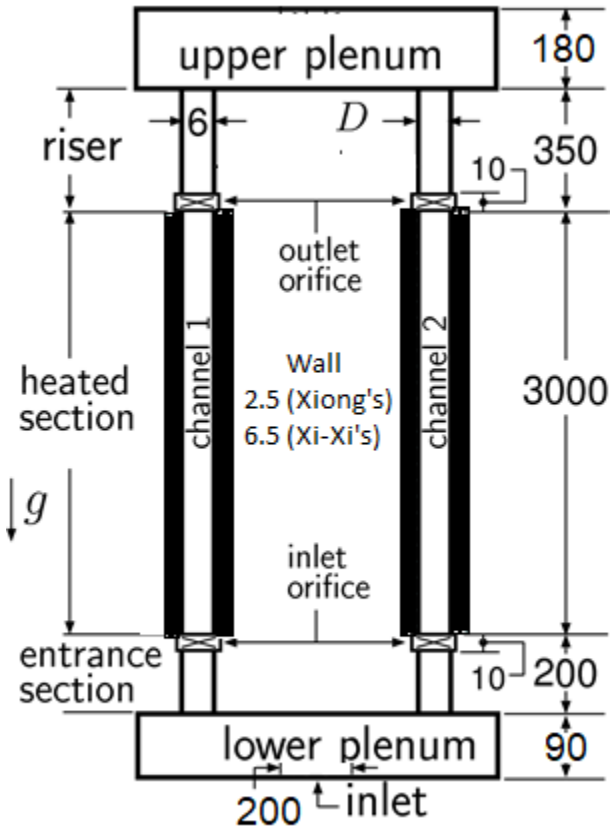

Figure 6.5 Equivalent geometry used in ANSYS CFX 18.2

6.2 Assumptions

The following assumptions are made with regards to the governing equations. The assumptions are similar to Li (2016) except for the wall heat structure and symmetry.

- The flow is not symmetric. (The reasons are explained in Chapter 7.)
- The flow is turbulent based on the calculated Reynolds number. (20,000-40,000 at inlet)
- The water is a Newtonian fluid.
- Radiation heat transfer is negligible because of the relatively low temperature difference expected between the channel and plenum walls.
- Heat transfer loss to the surrounding is negligible as the wall is assumed to be well insulated.
- Reynolds stresses can be approximated by the eddy-viscosity assumption.

6.3 Governing Equations

The governing equations consist of transport equations for conservation of mass, momentum, energy and turbulence quantities.

The governing equations in Cartesian coordinates are:

Continuity Equation:

$$\frac{\partial(\rho)}{\partial t} + \frac{\partial\left(\rho U_j\right)}{\partial x_j} = 0 \qquad (6.1)$$

Momentum Conservation Equation:

$$\left(\frac{\partial(\rho U_i)}{\partial t}\right) + \left(\frac{\partial\left(\rho U_j U_i\right)}{\partial x_j}\right)$$

$$= -\frac{\partial P'}{\partial x_i} + \frac{\partial}{\partial x_j}\left((\mu + \mu_t)\left[\frac{\partial U_i}{\partial x_j} + \frac{\partial U_j}{\partial x_i}\right]\right) + S_{M,buoy} + S_{M,frict} \quad (6.2)$$

where P' is the modified pressure and μ_t is the eddy viscosit.

$S_{M,buoy}$ is a source term added to the momentum equations as follows for buoyancy calculation:

$$S_{M,buoy} = \left(\rho - \rho_{ref}\right) g_i \quad (6.3)$$

where reference density, ρ_{ref}, is defined as the average density over the entire fluid domain. In this study, a value of 500 kg/m^3 for ρ_{ref} was used. For the y axis, aligned with the upward flow direction, the acceleration due to gravity, g_y, is -9.81 m/s^2. In the other two directions, both g_x and g_z are 0 m/s^2.

The full buoyancy model implemented in CFX was used in this study because of the spatial variation of the water density due to pressure and temperature change. When buoyancy is enabled in CFX, the pressure in the momentum equation excludes the hydrostatic gradient due to ρ_{ref}. Then, the pressure term appears in the momentum equation becomes the modified pressure, P', which is defined by using the static pressure P and turbulence kinetic energy k:

$$P' = P + \frac{2}{3}\rho k \quad (6.4)$$

This modified pressure is also related to the absolute pressure as follows:

$$P_{abs} = P' + P_{ref} + \rho_{ref} g\ (\vec{r} - \overrightarrow{r_{ref}}) \quad (6.5)$$

where P_{ref} is the reference pressure over the entire fluid domain and $\rho_{ref} g\left(\vec{r} - \overrightarrow{r_{ref}}\right)$ represents the hydrostatic pressure. All relative pressures in CFX are relative to this pressure. $\overrightarrow{r_{ref}}$ is the buoyancy reference location, specified at the centroid of one of the pressure-specified boundaries.

$S_{M,frict}$ is a general momentum source used to model the local friction pressure drop caused by a K-factor. There are two options to apply momentum sources in CFX: Loss model and General Momentum Source. Based on a previous study Ebrahimnia (2014), the general momentum source is preferred and enabled in this study to agree with the K factor modeling used in 1-D codes.

The general momentum source is able to specify the momentum sources in a specified direction, directly in terms of a momentum source per unit volume and is applied on fluid subdomains in the orifices. By neglecting the effect of velocity variation, shear stress and gravity in the subdomain, the momentum equation for steady-state condition becomes:

$$-\frac{\partial P}{\partial x_i} + S_{M,frict,i} = 0 \tag{6.6}$$

Therefore, desired pressure gradient can be obtained by specifying the general momentum source in a specific direction. In the flow direction the (y direction), the general momentum source is specified by:

$$S_{M,frict,y} = -\frac{K}{\Delta y} \times \frac{G}{2} \times V \tag{6.7}$$

where *K* is the local pressure drop coefficient, Δy is the length of the subdomain, and *G* is the mass flux which is equal to:

$$G = \frac{\dot{m}}{A} \tag{6.8}$$

where $\dot{m}$ is the mass flow rate and A is the cross section area. In Equation (6.7), V is the area-averaged value of the y-direction velocity.

When the source term is a function of velocity, to obtain good convergence the Momentum Source Coefficient (k) is specified in CFX for linearizing the source term with the following relation:

$$-\frac{\partial P}{\partial x_i} = \mathrm{k}U_i \tag{6.9}$$

Combining Equation (6.9) with Equations (6.6) and (6.7), k can be calculated with the following equation:

$$\mathrm{k} = \frac{K}{\Delta y} \times \frac{G}{2} \tag{6.10}$$

Because, the general momentum source approach is used to create a in pressure drop, the "Redistribute in Rhie Chow" and "Include Coefficient in Rhie Chow" options in CFX should be enabled to avoid possible pressure oscillations near the subdomain boundary.

Energy Conservation Equation:

Compared to the thermal energy equation, the total energy equation is preferred in this study. For a compressible flow, the total energy equation can achieve a more accurate solution by including the mechanical energy.

The total energy conservation equation is as follows:

$$\left(\frac{\partial(\rho h_{tot})}{\partial t}\right) + \left(\frac{\partial(\rho U_j h_{tot})}{\partial x_j}\right) = \frac{\partial}{\partial x_j}\left((\lambda + \frac{\mu_t}{Pr_t})\frac{\partial h}{\partial x_j} + \frac{\partial}{\partial x_j}(U_j[\tau_{ij} - \rho\overline{u_i u_j}]) + U_j \cdot S_M\right) \tag{6.11}$$

where h_{tot} is the total enthalpy and is related to the static enthalpy, mechanical energy, and turbulence kinetic energy as follows:

$$h_{tot} = h + \frac{1}{2}U_i U_i + k \tag{6.12}$$

where *h* is the static enthalpy. The turbulence kinetic energy, k, is modeled by:

$$k = \frac{1}{2}\,\overline{u_i u_i} \tag{6.13}$$

where u_i is the velocity fluctuation.

In Equation (6.11), $\frac{\partial}{\partial x_j}(U_j[\tau_{ij} - \rho\overline{u_i u_i}])$ represents the work due to viscous stresses and is named as the viscous work term. It models the internal heating by viscosity in the fluid, and is negligible in most flows. However, because of compressibility of this flow, it is included in the total energy equation in this study. The term $U_j \cdot S_M$ represents the work due to external momentum sources and is currently neglected. In the present study, both steady-state and transient solutions of the governing equations were performed.

6.4 Turbulence Closure

In general, turbulent flow could be said to exhibit average characteristics, with an additional time-varying, fluctuating component. Therefore, the original unsteady Navier-Stokes equations can be modified by the use of averaged and fluctuating quantities to produce the Reynolds Averaged Navier-Stokes (RANS) equations. Because Large Eddy Simulation (LES) and Direct Numerical Simulation (DNS) are too computationally expensive to model this problem, a RANS-based model is selected in this work.

However, the Reynolds averaging for RANS model introduces additional unknown terms including products of the fluctuating quantities, which are known as ‘turbulent’ or ‘Reynolds’ stresses. Reynolds stresses are difficult to determine directly and need to be modeled by additional equations with known quantities. For an isothermal flow, there are only four equations (the momentum equations in three directions and the continuity equation) to solve ten unknown quantities (the velocity components in three directions, the pressure, and six Reynolds stresses) in

isothermal turbulent flow problems. Hence, turbulence modeling for six unknown Reynolds stresses is required to close the equation system.

In this study, however, a full Reynolds stress model was not adopted. Instead, the eddy viscosity concept was invoked and a two-equation turbulence model was used.

6.4.1 Standard k-ε Turbulence Model

The standard *k-ε* turbulence model by Launder and Sharma (1974) is one of the most commonly used turbulence models, and it includes two extra transport equations to represent the turbulence quantities of the flow. These two additional equations are the turbulence kinetic energy, *k*, and the turbulent dissipation rate, *ε*.

The standard *k-ε* model with a scalable wall-function was used to calculate μ_t with the following relation:

$$\mu_t = C_\mu \rho \frac{k^2}{\varepsilon} \tag{6.14}$$

where C_μ is a closure constant and equal to 0.09. The turbulence kinetic energy, *k*, and the turbulence dissipation rate, *ε*, are obtained by solving the following two transport equations:

$$\frac{\partial(\rho k)}{\partial t} + \frac{\partial(\rho U_j k)}{\partial x_j} = \frac{\partial}{\partial x_j}\left(\left(\mu + \frac{\mu_t}{\sigma_k}\right)\frac{\partial k}{\partial x_j}\right) + P_k - \rho\varepsilon + P_{kb} \tag{6.15}$$

$$\frac{\partial(\rho \varepsilon)}{\partial t} + \frac{\partial(\rho U_j \varepsilon)}{\partial x_j} = \frac{\partial}{\partial x_j}\left(\left(\mu + \frac{\mu_t}{\sigma_\varepsilon}\right)\frac{\partial \varepsilon}{\partial x_j}\right) + \frac{\varepsilon}{k}\left(C_{\varepsilon 1} P_k - C_{\varepsilon 2}\rho\varepsilon + C_{\varepsilon 1} P_{\varepsilon b}\right) \tag{6.16}$$

where closure constants σ_k = 1.0, σ_ε = 1.3, $C_{\varepsilon 1}$ = 1.44 and $C_{\varepsilon 2}$ = 1.92. The turbulence production term, P_k, is modeled using:

$$P_k = \mu_t \left(\frac{\partial U_i}{\partial x_j} + \frac{\partial U_j}{\partial x_j} \right) \frac{\partial U_i}{\partial x_j} - \frac{2}{3} \frac{\partial U_k}{\partial x_k} \left(3\mu_t \frac{\partial U_k}{\partial x_k} + \rho k \right) \quad (6.17)$$

$\frac{\partial U_k}{\partial x_k}$ is large only in regions where velocity divergence is high for compressible flow, such as shocks. Therefore, the second term on the right-hand side of Equation (6.17) does not contribute significantly to the production for current flow conditions.

P_{kb} and $P_{\varepsilon b}$ in Equations (6.15) and (6.16) are turbulence production and dissipation due to buoyancy forces, respectively. They are included in the k and ε equation when the Buoyancy Turbulence option in CFX is set to 'Production and Dissipation' (ANSYS CFX-Solver Theory Guide 2013).

When the Full Buoyancy model is being used, the buoyancy production term, P_{kb}, is modeled as:

$$P_{kb} = -\frac{\mu_t}{\rho \sigma_\rho} g_i \frac{\partial \rho}{\partial x_i} \quad (6.18)$$

where σ_ρ is the turbulent Schmidt number and is equal to 1 for the Full Buoyancy model.

The buoyancy dissipation term, $P_{\varepsilon b}$, is assumed to be proportional to P_{kb} and must be positive, which is modeled as:

$$P_{\varepsilon b} = C_3 . max(0, P_{kb}) \quad (6.19)$$

where C_3, the Dissipation Coefficient, is equal to 1.

6.4.2 Scalable Wall Functions

The near-wall region can be subdivided into viscous sub-layer and logarithmic layer. For the viscous sublayer, the molecular viscosity is dominant in momentum and heat or mass transfer, whereas turbulence plays a major role in logarithmic layer. Wall functions, a set of semi-empirical

formulas and functions presumed to lie in log-layer, can be employed to link near-wall conditions in the viscosity affected sublayer region to the dependent variables at the near-wall cells.

The logarithmic relation for the near-wall velocity is given by:

$$u^+ = \frac{U_t}{u_\tau} = \frac{1}{\kappa} ln(y^+) + C \tag{6.20}$$

where u^+ is the near-wall velocity, u_τ is the friction velocity, U_t is the known velocity tangent to the wall at a distance of Δy from the wall, κ is the von-Karman constant typically 0.41, and C is a log-layer constant depending on the wall roughness (C = 5.2 for a smooth wall). y^+, the dimensionless distance from the wall, and friction velocity, u_τ, are defined as:

$$y^+ = \frac{\rho \Delta y u_\tau}{\mu} \tag{6.21}$$

$$u_\tau = \left(\frac{\tau_\omega}{\rho}\right)^{\frac{1}{2}} \tag{6.22}$$

where τ_ω is the wall shear stress.

To solve the singular problem of Equation (6.20) when U_t goes to zero, an alternative velocity scale, u^*, is used instead of u_τ in the logarithmic region:

$$u^* = C_\mu^{1/4} \, k^{1/2} \tag{6.23}$$

Then u_τ can be obtained using:

$$u_\tau = \frac{U_t}{\frac{1}{k} ln(y^*) + C} \tag{6.24}$$

The absolute value of wall shear stress τ_ω is obtained from:

$$\tau_\omega = \rho \, u^* u_\tau \tag{6.25}$$

where

$$y^* = (\rho u^* \Delta y)/\mu \quad (6.26)$$

However, this-wall function approach has the drawback that refining the mesh does not necessarily result in a unique solution of increasing accuracy. The use of scalable wall function formulation in ANSYS CFX for ε-equation based turbulence models can overcome this problem. It can be applied on arbitrarily fine meshes and produces consistent results for grids of varying y^+, independent of the Reynolds number of the application.

Scalable wall functions are implemented with the standard k-ε turbulence model in CFX. The basic idea behind the scalable wall function approach is to limit the value of y* used in the logarithmic formulation by a value of y* = max (y*, 11.06), where 11.06 is the value of y* at the intersection between the logarithmic and the linear wall profile. This method avoids the use of log-layer equations in a region where they were not appropriate. The non-dimensional distance from the wall, y^+, must be within a certain range for a specific turbulence model with proper wall function. When using the *k-ε* turbulence model with a scalable wall function, y+ should be less than 300.

6.4.3 Wall Heat Model

The only difference in the governing equations between previous work of Li (2016) and the present study is that the present study has conjugate heat transfer. CFX enables creating solid region in which heat transfer equations are solved. Within the solid domain, it can account for conduction, volumetric heat source and solid movement ("ANSYS CFX Solver Theory Guide" 2009). The energy conservation within the solid region is,

$$\frac{\partial(\rho h)}{\partial t} + \nabla(\rho U_s h) = \nabla(\lambda \Delta T) + S_E \quad (6.27)$$

Where, ρ, h, λ are the density, enthalpy and thermal conductivity respectively. U_s is the solid velocity, which is zero in the present case and S_E is the volumetric heat source which is specified in the wall. At the solid fluid interface, the CFX Solver calculates both fluid-side and solid-side temperatures based on heat flux conservation. These values are representative of the temperature within the half-control volumes around the vertices on the interface.

6.5 Boundary Conditions

Boundary conditions at the inlet, outlet, wall, symmetry and domain interface as well as the initial conditions of fluid domains and subdomains were prescribed as discussed in this section. The inlet turbulence intensity and the turbulent Prandtl number values were based on the sensitivity study by Li (2016).

Inlet:

- Specified mass flow rate
- Specified inlet temperature
- Turbulence: Medium Intensity (*I*=5%); Viscosity ratio (10)
- Flow direction: normal to boundary

Outlet:

- Relative Static Pressure: 0 [Pa]

Wall:

- Volumetric heat source is supplied.
- Fluid side: Conjugate heat transfer, No slip, Smooth
- Outer sides: Adiabatic

Interfaces:

- Conservation of mass, momentum, turbulence, and energy between two domains.

Fluid Domains:

- Material: Water
- Reference Pressure: Specified in the range of 23-25 MPa, depending on the specific experimental case.
- Buoyancy model: $g_x = 0, g_y = -9.81 \frac{m}{s^2}, g_z = 0, \rho_{ref} = 500\ kg/m^3$
- Heat Transfer: Total Energy
- Turbulence model: standard *k*-ε with scalable wall function
- Turbulent Prandtl Number (Pr_t): 0.95
- Buoyancy Turbulence: Production and Dissipation

Fluid Subdomain

- General Momentum Source: $S_{M,fric,x} = 0\ , S_{M,fric,y} = -\frac{K\,\dot{m}}{0.02\ A} V, S_{M,fric,z} = 0$
- Momentum source coefficient: $k = \frac{K\,\dot{m}}{0.02\ A}$

Solid domain

- Material: INCONEL 625
- Heat transfer: Thermal energy
- Stationary solid domain

Solid subdomain

- Volumetric heat source was given.

6.6 Material Properties

6.6.1 Supercritical Water

In CFX, water properties are calculated based on thermodynamic properties of water and steam from the IAPWS-IF97 database, formulated by Wagner et al. (2000). This database provides an efficient and accurate equation of state for water and steam properties.

There is a limited range of validity for the sets of equations in IAPWS-IF97, so temperature and pressure should be kept within this range. The range of validity for this property package as implemented in CFX is as follows:

$0°C < T \leq 800°C$ for $10 \text{ MPa} \leq P \leq 100 \text{ MPA}$

and

$800°C < T < 2000°C$ for $P < 10 \text{ MPA}$

In CFX, the minimum and maximum temperature and pressure must be set as well as the maximum number of integration points. The minimum and maximum value of temperature and pressure set in CFX depend on the simulated experiment, and the range set should cover the variation range of experimental temperature and pressure. In this study, to improve accuracy in the calculation of the physical properties, the minimum and maximum value of temperature and pressure were set to be equal to those of the experiments, respectively. Furthermore, a maximum of 1000 points was applied for all cases in this study.

6.6.2 INCONEL 625

INCONEL, nickel-chromium alloy 625 (UNS N06625) is used for its high strength, excellent fabricability (including joining), and outstanding corrosion resistance. Alloy 625 is a nonmagnetic, corrosion - and oxidation-resistant, nickel-based alloy. Table 6.1 shows the properties of Inconel 625 used in ANSYS CFX.

Table 6.1 INCONEL 625 Properties ("Inconel 625 Tech Data")

Properties	**In metric units**
Density	8440 kg/m^3
Thermal conductivity	15.5 W/m-K
Specific heat	496 J/kg-K

6.7 Grid Generation

The mesh (computational grid) consisting of hexahedral elements, was created using ANSYS MESHING R18.2. Because of the use of full geometry, relatively coarser mesh was used in the plena and the walls. In the heated section, finer mesh was used to resolve higher solution field gradients occurring. Figure 6.6 (a) shows a sample of the O-grid in a channel. The edge sizing across the O-grid has been explained in Figure 6.6 (b). Non-uniform radial distribution of nodes is used for grid refinement near the wall and uniform coarse grid is used in the solid wall section.

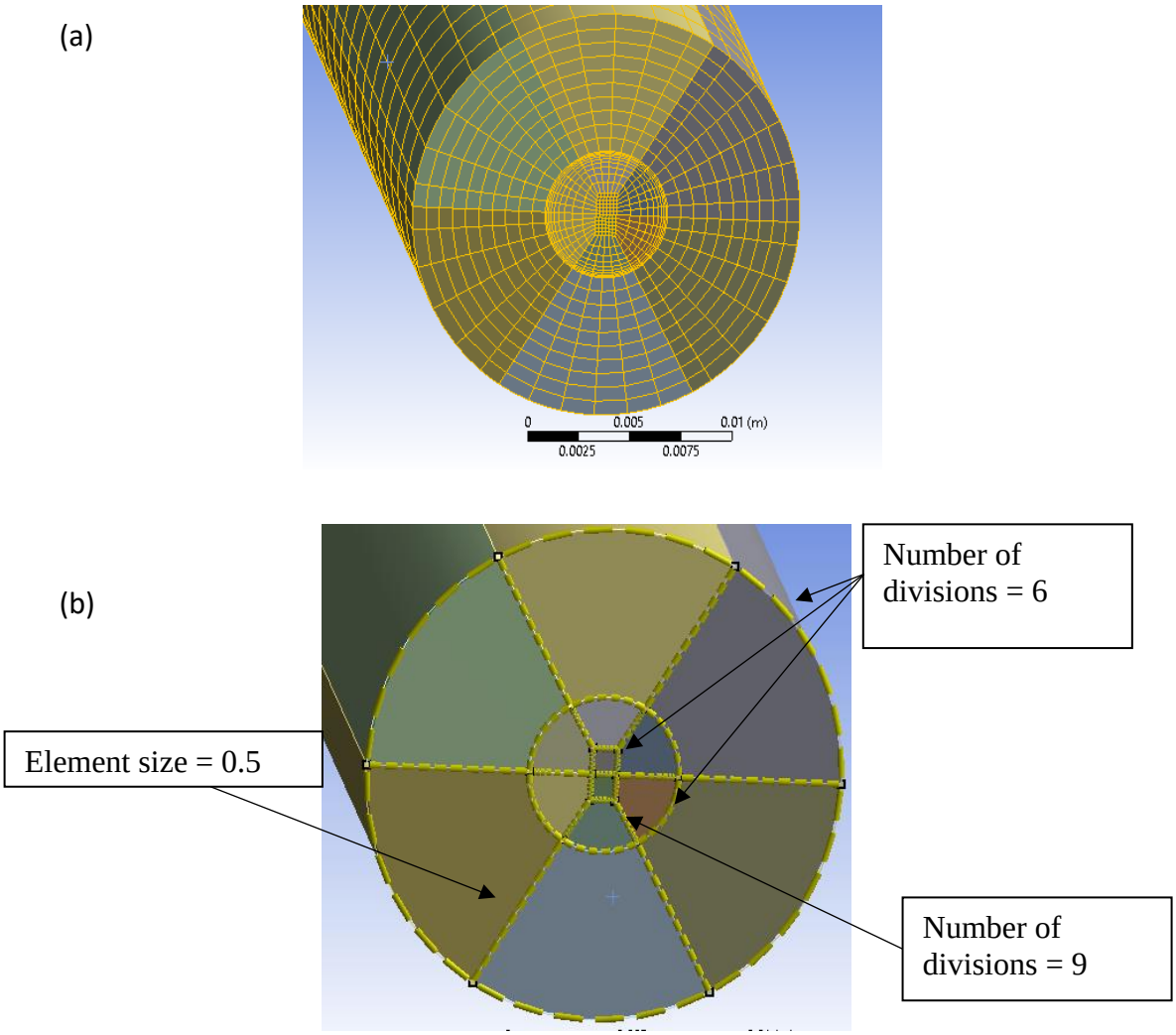

Figure 6.6 a) O-Grid sample b) edge sizing conditions used for O-grid

Because two experiments with different wall thickness are studied, wall element radial spacing size is kept constant i.e. 0.5 mm. Hence 5 radial nodes are used in wall for Xiong et al. cases (2.5 mm thick wall) and 13 radial nodes for Xi et al. cases (6.5 mm thick wall). The plena were coarsely meshed. Figure 6.7 shows the sample views of the mesh in plenum region.

(a)

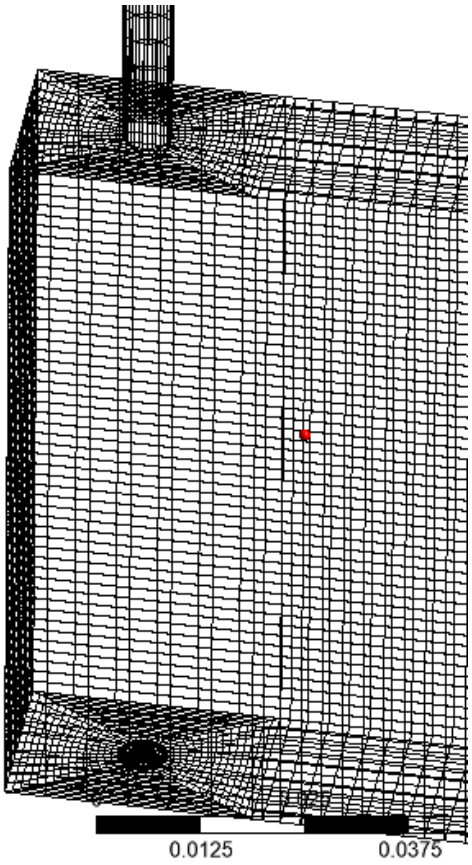

(b)

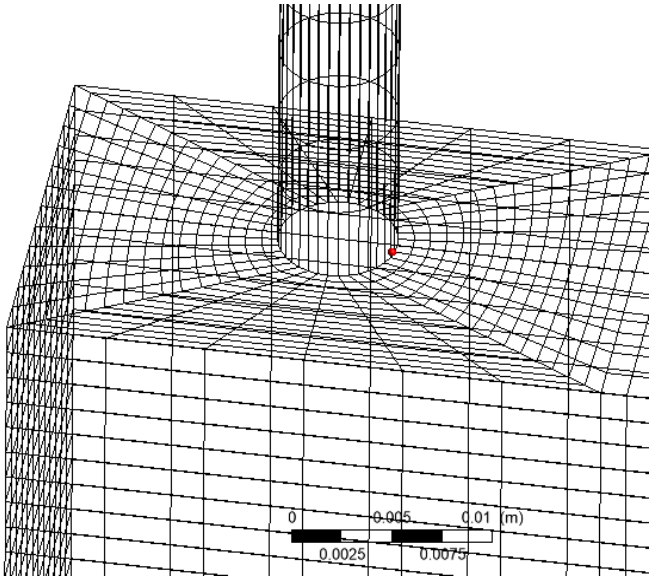

Figure 6.7 Plenum mesh (a) Isometric View (b) Detailed near channel

Grid independence was studied, and it is discussed in Chapter 7. Based on the grid independence study results the meshes summarized in Table 6.2 were used in this study.

Table 6.2 Mesh statistics

Cases	**Without wall**		**With wall**	
	Number of nodes	Number of element	Number of nodes	Number of element
Xiong et al. experiments	1,885,599	1,742,064	1,901,832	1,814,842
Xi et al. experiments	1,885,599	1,742,064	2,209,959	2,066,064

6.8 Solution Domain

Ten fluid domains were defined in the analysis: inlet fluid domain, channel 1 Kin fluid domain, channel 2 Kin fluid domain, channel 1 heated fluid domain, channel 2 heated fluid domain, channel 1 Kout fluid domain, channel 2 Kout fluid domain, outlet fluid domain, and two additional solid wall domains, as shown in Figure 6.8. To model local pressure drops by K factors, fluid subdomains were inserted into channel 1 Kin fluid domain, channel 2 Kin fluid domain, channel 1 Kout fluid domain and channel 2 Kout fluid domain. The solid wall domains were specified to be material INCONEL 625. The wall domains are around the heated fluid domains of the two channels.

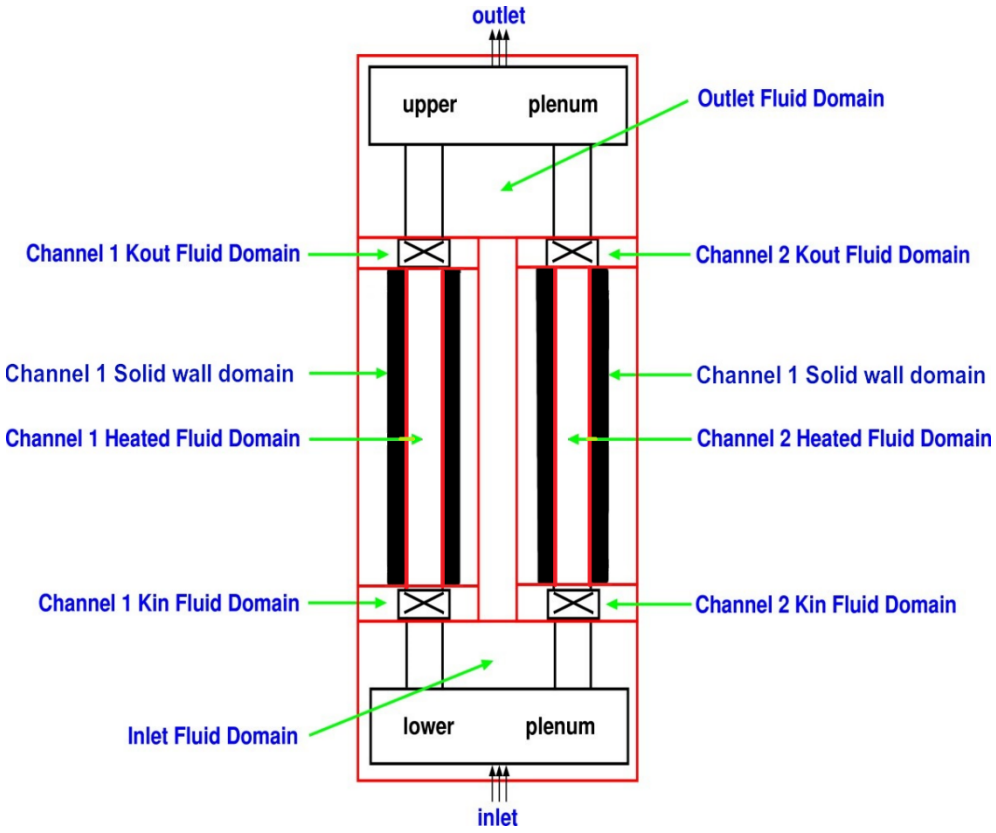

Figure 6.8 Domain declaration

6.9 Numerical Solution Method

ANSYS-CFX uses an element-based finite volume method, which first involves discretizing the domain into a mesh. The mesh is used to construct finite volumes which are used to conserve mass, momentum and energy. In CFX, all solution variables and fluid properties are stored at mesh nodes. The detailed numerical solution method has been explained well by Li (2016) , Bergmann (2015), Ebrahimnia (2014) and the ANSYS CFX Solver Theory Guide (2009)

For this study, double precision was used for the computations throughout. When the maximum normalized residual of each discretized equations was less than 1×10^{-6} and domain imbalances for the continuity, momentum, energy, and turbulence equations were controlled within 0.01 %, then the steady-state calculation was considered to be converged. For transient analyses, the First

Order and Second Order Backward Euler schemes were used, and the solver relaxation parameter was set to be 1.0 rather than the default value of 0.9. The number of iterations per timestep was varied between 30 and 120. The high-resolution advection scheme was used for both steady-state and transient analyses.

Chapter 7

Results and discussions

7.1 Linear Code

The stability analyses of Xiong et al. and Xi et al. experiments were carried out using the linear code described in Chapter 4. Nine cases with a thinner wall (Xiong et al., 2012) and twenty two cases (five cases with uniform power distribution and seventeen cases with non uniform power distribution) with a thicker wall (Xi et al., 2014) were studied. In these analyses, the total mass flow rate was held constant and the channel heating power was varied until the threshold power was found.

7.1.1 Xiong et al. Cases

Table 7.1 shows the comparison of threshold instability boundaries of the experiments and the numerical study without and with wall thermal energy storage effects using subcritical and supercritical Dittus Boelter correlations for heat transfer coefficient predictions. The linear code results without wall thermal energy storage effects showed good agreement with the experimental instability threshold and had an RMS error of 3.68%. It was also observed that the study without wall thermal energy storage effects tended to predict a threshold instability power lower than the experiment. It was known that wall thermal energy storage stabilizes the system (March-Leuba et al., 1993). Modelling the heat transfer coefficient with the standard subcritical Dittus Boelter correlation gave agreement with the experimental boundaries with an RMS error of 2.16%.

Table 7.1 Present study linear solution results compared with the Xiong et al. (2012) experiments

Case	Experimental	Without wall		With wall (Dittus Boelter Correlation)		With wall (Supercritical Dittus Boelter Correlation)	
	Power (kW)	Power (kW)	Diff%	Power (kW)	Diff.%	Power (kW)	Diff.%
1	67.9	65.5	3.53	70	-3.09	68.9	-1.47
2	66	63.5	3.79	66.5	-0.75	66.3	-0.45
3	65.6	62.5	4.73	64	2.43	63.8	2.74
4	67	63.5	5.22	66	1.49	65.8	1.79
5	66	64	3.03	66	0	65.7	0.45
6	64.6	62	4.02	65	-0.61	64.2	0.61
7	69.3	67	3.32	71	-2.45	70.5	-1.73
8	68.9	68.1	1.16	70	-1.59	69.8	-1.30
9	67.9	66	2.80	70.5	-3.82	70	-3.09

When using the supercritical Dittus Boelter correlation, the RMS error dropped to 1.75%. Without wall thermal energy storage, the instability threshold was underpredicted, but the inclusion of wall thermal energy storage effects increases the threshold power and the predictions become closer to the experimental onset threshold.

7.1.2 Xi et al. Cases

7.1.2.1 Uniform Power Profile

Table 7.2 shows the summary of the numerical predictions of Xi et al. uniform power profile experiments. Based on the Xiong et al. cases with uniform power, it was expected that the supercritical Dittus Boelter correlation would give better predictions of the instability threshold, so only that correlation was used for the further cases. The RMS error without the wall thermal

energy storage effects is 1.96%, whereas the RMS error with wall thermal energy storage effects is 1.60%.

Table 7.2 Comparison between experiment and present study with and without wall thermal energy storage effects.

Case	Experimental Power (kW)	No Wall (kW)	Difference %	With wall Supercritical Dittus Boelter correlation (kW)	Difference %
1	79.02	78	-1.29	78.1	-1.16
2	77.22	76.2	-1.33	76.5	-0.94
3	76.21	74.5	-2.25	74.7	-1.99
4	72.91	71.2	-2.34	71.6	-1.79
5	71.42	69.8	-2.27	70.1	-1.85

Summary of instability threshold for uniform power cases is shown in the Figure 7.1.

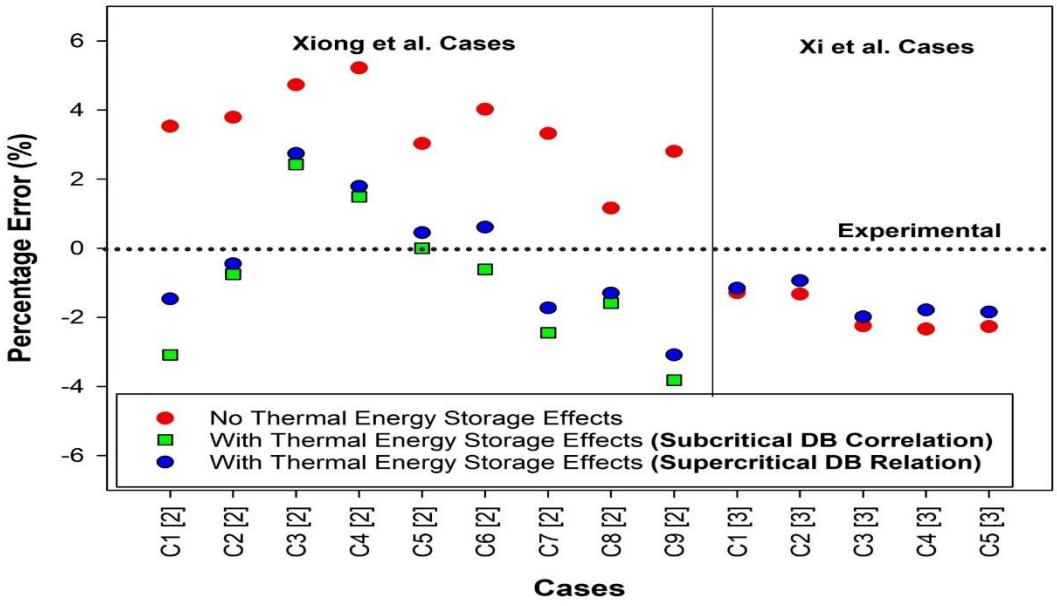

Figure 7.1 Summary of instability threshold [1] Xiong et al. [2] Xi et al. (Uniform Power cases)

It can be seen from the figure that the cases with uniform power distribution gave better predictions with wall thermal energy storage effects. It was also observed in Xiong et al. cases, that the predictions with heat transfer coefficient by Dittus Boelter Correlation in supercritical region were better than the predictions with heat transfer coefficient by Dittus Boelter Correlation in subcritical region. Hence, heat transfer coefficient was predicted with Dittus Boelter correlation in supercritical region throughout the further study.

7.1.2.2 Non-uniform Power Profiles

The non-uniform power profile cases were divided into three categories by Xi et al. (2014), namely: lower power boundary (LPB), intermediate boundary (IB), high power boundary (HPB). The LPB, IB, and HPB cases are the instability cases at time t1, t2 and t3 respectively as indicated in Figure 3.3 (b). Heated sections were divided into two sections and powers were applied according to the experimental details described in Chapter 3. The mass-flowrates were varied for determining the instability threshold while keeping the power profile constant.

LPB and IB cases

Table 7.3 shows the summary of the numerical predictions of the ratio of the instability power threshold to the mass flow rate for Xi et al. lower power boundary cases.

Table 7.3 Comparison of LPB between experiment and present study with and without wall thermal energy storage effects

Case	P/$\dot{m}$ (kJ/kg)	P/$\dot{m}$ (No Wall) (kJ/kg)	Difference %	P/$\dot{m}$ (With wall) (kJ/kg)	Difference %
1	1264.57	1353.72	-7.04	1411.94	-1.85
2	1509.41	1555.31	-3.04	1603.70	-1.79
3	1565.91	1561.90	0.25	1610.71	-1.99
4	1563.22	1538.59	1.57	1585.93	-0.94
5	1594.17	1585.93	0.51	1620.84	-1.16

The RMS error without wall heat storage effect is 3.51%. Incorporation of the wall thermal heat storage increased the RMS error to 6.13%. Figure 7.2 shows the comparison of predictions of LPB cases with and without wall energy storage effects.

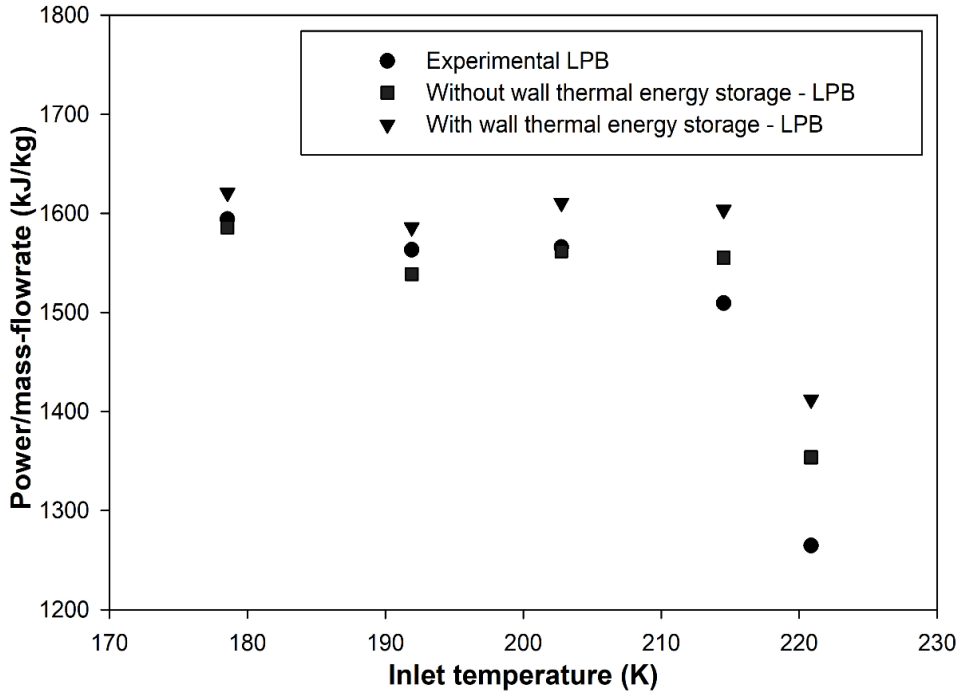

Figure 7.2 Experimental LPB cases versus 1D analytical With and without wall energy storage effects

Table 7.4 shows the summary of experimental and numerical threshold boundary of IB cases.

Table 7.4 Comparison of IB between experiment and present study with and without wall thermal energy storage effects

Case	**P/$\dot{m}$ (kJ/kg)**	**P/$\dot{m}$ (No Wall) (kJ/kg)**	**Difference %**	**P/$\dot{m}$ (With wall) (kJ/kg)**	**Difference %**
1	1318.38	1422.40	-7.889	1440.87	-9.290
2	1541.70	1584.96	-2.805	1631.57	-5.829
3	1641.25	1665.87	-1.499	1706.88	-3.998
4	1654.70	1636.38	1.107	1681.01	-1.589
5	1678.92	1655.92	1.369	1706.88	-1.665

The same trend as of lower power boundary (LPB) continued for intermediate boundary (IB) cases. Without wall thermal energy storage effect the RMS error was 3.88% whereas with wall thermal energy storage effects, it increased to 5.32%. The higher latter value is believed due to omission of axial conduction in the wall. Figure 7.3 shows the comparison of predictions of IB cases with and without wall energy storage effects.

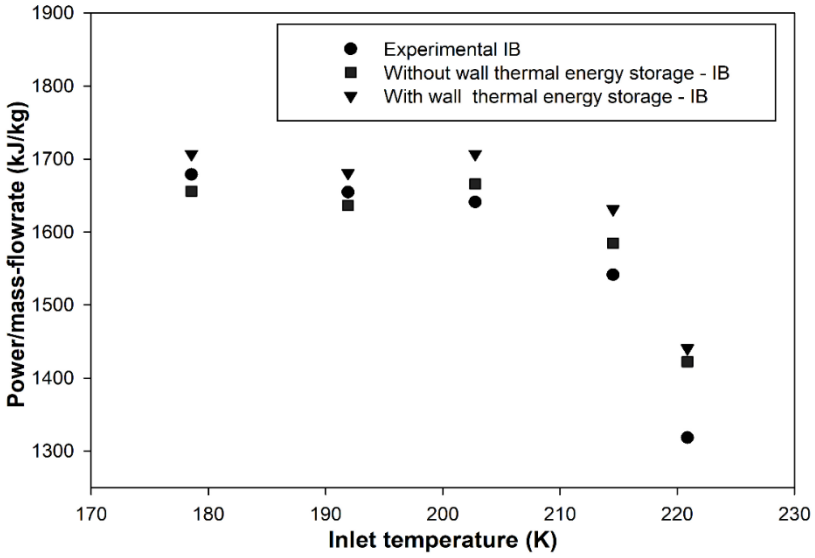

Figure 7.3 Experimental IB cases versus 1D analytical With and without wall energy storage effects

Axial conduction would be important when there is a sharp and sudden change in electrical power. Because the sudden change in power shape is not encountered in real systems, the increased RMS error for the present predictions of the cases is considered acceptable. It was also observed that the study without wall thermal energy storage effect (for LPB and IB) tended to predict the threshold instability mass flowrate less than the experiment, unlike in the Xiong et al. and Xi et al. uniform power cases.

HPB Cases

In all HPB cases, the step profile is smaller than LPB and IB cases as shown in Figure 3.3 (b). Table 7.5 shows a summary of numerical predictions of the HPB cases. The observed trends for the HPB cases were similar to the previous uniform power profile cases. The study without wall thermal energy storage effects tended to predict a threshold instability mass flow rate higher than the experiment whereas with wall thermal energy storage effects, the mass-flow rate predictions decreased making them closer to the experimental values. The RMS error without wall thermal energy storage effect was 7.72% whereas with wall thermal energy storage effects, it was decreased to 4.81%.

Table 7.5 Comparison of HPB between experiment and present study with and without wall thermal heat storage effects.

Case	**P/$\dot{m}$ (kJ/kg)**	**P/$\dot{m}$ (No Wall) (kJ/kg)**	**Difference %**	**P/$\dot{m}$ (With wall SDB correlation) (kJ/kg)**	**Difference %**
1	2120.17	1779.15	11.67	1922.63	4.55
2	2165.91	1862.55	10.33	1967.04	5.29
3	2168.60	1922.63	9.31	1986.72	6.29
4	2235.87	1954.15	9.77	2020.39	6.71
5	2262.78	2020.39	6.83	2106.06	2.88
6	2014.34	2091.28	6.46	2143.94	4.11
7	2077.13	2143.94	5.25	2207.46	2.44

Figure 7.4 show the comparison of experimental instability threshold HPB with numerical prediction (with and without wall thermal energy storage effects) of the linear code.

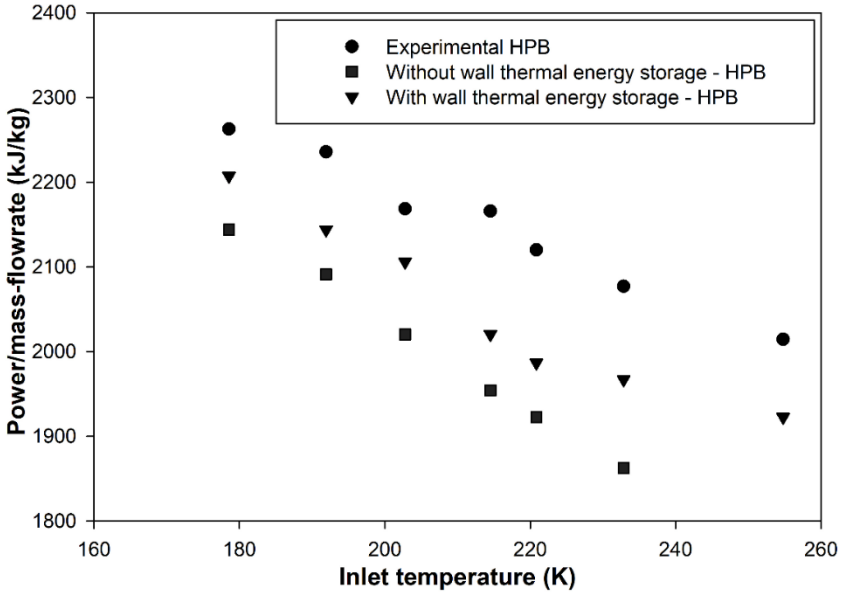

Figure 7.4 Experimental IB cases versus 1D analytical With and without wall energy storage effects

The summary of all the non-uniform power cases is shown in Figure 7.5.

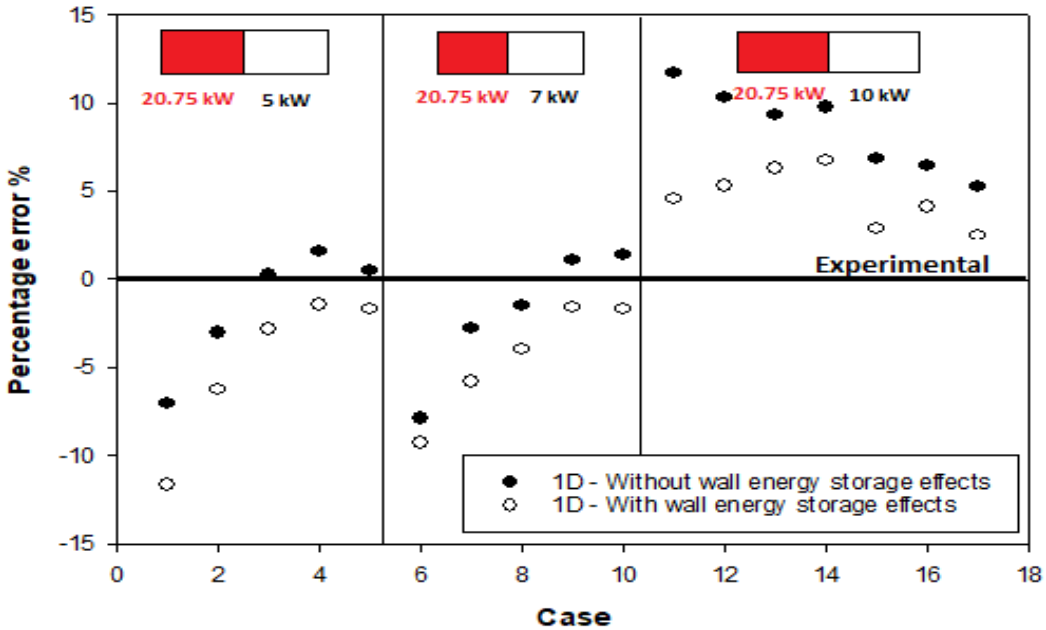

Figure 7.5 Summary of Xi et al. Cases (Non-uniform power profile)

It can be clearly observed that the LPB and IB cases performed worse with wall thermal energy storage effects than the cases without wall thermal energy storage effect. As discussed before, this can be improved on including wall thermal energy storage effects in linear solution. It was also observed that the HPB cases predictions were better with wall thermal energy storage effects.

7.1.3 Single Channel and Identical Parallel Channels

Numerical modelling of a single channel with and without wall thermal energy storage effects was performed for two cases of uniform power for the Xiong et al. geometry. Table 7.6 summarizes the predictions.

Table 7.6 Single channel cases (Pressure: 23 MPa, inlet temperature: 513K)

Case	Mass flowrate	Threshold Power (kW) (No wall)	Threshold Power (kW) (With wall)	Percent difference in with the wall and no wall results %
1	0.0168	30.78	62.48	50.73%
2	0.0176	31.36	64.12	51.09%

It was observed that the wall thermal energy storage makes a significant effect on the instability boundary threshold. About a 50% difference was observed between with and without wall thermal energy storage effects results in both the cases. It was observed that the effect of modelling the wall in single channel affects greatly the instability. When, two identical parallel channels were modelled, it was observed that the instability boundary power without wall thermal energy storage was exactly equal to the instability boundary power with wall thermal energy storage. Also, there was no effect of a change in the heat transfer coefficient correlation. Because the transfer function involves the difference between the total pressure outlet perturbations of two channels, the effect of the wall heat storage may perfectly cancel for identical channels. Due to the cancelling effect,

the change in heat transfer coefficient does not affect the instability thresholds. Hence, for channels that are only mildly dissimilar, it may be acceptable to ignore wall thermal energy effects in determining the instability boundary. The instability threshold power observed in single channel without wall heat storage effects is half of the instability power of two identical parallel channels. So, it was observed that the results of single channel and parallel channels can easily be related.

7.1.4 Period of Oscillation

It is important to predict a correct period of oscillation along with the instability threshold. In this study, the cross-over frequency is used to determine the major period of oscillation of any case, as discussed in Chapter 4. Table 7.7 shows the comparison of the period of oscillation predictions with and without wall thermal energy storage effects.

Table 7.7 Comparison of the period of oscillation of experimental and numerical

Case	Experimental Period of oscillation (s)	Period of oscillation (s) (No wall)	Period of oscillation (s) (With wall)
Xiong et al. cases 1-9	1	0.82	0.89
Xi et al. Uniform power	1.26	1.1	1.17
Xi et al. LPB, IB	1.6	2.183	1.9
Xi et al. HPB	1.3	1.658	1.38

It can be observed that consideration of wall thermal energy storage effects always improves the predictions of the oscillation period. Also, the prediction of oscillation period for Xi et al. LPB and IB cases is comparatively inaccurate compared to the uniform power and HPB results. These cases with a non-uniform power profile, accounting for axial conduction may be important in the prediction of an accurate oscillation period.

7.2 Non-Dimensional Parameters

Constructing an experimental set up for supercritical water, is very expensive and difficult because the pressure is above 23 MPa and the temperature is within the range of 350 K to 900 K. Hence, many researchers are focussing on supercritical fluid experiments with CO_2, R23, and Ammonia. The supercritical pressure and temperature required for CO_2 is low compared to supercritical water. In order to infer results for water based on CO_2 experiments, it was important to derive and validate a set of non-dimensional parameters, which can completely convert the experimental data of one fluid to another.

Table 7.8 Instability threshold of the CO_2 numerical cases

Case	Pressure (MPa)	Temperature (K)	mass flow (kg/s)	Threshold Power (kW)	Thickness (mm)	N_{tpc} CO_2	N_{wall} CO_2
1	8	291	0.0365	12	2.5	1284.08	7155.70
2	8	291	0.0365	12.3	5.5	1316.18	4736.86
3	8	293	0.0365	11.5	2.5	1230.57	7107.25
4	8	293	0.0365	12	5.5	1284.08	3979.95
5	8	293	0.0365	12.5	7.5	1337.58	1049.35
6	8	293	0.035	11.1	2.5	1450.70	7241.42
7	8	293	0.035	11.4	5.5	1495.34	4428.17
8	8	293	0.035	11.8	7.5	1517.66	1633.37
9	8	297	0.0365	11.3	2.5	1177.07	7054.40
10	8	297	0.0365	11.8	5.5	1209.17	4424.19

To validate the non-dimensional parameters derived in Chapter 5, numerical cases of a horizontal natural circulation loop with CO_2 were analysed with the linear frequency-domain code. The

instability thresholds for different boundary conditions were determined using an initial steady state solution from the SPORTS code. The geometry was considered to be similar to the horizontal loop geometry used by Zhang (2018) except for the channel wall thickness. Wall thicknesses of 2.5 mm, 5.5 mm and 7.5 mm were used. N_{TPC} and N_{SPC} of the data were calculated. Table 7.8 shows the details of all the CO_2 cases. Then, using N_{TPC} and N_{SPC}, the CO_2 cases were converted into equivalent water cases. N_{wall} was employed to calculate the new wall thicknesses for the water cases. Table 7.9 shows the converted water cases using non-dimensional parameters.

Table 7.9 Converted Water cases using Non-dimensional parameters

Cases	**Pressure (MPa)**	**Temperature (K)**	**mass flow (kg/s)**	**Threshold Power (kW)**	**Thickness (mm)**
1	25	372.531	0.0365	39.12	3.11
2	25	372.531	0.0365	40.10	6.5
3	25	373.358	0.0365	37.49	3.05
4	25	373.358	0.0365	39.12	6.55
5	25	373.358	0.0365	40.75	8.01
6	25	373.358	0.035	36.17	3.26
7	25	373.358	0.035	38.57	5.72
8	25	373.358	0.035	40.27	8.13
9	25	377.054	0.0365	36.32	2.97
10	25	377.054	0.0365	38.36	6.37

The converted water cases were then analysed with wall thermal energy storage effects using the SPORTS code steady state results and the linear frequency domain code. It was found that, the numerical instability boundary with wall thermal energy storage effects for natural circulation was

very close to the instability boundary predictions determined using the non-dimensional parameters. The relative RMS error was 4.6%. Table 7.10 compares the analytical threshold power (Using the non-dimensional parameters) and numerical threshold power (using the linear code).

Table 7.10 Comparison between threshold boundary power from non-dimensional parameters and the Linear code results

Case	Threshold power (kW) Using non-dimensional parameters	Threshold power (kW) using Linear code	Percentage error %
1	39.12	37.5	4.16
2	40.10	38.9	3.01
3	37.49	39.4	-5.07
4	39.12	36.1	7.74
5	40.75	38.5	5.54
6	36.17	36.4	-0.61
7	38.57	38.4	0.46
8	40.27	39.3	2.43
9	36.32	34.3	5.57
10	38.36	36.2	5.63

7.3 Numerical Analysis Using CFX

Numerical models were developed for the experiments of Xiong et al. and Xi et al. using ANSYS-CFX with and without wall thermal energy storage effects. In this study, the heating power was kept constant at the experimental value and the total mass flow rate was varied until the threshold mass flow rate was determined.

7.3.1 Determining the Instability Threshold

The instability threshold mass flow rate is determined by a transient analysis in which the time variation of the inlet mass flow rates in the heated channels are monitored. The initial condition for the transient analyses is a steady-state analysis. Therefore, for every run with different inlet mass flow rate, the steady-state solution must first be performed and obtained. The inlet and outlet channel mass flow rates are monitored to determine if oscillations grow in amplitudes with time. If so, the flow is said to be unstable and this kind of instability is defined as an oscillatory

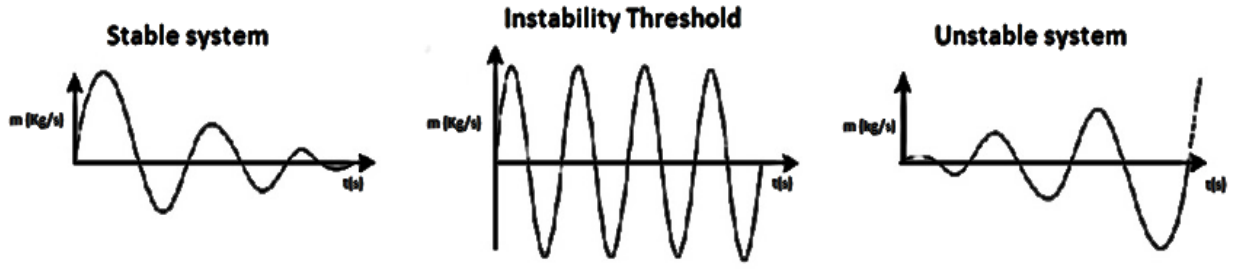

Figure 7.0.6 Stability of systems

instability. If the oscillation amplitudes become constant with time, the flow is said to be at the instability threshold, or neutrally stable (Li 2016). It should be noted that transient analyses must be run long enough (at least 30s is required in this study) to clearly identify a flow instability.

For a given case, the approach to determine the instability threshold begins with a relatively high mass flow rate for which the flow is stable. Then the heating power of two parallel channels are held constant as that of the experimental power and the mass flow rate is reduced in steps until sustained or diverging oscillations are observed. In this study, a decrement of 0.0005 kg/s was used in the search for the instability boundary. Within this decrement, if the higher mass flow rate caused a stable flow while the lower mass flow rate caused an unstable flow, then the average of these two mass flow rates was chosen as the threshold mass flow rate or instability boundary.

7.3.2 Grid Independence

Without Wall Thermal Energy Storage Effects

Li (2016) proved in her study that the prediction of instability threshold is not affected by different mesh sizes within a certain range. Even the largest difference was recorded to be only 1.15% (< 2%), all the other discrepancies were within 1%. Hence, no grid independence study was performed for the analyses without a wall and the number of nodes used by Li (2016) was considered acceptable.

With Wall Thermal Energy Storage Effect

By varying the number of nodes distributed radially in the wall, two meshes with a different number of nodes and different spatial grid sizes were generated using ANSYS Meshing.

Table 7.11 Grids used for mesh independence study

Mesh	Nodes in wall	Total nodes	Total elements
Mesh 1	15	2,518,086	2,317,286
Mesh 2	10	2,209,959	2,066,064
Mesh 3	5	1,901,832	1,814,842

Three meshes listed in Table 7.11 were tested using timestep of 0.01s for confirming the grid independence of the model with the wall thermal energy storage effects. With these three meshes, the oscillatory instability boundary of the Case 1 Xiong et al. was determined and compared. There was no noticeable difference (0%) in thermal hydraulic instability determined by three meshes. Furthermore, considering the mass flow rate decrement used in this study is a small enough value, 0.0005 kg/s, threshold mass flow rates predicted by the different meshes were the same. The oscillation pattern for the grids for Xiong et al. Case 1 at 0.0334 kg/s is shown in Figure 7.7. In the graphs of the transient response in this section, the normalized channel inlet mass flow rate, is

calculated by dividing the transient channel inlet mass flow rate by the initial transient channel inlet mass flow rate at t = 0 s.

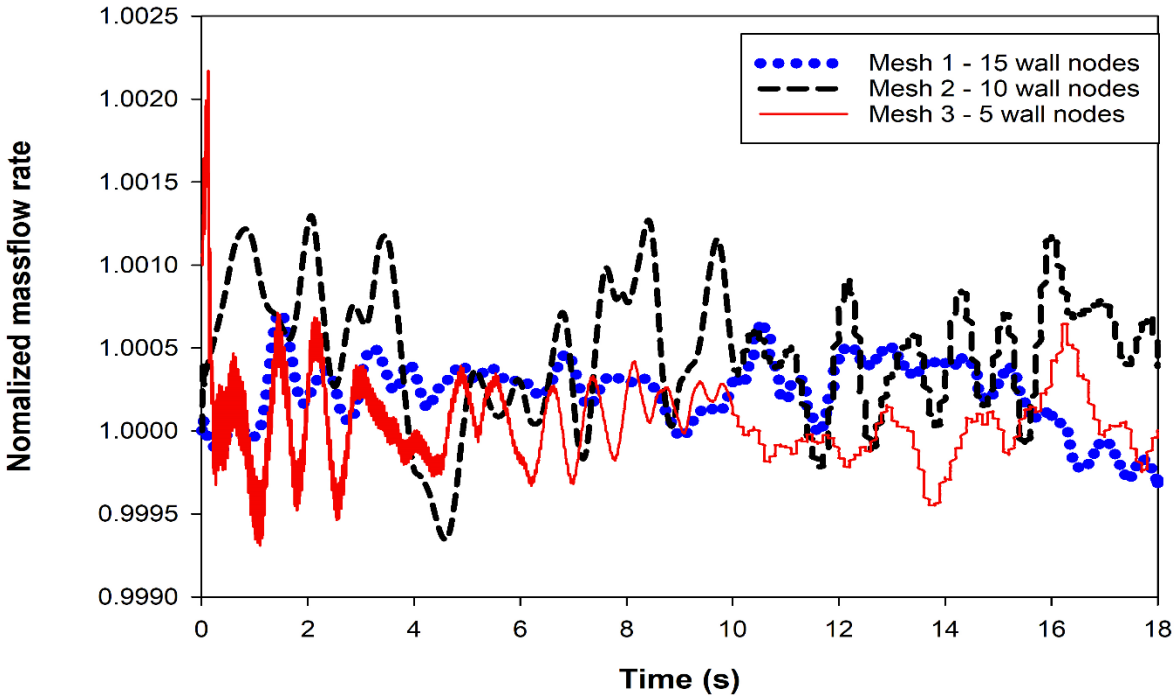

Figure 7.7 Channel 1 Oscillations (With wall, Xiong's Case 1- 0.0334 kg/s)

It was observed that the oscillation amplitude changes with the node refinement in the wall, but the instability threshold is the same for all the cases. The computational time required for each run was about 200 wall clock hours (8.38 hours) with the use of 30 cores on the Grex compute server.

7.3.3 Domain Symmetry Boundary Condition Effects

In a previous study, Li (2016) considered symmetry of the model and half the geometry was modelled. The results without consideration of wall thermal energy storage effects were in very good agreement with the experimental instability threshold. Hence, it was decided to work initially with the same symmetric model and add wall thermal energy storage effects. It was found that

however, the half geometry model, when analysed with wall thermal energy storage effects, predicted stable results for known unstable conditions.

Exploration of possible causes of unexpected results with a wall energy storage and symmetry led to the idea of solving the full geometry. This change enabled the model to capture the flow dynamics, changing the predictions with wall thermal heat storage effects. The instability threshold was then predicted within the experimental uncertainty limits and full geometry was used in subsequent analyses.

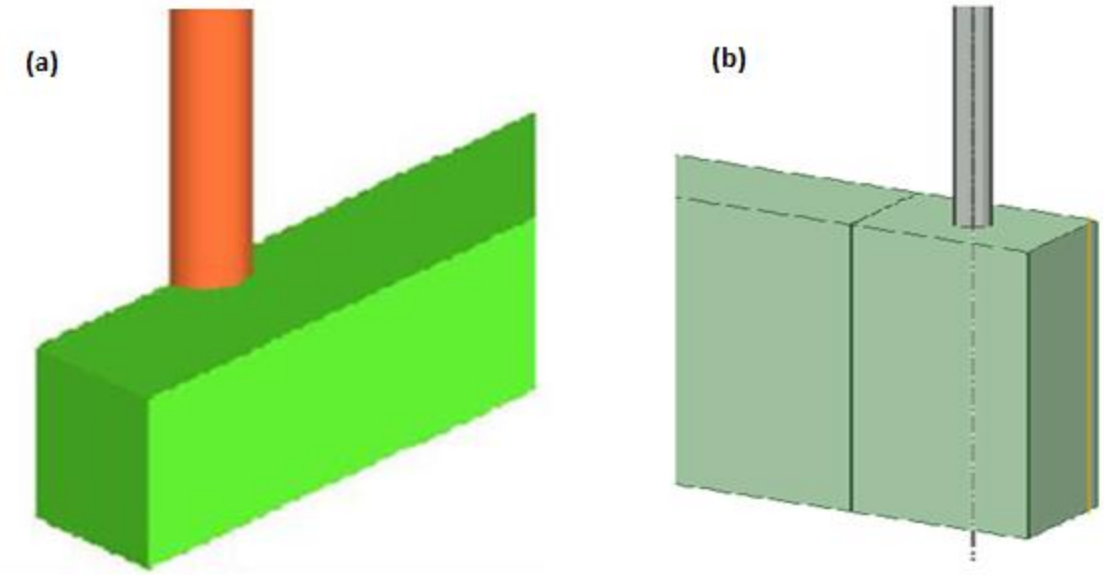

Figure 7.8 (a) Half model (Li 2016) (b) Full model

Table 7.12 compares the instability threshold of Case 1 and Case 3 with the half and full models. It was observed that, for Case 1, the instability threshold without wall thermal energy storage effects is not affected much by the use of symmetry (1.19%) but the instability threshold of the case with wall thermal energy storage effects varies by 9.2%. Also, in Case 3 the mass flow rate became very small, causing the supercritical property table temperature limit to exceed, and it was impossible to predict the instability threshold with symmetry.

Table 7.12 Half model vs Full model

Experimental case	**Without wall energy storage effects**		**With wall energy storage effects**	
	Half model	Full Model	Half model	Full model
Case 1	0.0340 kg/s (-1.19%)	0.0336 kg/s	0.0305 kg/s (-9.22 %)	0.0336 kg/s
Case 3	0.0360 kg/s (-1.12%)	0.0356 kg/s	Exceeded temperature range	0.0348 kg/s

The normalized inlet mass flow rate results for the case with a known unstable mass flow rate of 0.0334 kg/s and wall thermal energy storing effects for half and full geometry is shown in Figure 7.9. The erroneous stable behaviour of the half geometry predictions can be clearly seen.

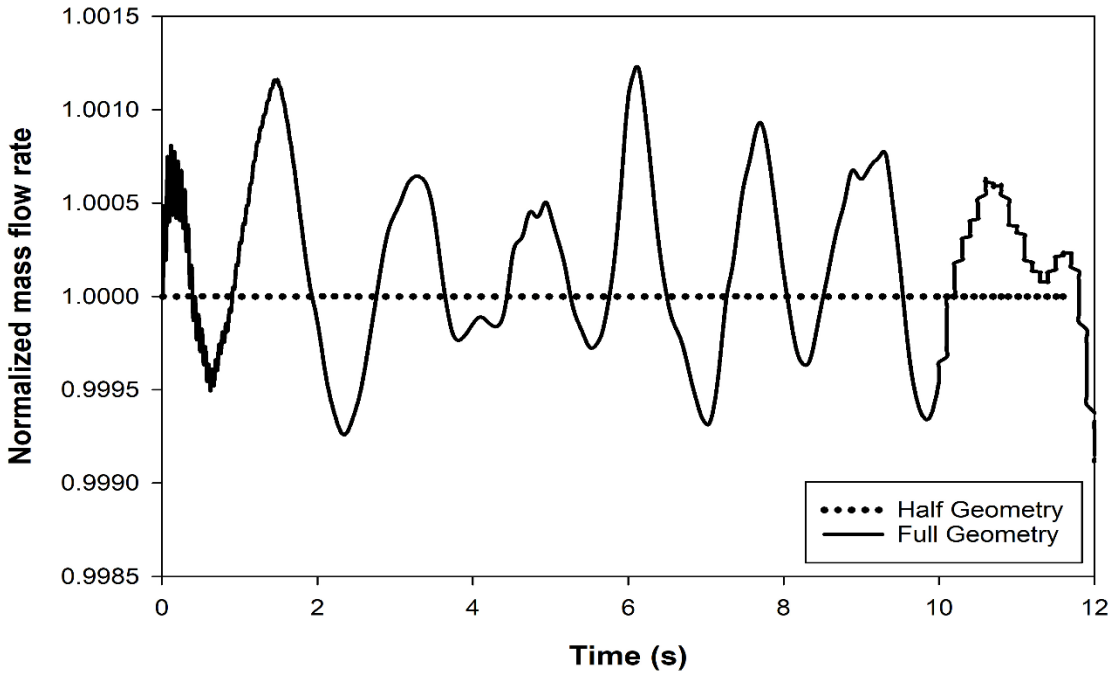

Figure 7.9 Full model versus Half model for Xiong et al. Case 1 at 0.0334 kg/s

7.3.4 Enlarged Plena

Initial tests with the full geometry were better but obtaining tight convergence (maximum residual less than 1×10^{-6}) was not possible. The solution residual distribution was examined at it was found that the maximum residuals were in the upper plenum and lower plenum regions. This led to an examination of velocity profiles in the plena. Figure 7.10 (a) shows the high velocity stream at the end of the channels creating small circulations around the area in the original small sized upper plenum. To avoid the jet like phenomenon at the end of channel, the height of plenum was increased by 4 times. It was observed that the high velocity stream stopped striking the upper wall of the upper plenum (Figure 7.10 (b)) and that the residuals improved.

(a)

(b)

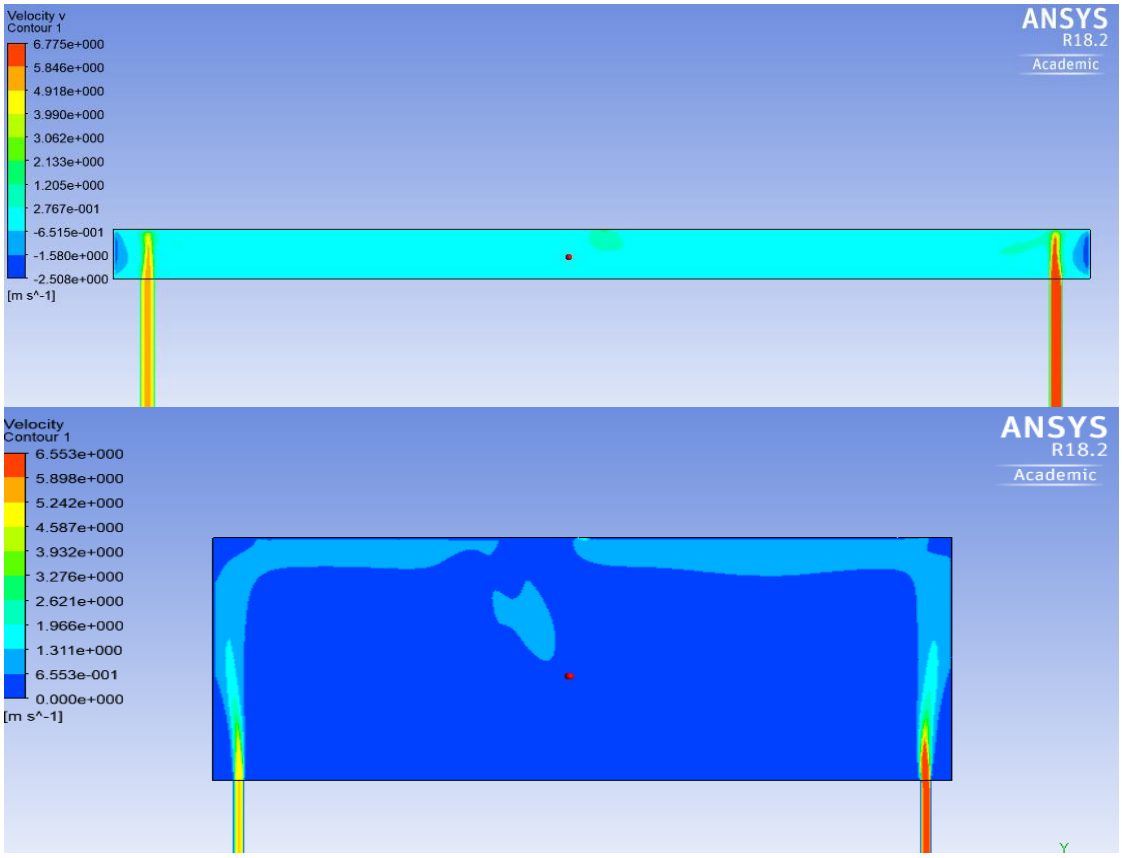

Figure 7.10 Contours in the upper plenum (a) small plenum case, and (b) large plenum case

Figure 7.10 (b) shows the effect of the larger plenum clearly. The difference in instability threshold prediction due to change in the plenum size was not initially considered in the current study because Li (2016) found that the using a larger plenum did not affect the stability boundary predictions significantly. In the present work, however significant improvement in convergence behaviour was obtained. Additional improvements were obtained by increasing the lower plenum height to 90 mm and increasing the inlet from 20 mm x 20 mm to 200 mm x 20 mm. This helped to reduce the velocity in the lower plenum and maintain relatively constant pressure. Residual and convergence was further improved.

7.3.5 Fast Fourier Transform

Period of oscillation is an important factor of the flow dynamics. Period of oscillation was reported to be about 1 s in the experiments (Xiong et al. 2012; Xi et al. 2014). But previous numerical studies (Li 2016; Xi et al. 2014) reported the numerical period of oscillation about 5s. To investigate this issue, a Fast Fourier transform (FFT) was performed on the experimental and numerical data.

Fast Fourier Transform(FFT) of Experimental Data

Figure 7.11 shows results of the FFT on experimental data of Xiong et al. Case 1. It was observed that though the dominant frequency was about 1.1 s^{-1} (oscillation period of 0.9 s) the experimental data also had a secondary (less dominant) frequency of 0.18 s^{-1} (oscillation period of 5.65 s). Hence, it was proved that even though the dominant period of oscillation in the experiment is about 1 s, the dynamics also has a period of oscillation near to 5.5 s which the numerical analyses were picking up.

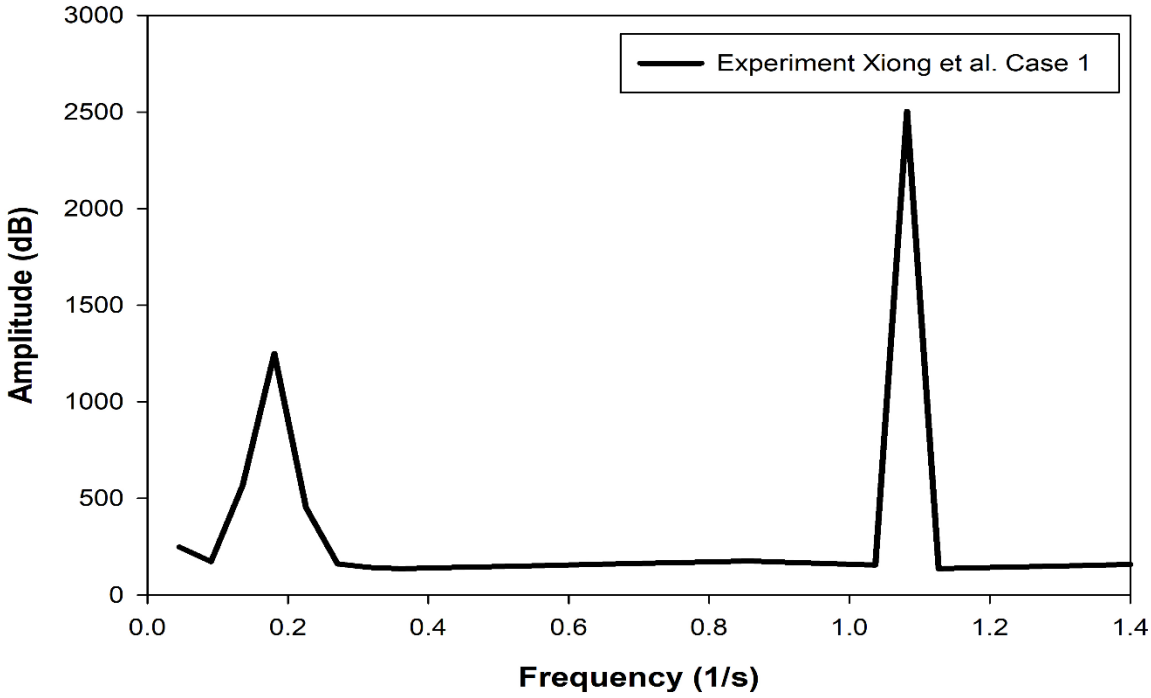

Figure 7.11 Fast Fourier transform of Xiong's experimental Case 1

7.3.6 Temporal Independence

Without Wall

In the temporal independence tests carried out by Li (2016), the lower limit of the timestep size was 0.01 s. In this work, the Case 1 from the previous study was rerun using a timestep size of 0.001 s. Using the First order transient scheme and half geometry, the cases were studied for temporal independence. An example of these results is for a mass flow rate of 0.0338 kg/s. For this mass flow rate, behaviour was predicted to be stable using timestep size of 0.001 s, whereas it

was reported as unstable using a timestep size of 0.01s. The comparison for Li (2016) results with the timestep size of 0.01 s with the results using timestep size of 0.001 s is shown in Figure 7.12.

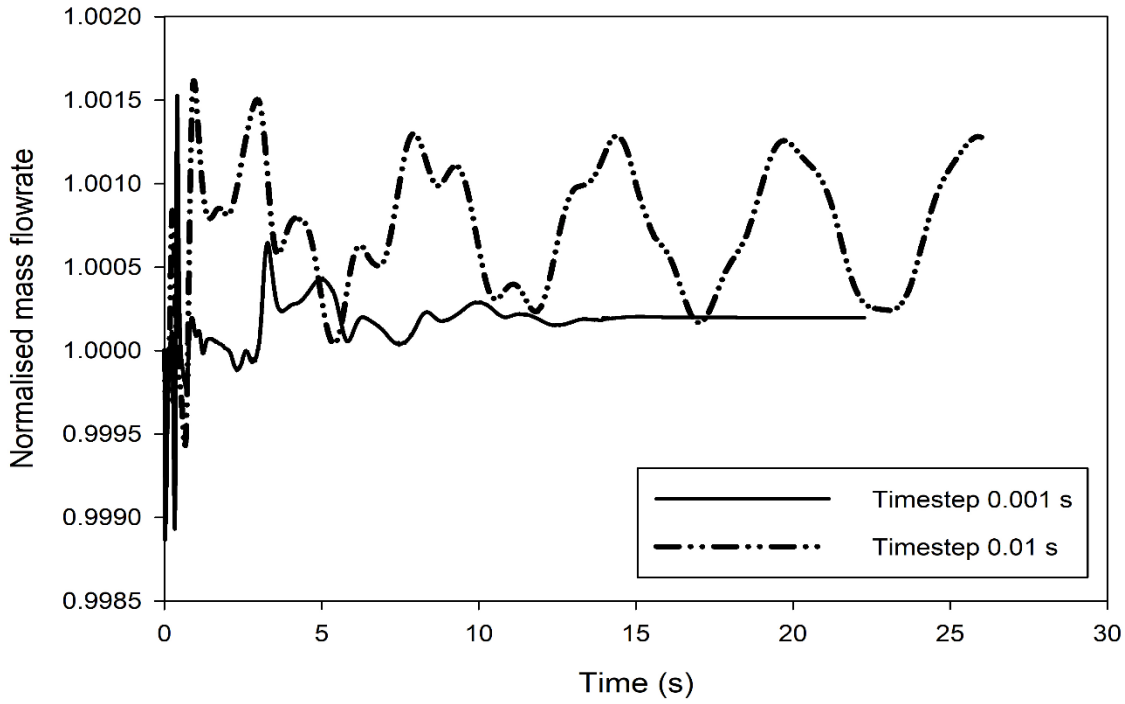

Figure 7.12 Comparison of different timestep results (Half geometry, Case 1, 0.0338 kg/s)

Hence, temporal convergence was identified as a critical issue. The focus of subsequent temporal convergence testing was using on the full geometry and enlarged plena with wall thermal energy storage effects, for the reasons explained in sections 7.3.3 and 7.3.4.

With Wall Thermal Energy Storage Effect

Wall thermal energy storage effects and full geometry were used in the study of the effect on the threshold boundary of Xiong et al. experimental Case 1 using timestep sizes of 0.001 s, 0.005 s, and 0.01 s. It was found that the instability threshold predicted was the same for three timestep sizes. The oscillation amplitude and pattern, however, were changed. The instability threshold

found using all the timestep sizes was 0.0336 kg/s. Also, some small magnitude, high frequency numerical oscillations were noticed for smaller timestep sizes of 0.001 s and 0.005 s at very first few seconds. The numerical oscillations were increased as the timestep size was reduced. Figure 7.13 demonstrates the normalized channel 1 inlet mass flow rate behaviour predicted using different timestep sizes.

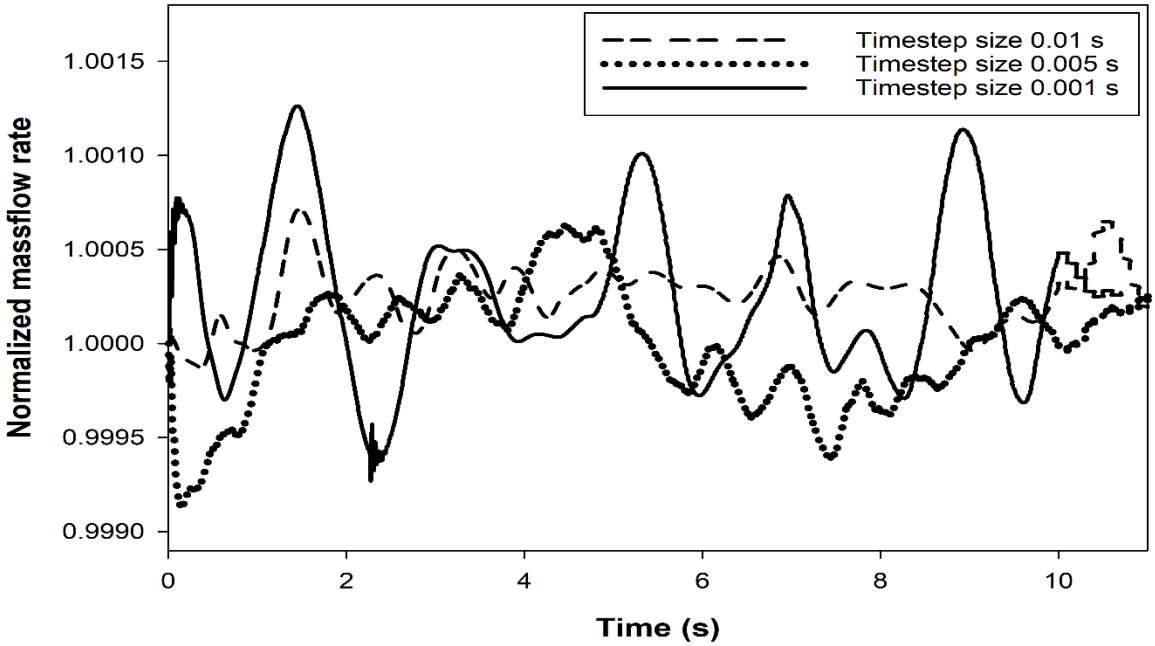

Figure 7.13 Normalized mass flow rate for channel 1 at 0.0338 kg/s using various timestep sizes

To reduce the numerical oscillations, 120 coefficient loop iterations were set for each timestep for the cases with the timestep of 0.001s which ran for 685 hours (more than 28 days) using 40 cores. Because of this very significant requirement of computational resources, only Xiong et al. Case 1 was analysed for temporal convergence. A timestep size of 0.01 s with 30 coefficient iterations per timestep was chosen as the acceptable compromise of accuracy and computational efforts. The Fast Fourier transform response for all the timesteps is discussed in section 7.3.7.

7.3.7 Fast Fourier Transform of Numerical Data

Without Wall Thermal Energy Storage Effects

In the previous study by Li (2016), it was concluded that the first order transient scheme gives smooth transient response while the second order transient gives numerical noise. A Fast Fourier Transform (FFT) of the same data was performed and it was found that the oscillations that were previously considered numerical oscillations represented a 1s period of oscillation.

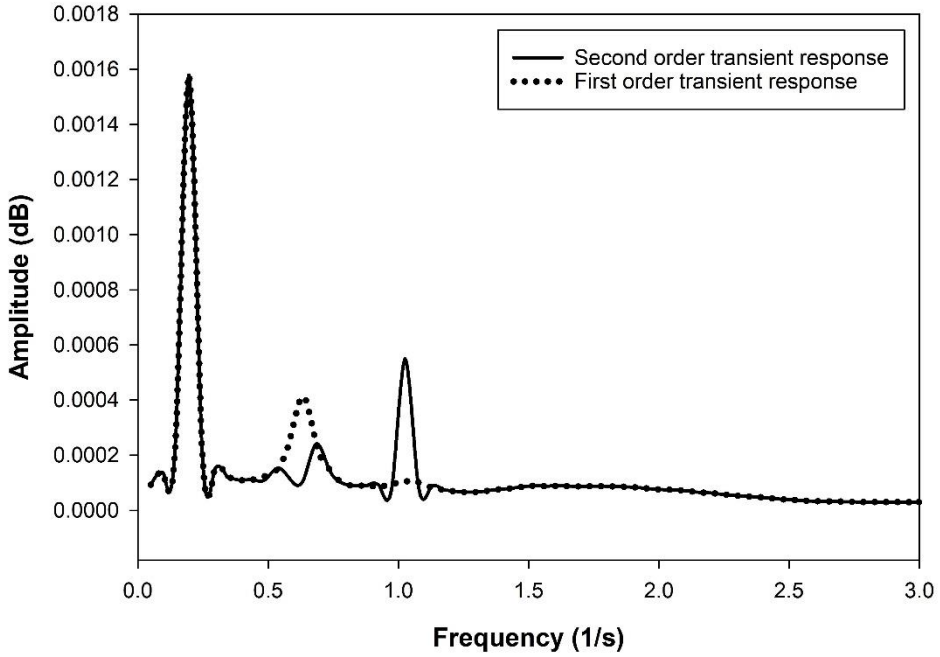

Figure 7.14 FFT analysis of Li (2016) Case 1 (First order transient scheme and Second order transient scheme)

Figure 7.14 represents the Fast Fourier transform of first order transient scheme and second order transient scheme of the cases by Li (2016). It can be clearly seen that the dominant frequency in both analyses is 0.2 s^{-1} (i.e. about 5 s of period of oscillation). But second order transient scheme also tends to show a secondary frequency of 1.1s^{-1} (i.e. 0.98 s of period of oscillation). Hence it

can be said that, the prediction of the dynamics improves on using second order transient scheme. There is also a frequency of 0.62 s^{-1} which can be mainly seen in first order transient scheme with half geometry. The reasons behind the 0.62 s^{-1} frequency are not understood at this time.

With Wall Thermal Energy Storage Effects

The 1D linear code study showed that the wall thermal energy storage affects the prediction of the period of oscillation. It was observed that, the addition of wall thermal energy storage effects makes the prediction of period of oscillation more accurate and closer to the experiment. Figure 7.15 compares the FFT results of both the approaches for Xiong et al. Case 1 using first order transient scheme.

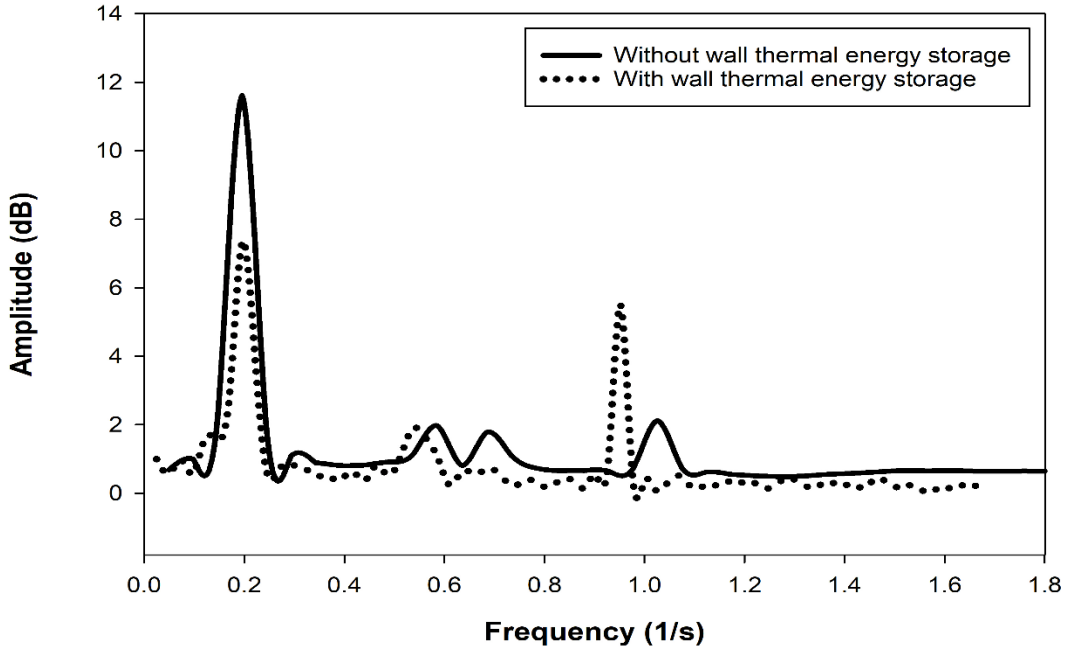

Figure 7.15 FFT analysis of CFX results of Xiong et al. Case 1, with and without wall thermal energy storage effects (First order transient scheme, Full geometry, 0.0334 kg/s)

It can be seen from the graph, that the frequency of 0.18 s^{-1}, which was dominant in FFT of without wall thermal energy storage effects, becomes less dominant in the results with wall thermal energy storage effects. It was also observed that the magnitude of the approximately 1s^{-1} frequency

increases in the results that include the wall thermal energy storage effects. These results indicate inclusion of wall energy storage effects improves the prediction of period of oscillation. It was also observed that the frequency response of the cases with wall thermal energy storage effects depends largely upon the temporal resolution (the order of the transient scheme and the timestep size).

(a)

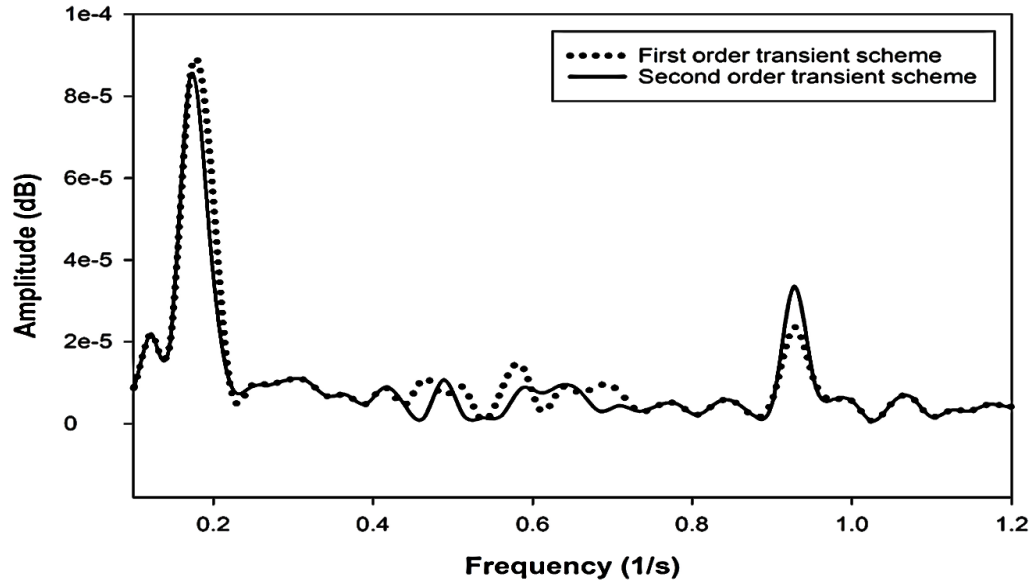

(b)

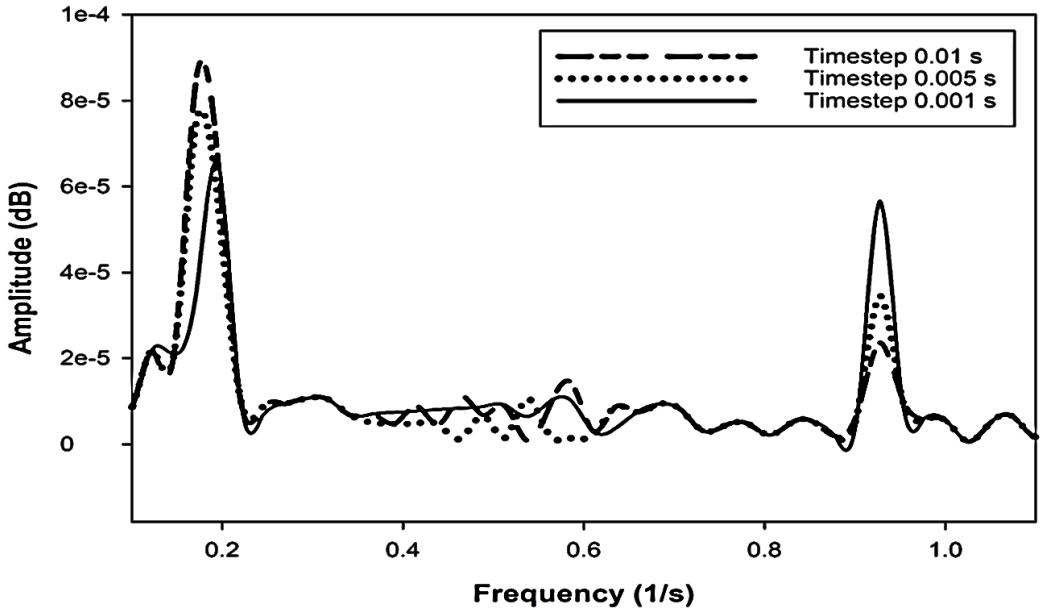

Figure 7.16 FFT results of CFX Case 1 with wall thermal storage effects
(a) First order transient scheme and second order transient scheme (timestep size 0.01 s)
(b) Three different timesteps (first order transient scheme)

Figure 7.16 (a) presents the frequency response of Case 1 with wall thermal energy storage effects using first and second order transient scheme (timestep of 0.01s). Figure 7.16 (b) shows the frequency response of Case 1 with wall thermal energy storage effects using three different timestep sizes (0.01s, 0.005s, 0.001s) using the first order transient scheme. The FFT results indicate that the second order transient scheme gives better predictions of period of oscillation than first order transient scheme. Also, the predictions of period of oscillation with timestep size 0.001 s are closest to the experiment.

7.3.8 Present CFX Predictions of Threshold Mass-flow Rates and Period of Oscillation with Wall Thermal Energy Storage Effects.

After determining the mesh and time step size, a total six experimental cases (Xiong et al. Cases 1,3 and 9 and Xi et al. Cases 1 ,2 and 3) were numerically investigated. All these cases have uniform power profiles. The full geometry, the second order transient scheme with timestep size of 0.01 s, and wall thermal energy storage effects were used in ANSYS CFX to obtain the instability boundaries. Figure 7.17 is a graph of two normalized mass flow rates for Case 9: one stable and one unstable; which have wall thermal energy storage effects. For a total mass flow rate of 0.0370 kg/s, the oscillation amplitudes grow slowly with time (unstable); on the other hand, the amplitude of the oscillations decreases with time for a total mass flow rate of 0.0365 kg/s (Stable). The average value, 0.0367 kg/s, is taken as the Case 9 stability boundary mass flow rate.

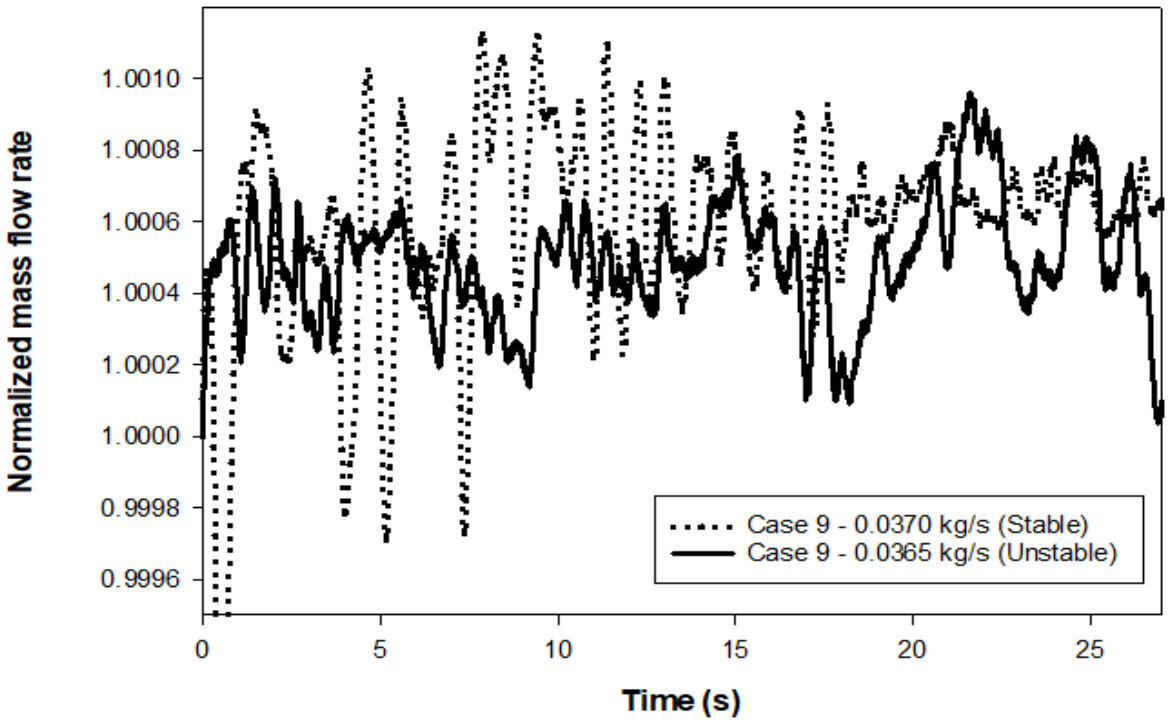

Figure 7.17 Normalized mass flow rate for Xiong et al. Case 9 - 0.0365 kg/s (unstable) versus 0.0370 kg/s (stable)

For a parallel channels system, if one channel oscillates first, it will initiate oscillations in the other channel to conserve the total mass flow rate. Thenceforth, both channels will oscillate. Because the inlet boundary condition for the parallel channels system of this study is constant total mass flow rate, channel 1 and channel 2 oscillate 180° out of phase to conserve the total mass flow rate, as demonstrated in Figure 7.18.

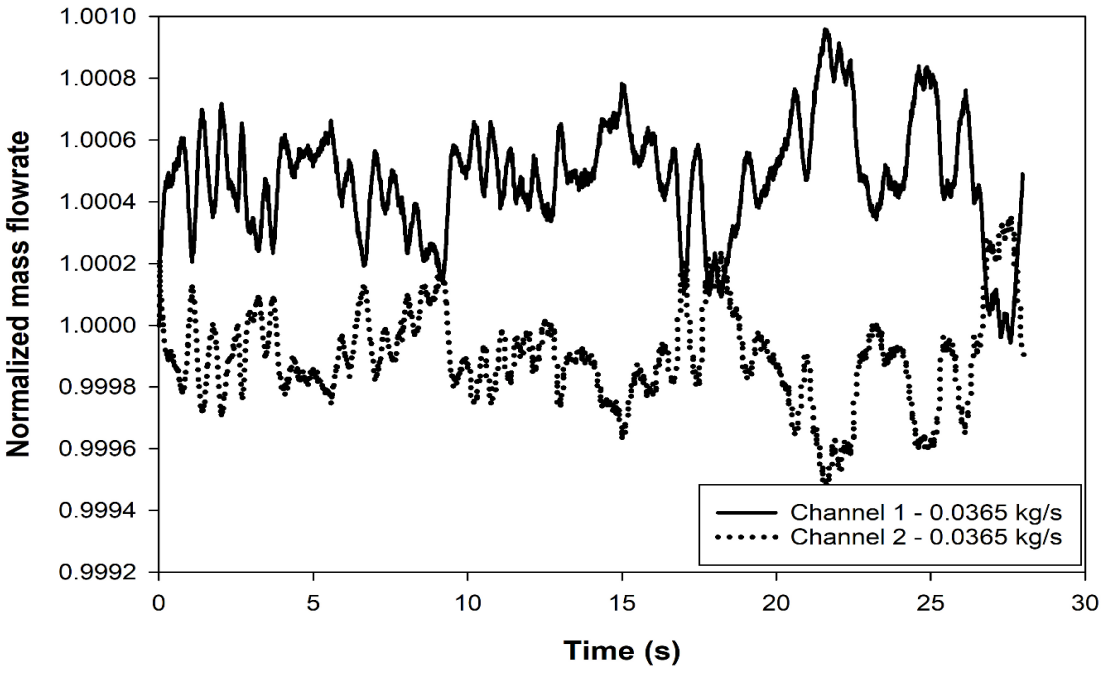

Figure 7.18 Normalized inlet and outlet mass flow rates for Xiong et al. Case 9

Table 7.13 summarizes the threshold mass flow rates of six experimental cases predicted by CFX.

Table 7.13 Threshold mass flow rate predictions with wall thermal energy storage

Case	**Threshold mass flow rate (kg/s)**		
	Experimental	**CFD predictions (No Wall)**	**CFD predictions (With Wall)**
Xiong et al. Case 1	0.0342	0.0336 (1.75%)	0.0336 (1.75%)
Xiong et al. Case 3	0.0333	0.0365 (-9.60%)	0.0348 (-4.50%)
Xiong et al. Case 9	0.0339	0.0356 (-5.01%)	0.0348 (-2.60%)
Xi et al. Uniform power Case 1	0.0347	0.0325 (-6.30%)	0.0315 (-9.20%)
Xi et al. Uniform power Case 2	0.0347	0.0390 (-12.39%)	0.0355 (-2.30%)
Xi et al. Uniform power Case 3	0.0347	0.0395 (-13.83%)	0.0365 (-5.10%)

7.3.9 Comparison of With and Without Wall Thermal Energy Storage Effects using Dimensionless Parameter N_{TPC}

The comparison of 1D linear code and CFX results can be made using the non-dimensional parameter N_{TPC} (Ambrosini and Sharabi 2008). Table 7.14 represents the comparisons of N_{TPC} values between the numerical analyses for the six experimental cases studied with CFX.

The RMS error of the CFX results without wall thermal energy storage effects is 9.17 %, this error is reduced to 4.96 % when wall thermal energy storage effects are included. The linear code 1D gives overall better predictions with an RMS error of 2.06% (With wall thermal energy storage effects) and 3.85% (Without wall thermal energy storage effects).

Table 7.14 N_{TPC} comparisons between numerical simulations and experimental results

Case number	**Exp.**	**CFD results (N_{TPC})**		**Linear code results (N_{TPC})**	
		With wall	**Without wall**	**With wall**	**Without wall**
Xiong et al. Case 1	3.54	3.41 (1.75%)	3.41(1.75%)	3.53 (0.25%)	3.31 (6.66%)
Xiong et al. Case 3	3.52	3.58 (-4.50%)	3.64(-9.60%)	3.42 (2.74%)	3.35 (4.72%)
Xiong et al. Case 9	3.35	3.41 (-2.60%)	3.51(-5.01%)	3.45 (-3.09%)	3.26 (2.79%)
Xi et al. Case 1	4.04	4.48 (-9.20%)	4.32 (-6.30%)	3.99 (1.12%)	3.96 (1.93%)
Xi et al. Case 2	3.95	4.10 (-2.30%)	4.48 (-12.39%)	3.88 (1.79%)	3.83 (2.34 %)
Xi et al. Case 3	3.90	4.17 (-5.10%)	4.61 (-13.83%)	3.81 (1.98%)	3.78 (2.24%)

Chapter 8

Conclusions and Recommendations

8.1 Conclusions

From the results of 1D -linear analyses with and without wall thermal energy storage effects and the examination of non-dimensional parameters, the following conclusions are drawn:

1. Excellent agreement between 1D- linear solution predictions and experimental data show that the 1D linear code can predict well the onset of supercritical flow instabilities including wall thermal energy storage effects, in two heated parallel channels with up-flow.
2. Including wall thermal energy storage effects improves the prediction of thermal hydraulic instability threshold.
3. The wall thermal energy storage effects has a small impact on the instability threshold of two similar (not identical) parallel channels with upward flow whereas they affect significantly a single channel. The wall had no effect on the instability boundary when the channels were identical. Thus, in the case of two identical parallel channels, there is a cancelling effect. It is unknown if this cancelling effect would exist with three parallel channels.
4. A linear, frequency-domain solution predicts accurately the period of oscillation.
5. The stability boundary predictions with wall thermal energy storage, for a parallel two channel system with the upward flow, are not significantly affected by the choice of correlation for the heat transfer coefficient between the wall and the fluid.
6. The non-dimensional parameter, N_{wall}, can convert the wall thickness of the heated section of a natural circulation experimental setup with one fluid (e.g. CO_2, R23, Ammonia) to

wall thickness with another fluid (water).

The Fast Fourier Transform (FFT) revealed the secondary, less dominant frequency of 5 seconds in the Xiong et al. experimental data, which explains predictions of 5s period of oscillation, in all previous 3D non-linear equation modelling. From the results of 3D CFD analyses using ANSYS CFX R18.2 with and without wall thermal energy storage effects, the following conclusions are drawn:

1. The agreement between the 3D CFD results and the experimental data shows that the 3D Navier-Stokes equation-based model can predict the onset of supercritical flow instabilities including wall thermal energy storage effects for up-flow in two heated parallel channels.
2. The 3D CFD code stability threshold predictions had greater RMS error compared to the experimental threshold than 1D linear code results.
3. The accuracy of the prediction of the period of oscillation depends on the transient scheme used in the CFD analysis. The second order transient scheme tends to produce more accurate results than the first order transient scheme (with and without wall thermal energy storage effects, at timestep size of 0.01 s).
4. Modelling wall thermal energy storage effects is important for the accurate prediction of the experiments, especially the period of oscillation.
5. Using the half geometry (assuming Symmetry), does not give good instability threshold predictions with wall thermal energy storage effects. The full geometry, on the other hand, gives reliable results with and without wall thermal energy storage effects, which agree well with the experiments.
6. The use of bigger plena helps to avoid solution convergence issues.

7. Small amplitude high frequency numerical oscillations are observed for a very small timestep such as 0.001s. These oscillations may be reduced by increasing the iterations per timestep to 120. For all the results presented here, 30 coefficient iterations per timestep were used. The numerical noise can also be reduced by increasing the number of radial nodes in the solid wall region.
8. Spatial grid size refinement across the radial direction in the wall does not have a significant influence on the predicted instability boundary predictions.
9. It is advisable to use as small timestep size as practically possible to improve the accuracy of the 3D CFD predictions. The accuracy of the predictions of period of oscillation improves with the reduction of timestep size and increment in order of transient scheme.

As noted earlier, none of the previous studies was able to obtain acceptable accuracy in numerical predictions with wall thermal energy storage effects. Previous researchers chose not to report modelling with the wall thermal energy storage effects (Sharma et al. 2015; Debrah et al. 2013b, 2013a) due to obtaining worse results with the wall modelled. This study is the first to report good results and good agreement with experiment using wall thermal energy storage effects. It shows that the wall thermal energy storage effects model in a 1D linear code and in ANSYS CFX R18.2 can give closer predictions to the experimental onset of two parallel channels with the upward flow.

8.2 Recommendations

The following recommendations are made for future studies:

1. The full geometry is suggested for all the future studies with wall thermal energy storage effects.
2. Analyse parallel channels downward flow, horizontal flow with linear solution and with CFD.
3. Analyse the parallel channels upward flow with wall thermal energy storage effects, using no axial conduction, in CFD.
4. Investigate the wall thermal energy storage effects in more than two parallel channels.
5. Model the Xi et al. non-uniform power cases using CFD (ANSYS CFX R18.2).
6. Analyse other fluids such as CO_2, Helium, and Methane using CFX to investigate their flow instability boundary in parallel channels.
7. Validate the non-dimensional parameter of wall, $N_{wall,}$ using experimental and numerical data for parallel channels.

References

Ambrosini, W. 2011. “Assessment of Flow Stability Boundaries in a Heated Channel with Different Fluids at Supercritical Pressure.” *Annals of Nuclear Energy* 38 (2): 615–27.

Ambrosini W., and Sharabi M. 2008. “Dimensionless Parameters in Stability Analysis of Heated Channels with Fluids at Supercritical Pressures.” *Nuclear Engineering and Design*, ICONE-14 - 14th International Conference on Nuclear Energy, 238 (8): 1917–29.

Ampomah-Amoako E. E., Akaho H. K., Benjamin J. B., Nyarko, and Ambrosini W. 2013. “Analysis of Flow Stability in Nuclear Reactor Subchannels with Water at Supercritical Pressures.” *Annals of Nuclear Energy* 60 (October): 396–405.

“ANSYS CFX Solver Theory Guide.” 2009. ANSYS.INC. https://www.sharcnet.ca/Software/Ansys/16.2.3/enus/help/cfx_thry/thry_rb_translationalEOM.html.

Bergmann C. 2015. “Comparison of Turbulence Model Predictions in Rod Bundles with Supercritical Up-Flow.” M.Sc. Thesis, Winnipeg: University of Manitoba. https://mspace.lib.umanitoba.ca/xmlui/handle/1993/31016.

Chatoorgoon V. 1986. “SPORTS - A Simple Non-Linear Thermalhydraulic Stability Code.” *Nuclear Engineering and Design* 93 (1): 51–67.

Chatoorgoon V. 2001. “Stability of Supercritical Fluid Flow in a Single-Channel Natural-Convection Loop.” *International Journal of Heat and Mass Transfer* 44 (10): 1963–72.

Chatoorgoon V. 2008. “Supercritical Flow Stability in Horizontal Channels.” *Nuclear Engineering and Design*, ICONE-14 - 14th International Conference on Nuclear Energy, 238 (8): 1940–46.

Chatoorgoon V., and Upadhye Preshit. 2005. “Analytical Studies of Supercritical Flow Instability in Natural Convection Loops.” In. Avignon, France.

D’Auria F., M. Modro, F. Oriolo, and K. Tasaka. 1993. “Relevant Thermalhydraulic Aspects of New Generation LWRs.” *Nuclear Engineering and Design* 145 (1): 241–59.

Debrah K. S., Ambrosini W., and Chen Y. 2013a. “Discussion on the Stability of Natural Circulation Loops with Supercritical Pressure Fluids.” *Annals of Nuclear Energy* 54 (April): 47–57.

Debrah K. S., Ambrosini W., and Chen Y. 2013b. “Assessment of a New Model for the Linear and Nonlinear Stability Analysis of Natural Circulation Loops with Supercritical Fluids.” *Annals of Nuclear Energy* 58 (August): 272–85.

Dutta G., Chao Z., and Jiang J. 2015. “Analysis of Parallel Channel Instabilities in the CANDU Supercritical Water Reactor.” *Annals of Nuclear Energy* 83 (September): 264–73.

Ebrahimnia E., Chatoorgoon V., and Ormiston S. J. 2016. “Numerical Stability Analyses of Upward Flow of Supercritical Water in a Vertical Pipe.” *International Journal of Heat and Mass Transfer* 97 (June): 828–41.

Ebrahimnia E. 2014. “Numerical Stability and Heat Transfer Analyses of Supercritical Water Flowing Upward In Vertical Heated Pipes.” M.Sc. Thesis, Winnipeg: University of Manitoba.

Gabaraev B. A., I. K. Ganev, V. K. Davydov, Y. N. Kuznetsov, V. A. Reshetov, and A. V. Smirnov 2003. “Vessel and Channel Fast Reactors Cooled by Boiling Water or Water with Supercritical Parameters.” *Atomic Energy* 95 (4): 655–62.

Ghadge D., and Chatoorgoon V.. 2018. “Analytical Study of Supercritical Water Flow in Two Heated Parallel Channels with Wall Heat Effect.” In London, UK.

Gómez T. O, Class R., Lahey T., and Schulenberg T. 2008. “Stability Analysis of a Uniformly Heated Channel with Supercritical Water.” *Nuclear Engineering and Design,* ICONE-14 - 14th International Conference on Nuclear Energy, 238 (8): 1930–39.

Hou D., Meng L., Pengfei L., and Yanhua Y. 2011. “Stability Analysis of Parallel-Channel Systems with Forced Flows under Supercritical Pressure.” *Annals of Nuclear Energy* 38 (11): 2386–96.

Li S., V. Chatoorgoon, and S. J. Ormiston. 2018. “Numerical Study of Oscillatory Flow Instability in Upward Flow of Supercritical Water in Two Heated Parallel Channels.” *International Journal of Heat and Mass Transfer* 116 (January): 16–29.

Li S. 2016. “Numerical Instability Study Of Supercritical Water Flowing Upward In Two Heated Parallel Channels.” M.Sc. Thesis, Winnipeg: University of Manitoba.

Liu J., Li H., Lei X., Kaikai G., and Liangxing Li. 2018. “Numerical Study on the Effect of Pipe Wall Heat Storage on Density Wave Instability of Supercritical Water.” *Nuclear Engineering and Design* 335 (August): 106–15.

March-Leuba J., and Rey J.M. 1993. “Coupled Thermohydraulic-Neutronic Instabilities in Boiling Water Nuclear Reactors: A Review of the State of the Art.” *Nuclear Engineering and Design 145*, 97–111.

Nuclear Energy Institute. 2017. “Nuclear Energy Institute.” Nuclear Energy Institute. 2017. https://www.nei.org/resources/statistics.

OECD. 2000. “Technology Roadmap Update for Generation IV Nuclear Energy Systems,” 66.

Oka Y., and Seiichi K. 2001. “Supercritical-Pressure, Once-through Cycle Light Water Cooled Reactor Concept.” *Journal of Nuclear Science and Technology* 38 (12): 1081–89.

Pioro I. L., and Duffey R. B. 2005. “Experimental Heat Transfer in Supercritical Water Flowing inside Channels (Survey).” *Nuclear Engineering and Design* 235 (22): 2407–30.

Pioro I. L., and Mokry S. 2011. “Thermophysical Properties at Critical and Supercritical Conditions.” *Heat Transfer*, 22.

Sharabi M. B., Ambrosini W., and He S. 2008. “Prediction of Unstable Behaviour in a Heated Channel with Water at Supercritical Pressure by CFD Models.” *Annals of Nuclear Energy* 35 (5): 767–82.

Sharma M., Bodkha K., Pilkhwal D. S., and Vijayan P. K. 2015. “A Supercritical Pressure Parallel Channel Natural Circulation Loop,” NURETH 17.

Sharma M., Vijayan P. K., Pilkhwal D. S., and Yutaka A. 2014. “Natural Convective Flow and Heat Transfer Studies for Supercritical Water in a Rectangular Circulation Loop.” *Nuclear Engineering and Design* 273 (July): 304–20.

Shitsi E., Debrah S. K., Agbodemegbe V. Y., Ampomah-Amoako. 2017. “Numerical Investigation of Flow Instability in Parallel Channels with Supercritical Water - ScienceDirect.” *Annals of Nuclear Energy* 110: 196–207.

United Nations. 2017. “World Population Projected to Reach 9.8 Billion in 2050, and 11.2 Billion in 2100 | UN DESA | United Nations Department of Economic and Social Affairs.” 2017.

https://www.un.org/development/desa/en/news/population/world-population-prospects-2017.html.

Wagner W., Cooper J. R., Dittmann A., Kijima J., Kretzschmar H.-J., Kruse A., Mareš R., 2000. "The IAPWS Industrial Formulation 1997 for the Thermodynamic Properties of Water and Steam." *Journal of Engineering for Gas Turbines and Power* 122 (1): 150–84.

Xi X., Zejun X., Xiao Y., Yongliang L., and Yanping H. 2014. "An Experimental Investigation of Flow Instability between Two Heated Parallel Channels with Supercritical Water." *Nuclear Engineering and Design* 278 (October): 171–81.

Xi X., Zejun X., Xiao Y., Xiong, and Yanping H. 2014. "Numerical Simulation of the Flow Instability between Two Heated Parallel Channels with Supercritical Water." *Annals of Nuclear Energy* 64 (February): 57–66.

Xiong T., Xiao Y., Shanfang H., Junchong Y., and Yanping H. 2013. "Modeling and Analysis of Supercritical Flow Instability in Parallel Channels." *International Journal of Heat and Mass Transfer* 57 (2): 549–57.

Xiong T., Xiao Y., Zejun X., Yongliang L., Yanping H., and Junchong Y. 2012. "Experimental Study on Flow Instability in Parallel Channels with Supercritical Water." *Annals of Nuclear Energy* 48 (October): 60–67.

Feng Y. L., Hao Z., Wenxi T., Guanghui S., Suizheng Q. 2013. "Theoretical Study on the Flow Instability of Supercritical Water in the Parallel Channels - ScienceDirect." *Progress in Nuclear Energy* 68: 169–76.

Zhang L. 2018. "Flow Instability Study of a Natural Circulation Loop with Supercritical Fluids - UMB - University of Manitoba.",M.Sc.Thesis

Zhao J. 2005. “Stability Analysis of Supercritical Water Cooled Reactors.” Thesis, Massachusetts Institute of Technology.

Zuber N. 1966. “An Analysis of Thermally Induced Flow Oscillations near Critical and Super-Critical Region.” Report by *Marshall Space Flight Center NASA Huntsville*